Modelling of flow through porous packing elements of a CO_2 absorption tower

by

Christo Rautenbach

Thesis presented at the University of Stellenbosch in partial fulfilment of the requirements for the degree of
Master of Natural Sciences

Department of Mathematical Sciences
Supervisor:
Desember 2009

DECLARATION

By submitting this dissertation electronically, I declare that the entirety of the work contained therein is my own, original work, that I am the owner of the copyright thereof (unless to the extent explicitly otherwise stated) and that I have not previously in its entirety or in part submitted it for obtaining any qualification.

December 2009

Abstract

Modelling of flow through porous packing elements of a CO_2 absorption tower

C. Rautenbach

Department of Mathematical Sciences
University of Stellenbosch
Private Bag X1, 7602 Matieland, South Africa

Thesis: MSc (Applied Mathematics)

February 2009

Packed beds are widely used in industry to improve the total contact area between two substances in a multiphase process. The process typically involves forced convection of liquid or gas through either structured or dumped solid packings. Applications of such multiphase processes include mass transfer to catalyst particles forming the packed bed and the adsorption of gases or liquids on the solid packing.

An experimental study on the determination of air flow pressure drops over different packing materials was carried out at the Telemark University College in Porsgrunn, Norway. The packed bed consisted of a cylindrical column of diameter $0.072m$ and height $1.5m$, filled with different packing materials. Air was pumped vertically upwards through a porous distributor to allow for a uniform inlet pressure. Resulting pressure values were measured at regular height intervals within the bed. Due to the geometric nature of a Raschig ring packing wall effects, namely the combined effects of extra wall shear stress due to the column surface and channelling due to packing adjacent to a solid column surface, were assumed to be negligible.

Several mathematical drag models exist for packed beds of granular particles and an important question arises as to whether they can be generalized in a scientific manner to enhance the accuracy of predicting the drag for different kinds of packing materials. Problems with the frequently used Ergun equation, which is based on a tubular model for flow between granules and then being empirically adjusted, will be discussed. Some theoretical models that improve on the Ergun equation and their correlation with experimental work will be discussed. It is shown that a particular pore-scale model, that allows for different geometries and porosities, is superior to the Ergun equation in its predictions. Also important in the advanced models is the fact that it could take into account anomalies such as dead zones where no fluid transport is present and surfaces that do neither contribute to shear stress nor to interstitial form drag. The overall conclusion is that proper modelling of the dynamical situation present in the packing can provide drag models that can be used with confidence in a variety of packed bed applications.

Uittreksel

Modellering van vloei deur die pakkings-elemente van 'n CO_2 absorpsie toring

("Modelling of flow through porous packing elements of a CO_2 absorption tower")

C. Rautenbach

Departement van Wiskundige Wetenskappe
Universiteit van Stellenbosch
Privaatsak X1, 7602 Matieland, Suid Afrika

Tesis: MSc (Toegepaste Wiskunde)

Februarie 2009

Gepakte materiaal strukture word in die industrie gebruik om die kontak area tussen twee stowwe in meervoudige faseprosesse te vergroot. Die proses gaan gewoonlik gepaard met geforseerde konveksie van 'n vloeistof of 'n gas deur gestruktureerde of lukrake soliede gepakte strukture. Toepassings van sulke meervoudige faseprossese sluit onder andere in die massa-oordrag na katalisator partikels wat die gepakte struktuur vorm of die absorpsie van gasse of vloeistowwe op die soliede gepakte elemente.

'n Eksperimentele ondersoek oor die drukval van veskillende gepakte elemente in 'n kolom is gedoen by die Telemark University College in Porsgrunn, Noorweë. Die gepakte struktuur het bestaan uit 'n kolom met 'n diameter van $0.072m$ en 'n hoogte van $1.5m$. Lug is vertikaal opwaarts gepomp deur 'n poreuse plaat wat gesorg het vir 'n benaderde uniforme snelheidsprofiel. Die druk is toe op intervalle deur die poreuse struktuur gemeet. In die studie is die effekte van die eksterne wande, nl. die bydrae van die wand se wrywing en die vorming van kanale langs die kolom wand, as weglaatbaar aanvaar.

Daar bestaan baie wiskundige dempingsmodelle vir gepakte strukture wat uit korrels saamgestel is. 'n Belangrike vraag kan dus gevra word, of laasgenoemde modelle veralgemeen kan word op 'n wetenskaplike manier om die demping deur verskillende gepakte strukture akkuraat te kan voorspel. Probleme wat ontstaan het met die wel bekende Ergun vergelyking, wat gebaseer is op 'n kapillêre model en wat toe verder aangepas is deur empiriese resultate van uniforme sfere, sal bespreek word. Teoretiese modelle wat verbeteringe op die Ergun vergelyking voorstel sal bespreek word en vergelyk word met eksperimentele data. Daar word ook gewys dat 'n spesifieke porie-skaal model, wat aanpasbaar is vir verskillende geometrieë en porositeite, in baie gevalle beter is as die Ergun vergelyking. 'n Ander baie belangrike aspek van gevorderde modelle is die moontlikheid om stagnante gebiede in die gepakte strukture in ag te neem. Laasgenoemde gebiede sal die totale kontak area sowel as die intermediêre vorm demping verlaag. Die gevolgtrekking is dat wanneer deeglike modulering van dinamiese situasies in die industrie gedoen word kan dempings modelle met vertroue op 'n verskeidenheid gepakte strukture toegepas word.

Acknowledgements

I would like to express my sincere gratitude to the following people and organisations who have contributed to making this work possible:

- Jesus for making so many dreams come true and for always being there for me. I trust you completely my Lord,
- My family, for there constant support and love that carried me through the good and the not so good. *Baie dankie Pa, Ma, Ess-Jee en Ouma*,
- My friends, especially my colleague at the Physics Department, Francesca Helen Mountfort for proof reading this work as well as being the most loyal friend I have ever had,
- Prof J. P. du Plessis of the University of Stellenbosch as my study leader. Thank you for all of the opportunities you gave me and the wisdom and guidance you imparted to me through the course of this degree,
- Prof B. M. Halvorsen for facilitating me and my colleagues in Norway and taking care of us while we were there. Thank your for you guidance in the experimental work and also for funding our visit to your beautiful country. *Tusen takk Britt*,
- Last but most certainly not least, all of my friends in Paarl and Stellenbosch. You guys who listened to me even though you had no idea what I was talking about. Thank you for standing with me through the course of my studies.

Dedications

Hierdie tesis word opgedra aan my God en Here ,
Jesus die Christus,
vir Sy bonatuurlike ondersteuning, liefde en leiding.

Contents

Nomenclature

Latin symbols:

a	$[m^2/m^3]$ specific surface
a_v	$[m^2/m^3]$ specific surface of a particle
A	$[m^2]$ cross sectional area of packing
c_d	[-] form drag coefficient
d	$[m]$ dimension of an RUC
d_c	$[m]$ column diameter
d_e	$[m]$ equivalent particle diameter, $6V_p/S_p$
d_{gV}	$[m]$ equivalent cubic diameter
d_h	$[m]$ hydraulic diameter of the packing, $\frac{4\epsilon}{a}$
d_{pp}	$[m]$ distance between parallel surfaces in a RUC
d_p	$[m]$ particle diameter
d_s	$[m]$ linear dimension of solid cube in a granular RUC
$\overline{d}_{sv}$	$[m]$ surface-volume mean diameter
D_a	$[m]$ arithmetic diameter
D_{avg}	$[m]$ nominal size of particle according to sieve analysis
D_p	$[m]$ nominal diameter or equivalent diameter
F	$[kg\ m\ s^{-2}]$ force
F	[-] dimensionless shear factor
F_v	$[\ s^{-1}\ (kg/m)^{1/2}\ ]$ gas flow factor, $q\sqrt{\rho}$
k	$[m^2]$ hydrodynamic permeability
K	[-] wall factor, eqn. (5.1.10)
L	$[m]$ packed bed depth
l	$[m]$ length of pore scale
m	[-] Sonntag's correction
n	[-] ratio of specific surface of particle to the specific surface of a sphere of the same diameter (nominal size)
$\underline{n}$	[-] normal vector on $\partial\mathcal{U}$ pointing out of $\mathcal{U}$
$\underline{\hat{n}}$	[-] streamwise direction
$\underline{\tilde{n}}$	[-] interstitial velocity direction
N	$[m^{-1}]$ number of particles per unite volume

p [Pa] measured pressure in the case of experiments and numerical simulation
p [Pa] interstitial pressure
p_f [Pa] intrinsic phase average pressure
P [Pa] pressure in open section of column
$\tilde{p}$ [Pa] pressure deviation, p-p_f
$\underline{q}$ [$m\ s^{-1}$] superficial velocity
$\underline{q}_{mf}$ [$m\ s^{-1}$] minimum fluidization velocity
r_h [m] hydraulic radius
$\underline{r}$ [m] arbitrary position vector
$\underline{r}_o$ [m] position vector of REV centroid
Re [-] Reynolds number
Re_G [-] gas phase Reynolds number, $\frac{qd_h\rho}{\mu\epsilon}$
Re_m [-] Reynolds number for porous media, $\frac{\rho q\sqrt{k}}{\mu}$
Re_p [-] effective interstitial Reynolds number, $\frac{\rho q d_p}{\mu}$
Re_{qd_s} [-] particle Reynolds number, $\frac{\rho q d_s}{\mu}$
s_{fs} [m^2] surface of a single particle
$S_{\parallel}$ [m^2] surface area in RUC adjacent to streamwise fluid volume
$S_{\perp}$ [m^2] surface area in RUC adjacent to transverse fluid volume
S_{ff} [m^2] fluid-fluid interface
S_{fs} [m^2] fluid-surface interface (particle surface area)
S_p [m^2] surface area of a single particle
S_{ss} [m^2] solid-solid interface
$\mathcal{U}_f$ [m^3] fluid phase constituent of an elementary volume
$\mathcal{U}_o$ [m^3] total volume of an elementary volume
$\mathcal{U}_s$ [m^3] total solid volume of an elementary volume
U_f [m^3] total fluid volume
U_{fs} [ms^{-1}] fully supported velocity
U_{mf} [ms^{-1}] minimum fluidization velocity
U_o [m^3] total volume
U_s [m^3] total solid volume
$\underline{v}$ [$m\ s^{-1}$] particle velocity
$\underline{v}_p$ [$m\ s^{-1}$] cross-sectional mean velocity in streamwise duct section
V_p [m^3] volume of particular particle
W [kg] weight of packed bed
x [-] mass fraction

Greek symbols:

β	[-] average pore velocity ratio, $\frac{v_{\perp}}{v_{\|\|}}$
ϵ	[-] porosity or void fraction
μ	[$N\ s\ m^{-2}$] fluid dynamic viscosity
ρ	[$kg\ m^3$] density
ρ_f	[$kg\ m^3$] fluid mass density
ρ_p	[$kg\ m^3$] particle- or solid mass density
τ	[$N\ m^{-2}$] local shear stress
ϕ_s	[-] shape factor (sphericity)
ϕ_{gran}	[-] shape factor (sphericity) of the RUC granular model
φ	[-] form factor
χ	[-] tortuosity factor
ψ	[-] geometric factor

Chapter 1

Introduction to absorption towers

In engineering practice packed beds are used to create a large contact area between a liquid and a gas or a liquid/gas and a solid. This is achieved by creating a large surface to volume ratio. Figure 1.1 shows a schematic example of a typical atmospheric CO_2 absorption tower. The absorber is typically sodium hydroxide (NaOH) but a variety of different absorbers are used in the industry. The absorber is uniformly sprayed from the top of the tower, wetting the solid parts of the porous packed beds, whilst the CO_2 gas is pumped in from the bottom of the tower. Thus the CO_2 comes into contact with the absorber on the wet solid surface of the porous packed bed. The lean gas, containing a low percentage of CO_2, leaves the tower at the top and the liquid containing the soluble CO_2 is drained from the tower at the bottom. The larger the wet fluid-solid-interface the better the absorption.

There is a wide range of different packing materials available. The packing material used varies from application to application. Factors that need to be considered include the pressure drop produced by the packed bed, chemical stability of the packing and size of the packing, to name but a few. Porous media created by using the packing materials illustrated in Figure 1.2 are called random dumped packings, as they are randomly placed into the container. From the wide variety of random dumped packing elements used in the industry, only a few will be investigated in this work, due to the availability of the elements. Raschig rings and small glass spheres were provided by the TUC in Porsgrunn Norway and are used to verify results produced in the present study. At present structured packing is mainly used in the CO_2 absorption process but in this work the efficiency of structured packings are compared to that of random dumped packings. The possibility that random dumped packings may be more effective than structured packings is of particular interest as it is easier and more cost effective to construct. An example of structured packing material is given in Figure 1.3. This packing is not random but designed specifically according to the demand of the application in which it will be used. Structured packing is made of corrugated sheets arranged in a crisscrossing fashion. The rotation of each layer of the structured packing about the column axis facilitates cross mixing of the vapor and the liquid in all directions [13]. Wall wipers are also present in a column fitted with structured packing to prevent vapour and/or liquid bypassing along the column wall. Successful optimization of costly processes regarding the absorption of CO_2 depends to a large extent on the accuracy to which flow characteristics in the various components of the absorption tower can be predicted. The variety of packing materials used as modules in the tower can be considered as porous media, allowing a theoretical analysis and subsequent predictive expressions linking velocity to pressure gradients. A prime goal of the current study is to substantiate such mathematical analysis by numerical computation and experimental data.

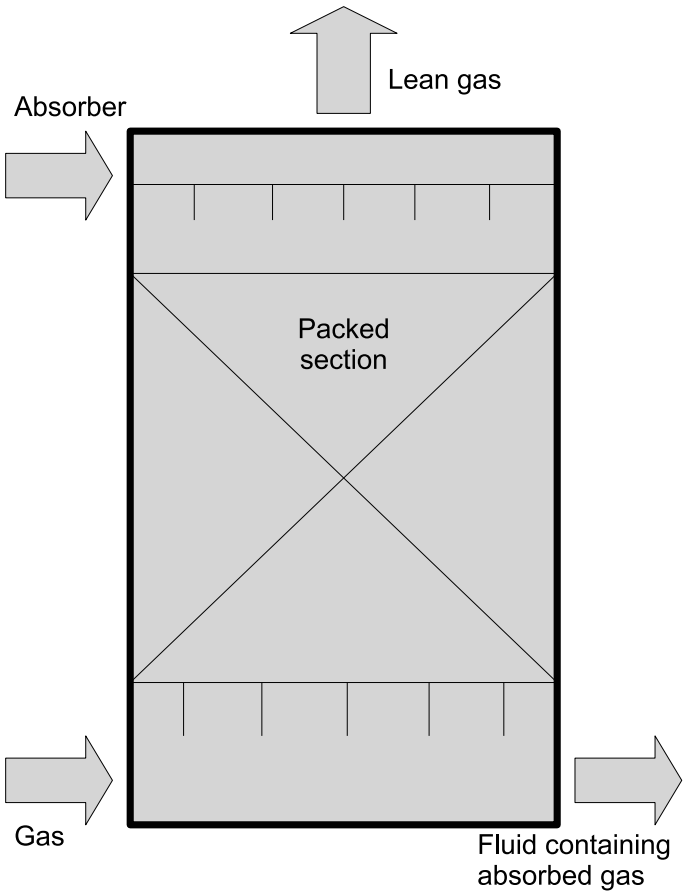

Figure 1.1: Schematic illustration of a CO_2 absorption tower .

(a) Pall ring. (b) Intalox metal tower packing (IMTP). (c) Raschig ring.

Figure 1.2: Typical examples of random packings.

The research project entails a literature study on the problem addressed, followed by analytical and computational studies on single phase Newtonian flow of gas through the packing. The research involves analytical and computational work to predict the flow characteristics, such as velocity distributions and pressure gradients in the packing elements of a typical CO_2 absorption tower. The research was conducted in collaboration with the Telemark University College in Porsgrunn, Norway, and included a two months visit to the TUC, mainly for the experimental aspects of the research.

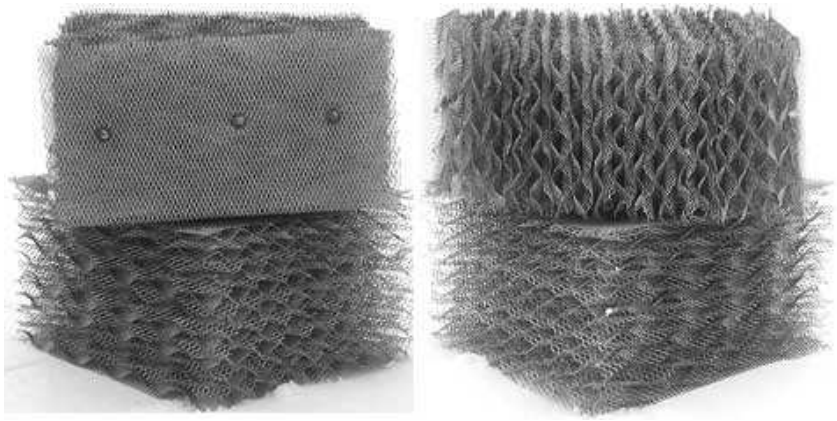

Figure 1.3: Typical example of a structured packing element.

This project ties in with the research done on porous media at the University of Stellenbosch and this creates an ideal opportunity to apply the research results in high technology practice. It also provides insight into the flow processes within the packing elements of an absorption tower. This can be of considerable aid to large scale computations on the overall functioning of the tower and enhance optimization of the absorption process. A good understanding of single phase flow through porous media is crucial to the understanding and modelling of two phase flow through porous media.

Chapter 2

Drag models

A RUC drag model was developed at the University of Stellenbosch since 1990 and is used in this work to give a possible prediction of single phase flow through the packing elements of a CO_2 absorption tower. This chapter will be devoted to an outline of principal features of this model [6].

2.1 Volume averaging theory

Volume averaging is performed to obtain volume averaged quantities of the interstitial variables that can then be compared to measured quantities.

2.1.1 Representative elementary volume (REV)

A representative elementary volume is defined as a volume $\mathcal{U}_o$ consisting of both fluid and solid parts which is a statistical representation of the local average properties of the porous medium. The volume of the solid constituent of the elementary volume $\mathcal{U}_o$ is denoted by $\mathcal{U}_s$. The fluid constituent within $\mathcal{U}_o$ is denoted by $\mathcal{U}_f$. A schematic example of a porous medium is given in Figure 2.1. The magnitude of a REV must be in the bound of:

$$l^3 << \mathcal{U}_o << L^3, \tag{2.1.1}$$

where l is the width of the pore scale and L is the macroscopic dimensions of the porous structure. Within the REV interfaces exist between solid-solid, fluid-fluid and fluid-solid. The solid-solid interface is denoted by S_{ss}, the fluid-fluid by S_{ff} and finally the fluid-solid interface is denoted by S_{fs} (see Figure 2.1). An arbitrary position in the porous structure is denoted by the position vector $\underline{r}$ while the centroid of the REV is denoted by the position vector $\underline{r}_o$. It is of importance to note that the arbitrary vector, $\underline{r}$, may be the position vector of a point anywhere in the porous structure including the interfaces. In the notation used the porosity (or void fraction) is denoted by:

$$\epsilon \equiv \frac{\mathcal{U}_f}{\mathcal{U}_o}. \tag{2.1.2}$$

In an attempt to understand and quantify the interstitial parameters of a porous structure, mathematical and numerical models are being developed to approximate the flow conditions in the pore-space. The RUC drag model is one such model. The RUC approximates the porous structure by imbedding the average geometric characteristics of the material (as

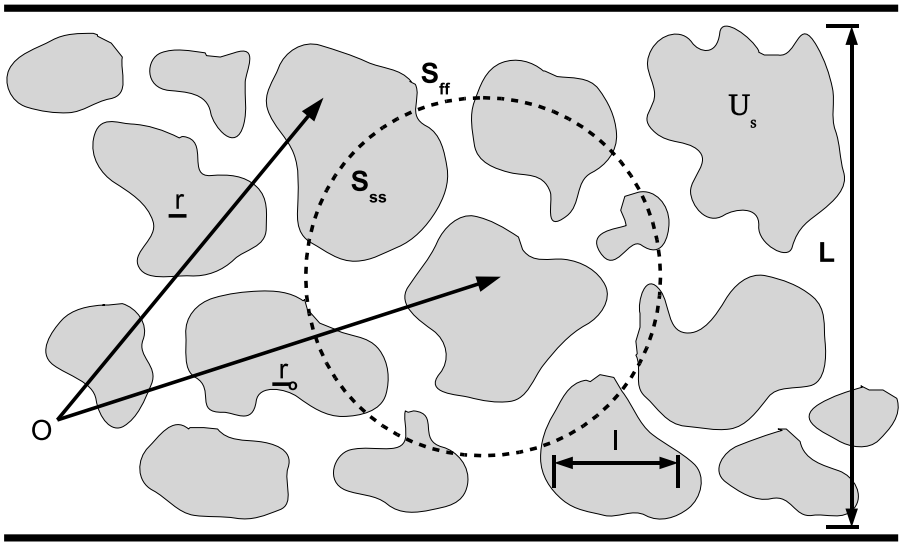

Figure 2.1: Spherical representative elementary volume.

found in an REV) within the smallest possible hypothetical representative unit cell (RUC). A brief summary of the derivation and results of closure of the RUC model is given in the next section.

2.1.2 Volume averaging of transport equations

The two equations governing the momentum transfer of fluid within the void sections of the porous medium are the continuity equation and the Navier-Stokes equation [6]. The interstitial conservation of mass is governed by the continuity equation as follows:

$$\frac{\partial \rho}{\partial t} + \nabla \cdot (\rho \underline{v}) = 0. \tag{2.1.3}$$

The momentum transport equation describes the momentum transport of an incompressible Stokes fluid and is given by the following equation:

$$\rho \frac{\partial \underline{v}}{\partial t} + \nabla \cdot (\rho \underline{v}\ \underline{v}) - \rho \underline{g} + \nabla p - \nabla \cdot \underline{\underline{\tau}} = \underline{0}. \tag{2.1.4}$$

If time independence is assumed in equation (2.1.3) and (2.1.4), all of the partial derivatives with respect to time will be zero. The phase average of equation (2.1.3) is given by equation (2.1.5) with the assumption that there is a no-slip condition on the boundary and that the flow is incompressible.

$$\nabla \cdot \underline{q} = 0. \tag{2.1.5}$$

The volume averaging of the momentum transport equation (2.1.4) leads to equation (2.1.6) if the average field $\underline{q}$ is assumed uniform and given a Newtonian fluid with a constant vis-

cosity, μ, no-slip boundary conditions and constant uniform porosity.

$$-\epsilon\nabla p_f = \frac{1}{\mathcal{U}_o}\iint\limits_{S_{fs}} (\underline{n}\widetilde{p} - \underline{n}\cdot\underline{\underline{\tau}})\,\mathrm{d}S. \tag{2.1.6}$$

2.1.2.1 Creep flow at low Reynold numbers ($Re \to 0$)

Let the integral in equation (2.1.6) be denoted by $\underline{I}$. In the lower Reynolds number limit ($Re \to 0$) where only viscous drag is present, it follows that:

$$\underline{I}_o = \frac{1}{\mathcal{U}_o}\iint\limits_{S_{fs}} (\underline{n}\widetilde{p} - \underline{n}\cdot\underline{\underline{\tau}})\,\mathrm{d}S, \tag{2.1.7}$$

given a situation of Stokes flow.

2.1.2.2 Inertial flow ($Re \to 2000$)

A dimensionless shear factor is needed in the Forchheimer regime at high Reynolds number flow ($Re \to 2000$). In this regime recirculation develops but turbulence is still absent. Inertial effects due to interstitial recirculation dominate. Equation (2.1.6) can be expressed as follows:

$$\underline{I}_\infty = \frac{1}{\mathcal{U}_o}\iint\limits_{S_{fs}} \underline{n}\widetilde{p}\,\mathrm{d}S. \tag{2.1.8}$$

In the previous definition the high Reynolds number limit implies the laminar limit where turbulence is not yet present.

2.2 General closure with a Representative Unit Cell (RUC)

In the context of this work, closure implies a process of applying a model to write the surface integral in terms of known macroscopic parameters.

2.2.0.3 Creep flow

If the wall shear stress τ_w is assumed uniform and constant over S_{fs} in all channel sections in a RUC (Representative Unit Cell) and the flow is assumed to be a fully developed Newtonian flow between all parallel plate sections a distance $d_p p$ apart, it follows that [7]:

$$\underline{I}_o = \left(\frac{S_{||} + \beta S_\perp}{\mathcal{U}_o}\right)\cdot\left(\frac{6\mu v_p}{d_p p}\right)\hat{\underline{n}} = \frac{S_{||} + \beta\xi S_\perp}{\mathcal{U}_o}\cdot\frac{6}{d_p}\left(\frac{\psi^2}{\epsilon}\right)\mu\underline{q}, \tag{2.2.1}$$

given the average transverse interstitial velocity βv_p. A new constant is defined as:

$$G_o \equiv \frac{6\psi^2}{\epsilon d_p}\cdot\frac{S_{||} + \beta S_\perp}{\mathcal{U}_o}, \tag{2.2.2}$$

and thus it follows from equation (2.2.2) that:

$$\underline{I}_o = -\epsilon\nabla p_f = G_o\mu\underline{q}. \tag{2.2.3}$$

An expression for the dimensionless overall shear factor, G_o, has thus been determined in the Darcy regime at low Reynolds number flow.

2.2.0.4 Inertial flow

If the contribution of shear stresses is discarded because of the predominance of the pressure gradient, it follows that equation (2.1.8) can be expressed as:

$$\underline{I}_\infty = \frac{S_\perp}{\mathcal{U}_o} \cdot \frac{c_d \rho q}{4} \left(\frac{\psi^2}{\epsilon} \right)^2 \underline{q}. \tag{2.2.4}$$

If G_∞ is geometrically determined as:

$$G_\infty \equiv c_d \frac{S_\perp}{\mathcal{U}_o d_p} \left(\frac{\psi^2}{2\epsilon} \right)^2 Re_{qd_s}, \tag{2.2.5}$$

it follows that:

$$\underline{I}_\infty = G_\infty \mu \underline{q}. \tag{2.2.6}$$

An expression for the overall shear factor, G_∞, has thus been determined in the Forcheimer regime at high Reynolds number flow.

2.2.0.5 Unifying overall shear factor

Making use of the power addition technique described by Churchill and Usagi [3], a unifying factor G can be defined as:

$$G = [G_o^s + G_\infty^s]^{1/s}. \tag{2.2.7}$$

Here s is the shifting parameter and is used to shift the functional value G closer or further away from the asymptotes at the critical point. Finally equation (2.1.6) can be written as:

$$-\epsilon \nabla p_f = G \mu \underline{q}. \tag{2.2.8}$$

In the following subsection the F-values (shear factor) for different porous structure families are presented as obtained by Du Plessis [7, 4] with closure of the RUC drag model. The relationship between the shear factor G and F is described by:

$$F = \frac{G}{\epsilon}. \tag{2.2.9}$$

2.2.0.6 Granular porous media

This model aims to approximate porous media such as sand, consisting of small granular parts. The RUC for a granular porous medium is given in Figure 2.2. The darker area at the center of the RUC corresponds to the solid phase and is surrounded by the fluid phase.

The expression for the overall shear factor for granular porous media is thus expressed as:

$$F d_s^2 = \frac{25.4(1-\epsilon)^{4/3}}{\left(1-(1-\epsilon)^{1/3}\right)\left(1-(1-\epsilon)^{2/3}\right)^2} + \frac{c_d(1-\epsilon)}{2\epsilon\left(1-(1-\epsilon)^{2/3}\right)^2} Re_{qd_s}, \tag{2.2.10}$$

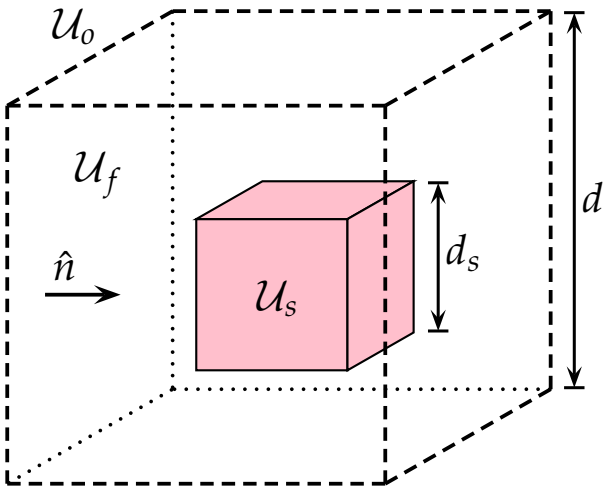

Figure 2.2: RUC for a granular porous medium.

according to Du Plessis [7]. In equation (2.2.10) Re_{qd_s} is defined as:

$$Re_{qd_s} \equiv \frac{\rho q d_s}{\mu}. \tag{2.2.11}$$

The form drag coefficient is represented by c_d and should typically be determined either numerically or empirically. The streamwise pressure drop can be determined via the drag factor, F, as follows:

$$-\frac{dp}{dx} = \mu q F. \tag{2.2.12}$$

2.2.0.7 Foamlike porous media

The RUC foam model was developed to accurately predict flow behavior through foamlike porous media. One possible representation of a foam is given in Figure 2.3. It should be noted that Figure 2.3 is only one representation of a possible foam. Other variations of the foam model do exist depending on the medium being modelled [4]. The shaded part in Figure 2.3 represents the fluid constituent while the rest is the solid part of the foam medium.

A typical example is a spongelike substance. The two variations that exist in the foam model are the doubly staggered model and the singly staggered model (for more detail refer to Du Plessis *et al.* [4]). The friction factor is given as:

$$F = \frac{24\psi^2\,(\psi-1)}{d^2\epsilon^2} + \frac{c_d\rho q\,\psi^2(\psi-1)}{2d\mu\,\epsilon^2(3-\psi)}, \tag{2.2.13}$$

in the case of the doubly staggered model and as:

$$F = \frac{36\psi^2\,(\psi-1)}{d^2\epsilon^2} + \frac{c_d\rho q\,\psi^2(\psi-1)}{d\mu\,\epsilon^3(3-\psi)}, \tag{2.2.14}$$

for the singly staggered model. An expression for the geometric factor, ψ, as given in equations (2.2.13) and (2.2.14), are given as:

$$\psi = 2 + 2cos\left[\frac{4\,\pi}{3} + \frac{1}{3}\,cos^{-1}(2\epsilon-1)\right], \tag{2.2.15}$$

for foamlike media.

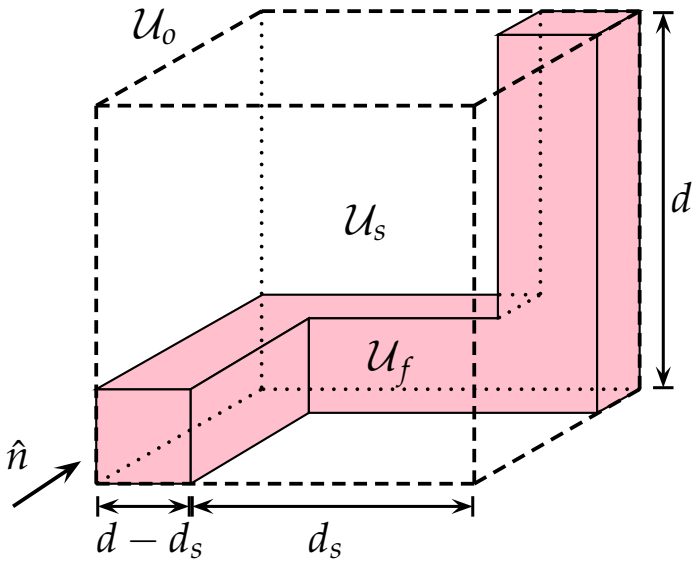

Figure 2.3: Doubly staggered RUC representation [4].

2.3 The Ergun equation

If only gas flow is considered from the bottom of a column, through the porous structure, the theory of fluid flow through granular porous media can be used. In industry the accurate prediction of the pressure drop through a porous packed bed is of importance. One such model has been developed by assuming that the packed bed can be treated as a collection of tangled tubes with arbitrary cross-sections. These crooked tortuous tubes are then approximated with theory developed for straight tubes [9]. The model is the so called *capillary model* and the Ergun equation [8] is one well known result of the capillary model. Even though the Ergun equation [8] has its origin in theory, empirical constants are also used in the final equation. Ergun's equation was fitted to data acquired using uniform spherical particles and thus empirical constants were added to the equation so that it would better match the data.

It was found that in the *laminar flow regime*, the pressure drop can be modelled by:

$$-\frac{dp}{dx} = \frac{150(1-\epsilon)^2\mu}{D_p^2\epsilon^3}q, \tag{2.3.1}$$

with D_p the diameter of a sphere with the same volume as the real particle. The empirically based constant is thus 150 in the Darcy regime and equation (2.3.1) is also known as the *Blake-Kozeny* equation [9].

In the *inertial flow regime* where recirculation dominate but turbulence is not yet present the so called *Burke-Plummer* equation [9] is used to predict the pressure drop as follows:

$$-\frac{dp}{dx} = \frac{1.75(1-\epsilon)\rho}{D_p\epsilon^3}q^2. \tag{2.3.2}$$

The empirically based constant in equation (2.3.2) is thus 1.75.

Again, using power addition the *Ergun equation* [8] can be formulated by adding the Blake-Kozeny equation (2.3.1) and the Burke-Plummer equation (2.3.2). This result not only

describes flow in the low and high velocity regimes but also gives a satisfactory result in the intermediate regime. The Ergun equation [8] is thus given as:

$$-\frac{dp}{dx} = \frac{150(1-\epsilon)^2\mu}{D_p^2\epsilon^3}q + \frac{1.75(1-\epsilon)\rho}{D_p\epsilon^3}q^2. \tag{2.3.3}$$

The empirically based constants compensate for the assumptions made in the capillary model. One assumption is that the porous medium is statistically uniform so that there is no channelling. Of course this is a crude assumption as channelling is common place in practical applications [9]. Another more practical assumption is that the column diameter is large in comparison to the particle dimensions ($d_p << d_c$). With any deviations from the assumptions made, the capillary model will probably yield inaccurate predictions. The Ergun equation [8] also assumes a uniform particle size distribution. Thus as better data becomes available, the modelling can be improved to represent a wider spectrum of packed beds [9].

Based upon the extensive investigation of numerous experimental data, the following improvement was suggested by Mcdonald et al. [17]:

$$-\frac{dp}{dx} = \frac{180(1-\epsilon)^2\mu}{D_p^2\epsilon^3}q + \frac{1.8\rho(1-\epsilon)}{D_p\epsilon^3}q^2. \tag{2.3.4}$$

The empirical origin of the Ergun and Mcdonald constants is based on spherical particles. Modelling flow through non-spherical particle can thus be expected to deviate from the predictions of the Ergun equations (2.3.3). In the following chapter the extent of the influence of these assumptions on the accuracy of the Ergun equation (2.3.3) is assessed in its application to irregularly shaped particles and non-uniform spherical particle size distribution powders.

Chapter 3

Geometrical aspects of packings

The main virtues of a good packing are a low pressure drop across the packing, a high porosity, a large specific surface area and a chemical resistance to the particular fluid [9]. The aim is to keep the costs involved as low as possible. The packing is best described by means of the porosity and the specific surface, where the specific surface is the total surface area of the packing per total packing volume. The great disadvantages of randomly dumped packings are poor distribution of both phases over the cross-section of the tower and in some cases large pressure drops [14]. Of course, the extent of the disadvantages differ from packing to packing.

Concepts widely used in porous packed columns are discussed in the current chapter with the aim to adapt and improve existing models.

3.1 Influence of packing shapes

The design of packing shapes remains an empirical art, as the pressure drop over the packed bed must be determined experimentally. Over the years many different packing shapes have emerged, but only a few are widely used. The oldest and still most commonly used packing is the Raschig ring. This packing element consists simply of a cylinder with its width equal to its height. It is mainly manufactured from ceramics, metals, plastics and carbon [22]. Since the Raschig ring modifications have been added to the ring, that mostly consist of internal partition. The modifications were an attempt to create a greater surface to volume ratio, higher porosity and a lower pressure drop across the packing. Some packing elements that followed the Raschig ring are the Lessing ring and the cross-partition ring, to name but a few. The Berl saddle is a packing element developed in the 1930's and was an improvement on the Raschig ring in that it has a larger surface to volume ratio. An example of a Berl element can be seen in Figure 3.1 (a). In the 1950's a significant improvement was made on the Raschig ring [14],the Pall ring. It consists of a cylinder with equal diameter and height but with ten holes punched into the sides resulting in ten fingers bending inwards as shown in Figure 1.2 (a). The resulting element has the same surface area as the Raschig ring but the total packing is much more permeable to the fluids [16]. Improvements on the Pall ring include packing elements like the Hy-Pak packing and creates a larger internal surface area inside of the cylinder. The Intalox Metal Tower Packing, IMTP, combines the advantages of the saddle shape with that of modern packing element designs, some of which are shown in Figure 1.2 (b).

Throughout history it is clear that a packing element's shape plays a large role in the effectiveness of a packed column. The effect of the shape on the pressure drop is quantified

(a) Intalox saddle (ceramic). (b) Tellerette packing (plastic).

Figure 3.1: Typical examples of modern random packings.

by the so called *shape factor.* The definition of the shape factor is discussed in the following sections using the concept of the *specific surface.*

3.1.1 Specific surface

The specific surface is of great importance in packed columns. It is a measure of the surface area per unite volume of the packing structure. The specific surface of a particle, a_v, is defined as:

$$a_v = \frac{s_{fs}}{V_p}, \tag{3.1.1}$$

with s_{fs} the contact area of a single particle with the fluid and V_p the volume of the same particle [9]. As an example the specific surface of a spherical particle can be calculated as follows: For a spherical particle $s_{fs} = \pi D_p^2$ and $V_p = \pi D_p^3/6$. It thus follows that:

$$a_v = \frac{6}{D_p}, \tag{3.1.2}$$

where D_p represents the particle diameter. Since $(1 - \epsilon)$ is the solid ratio in a packed bed it follows that the ratio of the total surface to the total packed bed volume is given as:

$$a = a_v(1 - \epsilon) = \frac{6}{D_p}(1 - \epsilon). \tag{3.1.3}$$

according to Geankoplis [9].

The concept of specific surface is of course applicable to all packings and various trivial empirical methods can be employed to determine the specific surface of a packed bed.

3.1.2 Specific surface of the RUC drag model

If it is assumed that the total volume of the packed section in a particular tower is divided into N equal volumes, the RUC model can be applied. Again, the smaller the particles are compared with the tower diameter, the more accurate this assumption, especially when one is trying to "fit" cubic cells into a cylinder. The volume of one REV would then be equal to $\mathcal{U}_o$ (refer to section 2.1). To calculate the specific surface, the geometrical characteristics of each

model will be used. Through trivial geometrical calculations the porosity, ϵ, and particle specific surface, s_{fs}, of each RUC can be calculated and thus the particle's specific surface can be determined. Multiplying the particle's specific surface, a_v, with the solid ratio of the packing, the total specific surface, a, is calculated. In Table 3.1 the expressions for the specific surface, a, are presented for the granular and foam RUC models.

	Granular	*Foam*
$\mathcal{U}_s = V_p$	d_s^3	$d^3 - (d - d_s)^2 (d + 2d_s)$
s_{fs}	$6d_s^2$	$12(d - d_s)d_s$
a_v	$\frac{6}{d_s}$	$\frac{12(d - d_s)d_s}{d^3 - (d - d_s)^2 (d + 2d_s)}$
$(1 - \epsilon)$	$\left(\frac{d_s}{d}\right)^3$	$3\left(\frac{d_s}{d}\right)^2 - 2\left(\frac{d_s}{d}\right)^3$
a	$\frac{6d_s^2}{d^3}$	$\frac{12(d - d_s)d_s}{d^3}$

Table 3.1: Specific surface of the RUC model.

3.1.3 Comparison with experimental data

Pressure drop experiments were conducted at the TUC in Porsgrunn, Norway. The packing materials used are described in Chapter 4. The glass Raschig rings used in some of the experiments were used to compare the theoretical equations, determining the specific surface, with the empirical values. For the glass Raschig rings it was determined that the nominal diameter (the diameter of a equivalent sphere), D_p, was equal to $0.0069m$. For the RUC model d_s and d were calculated to be $0.0068m$ and $0.0083m$ respectively. The bed had a porosity of 0.46, with a Sonntag correction equal to 0.2, which assumes that only 20% of the inner volume of a ring is available for flow. In Table 3.2 the comparison of the theoretical and experimental specific surfaces are given.

Experimental a	*Granular a*	*Foam a*	*Equation* (3.1.3)
454.73	485.21	214.06	466.08

Table 3.2: Comparison of theoretical and experimental values of glass Raschig ring's specific surfaces.

It is clear that both the granular RUC model [7] and equation (3.1.3) over-predict the specific surface. The reason for this over estimation is possibly due to the relatively large particles compared to the column diameter. The foam RUC model [4] severely under predicts the specific surface possibly because Raschig rings do not resemble a foamlike structure.

3.1.4 Shape factor or sphericity

In the case of irregular shaped packings, like those given in Figure 1.2, shape factors can be used to determine the equivalent diameter of a sphere with the same volume as the element or particle (nominal diameter). The sphericity, ϕ_s, of an element is the ratio of the surface of the equivalent sphere to the actual surface area of the element [9]. The equivalent sphere refers to a sphere having the same volume as the actual particle (see Appendix B). In Figure 3.3 a graphical explanation of the sphericity is given. To help understand the shape factor one can think of having a spherical ball clay. When the ball is formed into the shape of the packing element it will have a larger surface area but still the same volume (refer to Figure 3.3). The sphericity can thus be defined as:

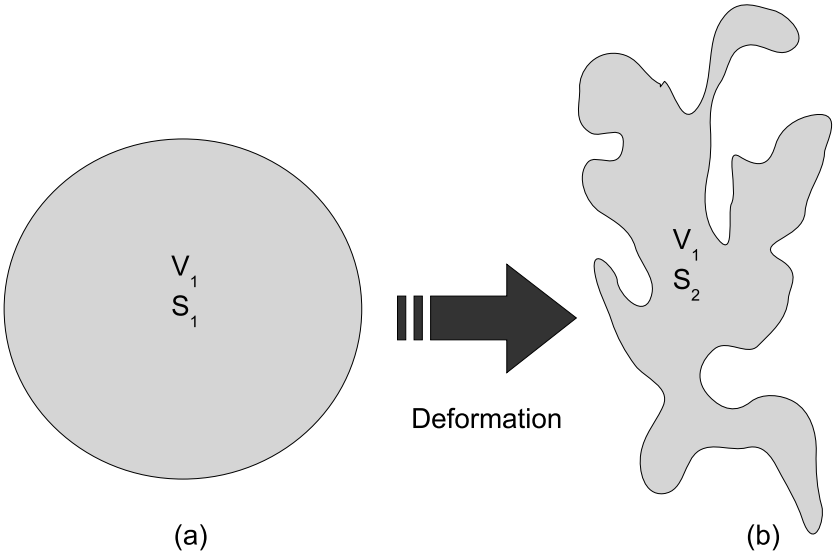

Figure 3.2: (a) A sphere with the same volume, V_1, as the actual particle, (b) irregularly shaped particle with volume equal to V_1.

$$\phi_s = \frac{\pi D_p^2}{s_{fs}}, \tag{3.1.4}$$

with D_p the equivalent sphere diameter and s_{fs} the actual packing element surface area. From equation (3.1.1) it follows that:

$$a_v = \frac{s_{fs}}{V_p} = \frac{\pi D_p^2/\phi_s}{V_p} = \frac{a}{(1-\epsilon)}, \tag{3.1.5}$$

and thus from equation (3.1.3) that:

$$a = \frac{\pi D_p^2}{V_p\,\phi_s}(1-\epsilon). \tag{3.1.6}$$

The volume of a sphere with a diameter of D_p has the same volume as the particular particle (per definition of nominal diameter). Thus equation (3.1.6) reduces to:

$$a = \frac{6}{\phi_s D_p}(1-\epsilon). \tag{3.1.7}$$

Table 3.3 provides well known sphericity values as presented by Geankoplis [9]. The ϕ_s values were calculated by Geankoplis [9] using equation (3.1.5).

Material	*Shape factor, ϕ_s*
Spheres	1
Cubes	0.81
Cylinders, $D_p = h$ $(length)$	0.87
Berl saddles	0.3
Raschig rings	0.3

Table 3.3: Sphericity of some packing elements [9].

In verifying the results given by Kolev [14], the specific surface of glass spheres were calculated using the definition of the specific surface. In Table 3.4 a few characteristics of some packing materials are given as presented by Kolev [14]. A discrepancy arises between the values calculated via the definition and the a-values given in Table 3.4. It was noted that the particle diameters were integer values. When the number of particles per unit volume and specific surface where used to calculate D_p, it was found that the values were rounded too much to allow accurate back substitution. To recalculate D_p the porosity is written as follows:

$$\epsilon = \frac{U_f}{U_o} = \frac{1-U_s}{U_o} = \frac{1-N\mathcal{U}_s}{U_o}, \tag{3.1.8}$$

with $\mathcal{U}_s$ the volume of one solid particle. In this particular case it is the volume of a sphere. If N represent the number of particles in a cubic meter of the packing volume it follows that $U_o = 1m^3$. So for a spherical particle it follows that:

$$\mathcal{U}_s = \frac{1-\epsilon}{N} = \frac{\pi D_p^3}{6}. \tag{3.1.9}$$

From equation (3.1.9) the nominal diameter, D_p, can be expressed as:

$$D_p = \sqrt[3]{\frac{6(1-\epsilon)}{\pi N}}. \tag{3.1.10}$$

The results of Table 3.4 were confirmed only for the glass spheres as it is the only geometrical shape that can easily be described analytically. In general the nominal diameter is given by the following relation:

$$D_p = \sqrt[3]{\frac{6V_p}{\pi}} \tag{3.1.11}$$

and from equation (3.1.5) it can be written as:

$$D_p = \sqrt[3]{\frac{6\, s_{fs}(1-\epsilon)}{\pi a}}. \tag{3.1.12}$$

Packing	*Material*	*Size of particle* [mm]	N [$1/m^3$]	a [m^2/m^3]	a, *with eqn.* (3.1.7) [m^2/m^3]	ϵ [m^3/m^3]
Pall ring	Metal	50	6242	112.6		0.951
		38	15772	149.6		0.952
		35	19517	139.4		0.965
		25	53900	223.5		0.954
		15	229225	368.4		0.933
Pall ring	Plastic	50	6765	111.1		0.919
		35	17000	151.1		0.906
		25	52300	225.0		0.877
Pall ring	Ceramic	50	6215	116.5		0.783
Raschig ring	Ceramic	50	5990	95.0		0.830
		38	13275	118.0		0.680
		25	47700	190.0		0.680
		15	189091	312.0		0.690
		13	378000	370.0		0.640
		10	672000	440.0		0.650
		8	1261000	550.0		0.650
		6	3022936	771.9		0.620
Raschig ring	Metal	15	260778	378.4		0.917
Raschig ring	Carbon	25	50599	202.2		0.720
		13	378000	370.0		0.640
Sphere	Glass	25	66664	134.5	134.802	0.430
		13	561877	282.2	283.878	0.400

Table 3.4: Geometrical characteristics of random packings according to Kolev [14] and the verification of data according to equation (3.1.7).

Thus if the nominal diameter is to be calculated, either the particle volume or the particle surface must be known by means of empirical methods. Another possible expression for the nominal diameter can be formulated from equation (3.1.10) in terms of the total packing volume, U_o. Equation (3.1.12) leads to the nominal diameter:

$$D_p = \sqrt[3]{\frac{6(1-U_o\epsilon)}{\pi N}}. \tag{3.1.13}$$

In the latter equation only the total bed volume, porosity and number of particles in the bed is required.

From equation (3.1.7) the arithmetical diameter can be derived. If spherical particles are assumed, the shape factor, ϕ_s, is equal to one. In this situation the diameter $D_p = D_a$, where D_a is called the arithmetic diameter [14]. The arithmetic diameter is the diameter of spheres

which will produce the same porosity and specific surface as an actual packing [14]. It then follows that:

$$D_a = \frac{6(1-\epsilon)}{a}, \tag{3.1.14}$$

where ϵ and a are the porosity and specific surface of the actual packing respectively.

3.1.5 Granular RUC model, shape factor

To make the RUC model more flexible for irregular shaped particles a shape factor was defined. The granular RUC shape factor is defined similarly as in equation (3.1.4). Instead of using a sphere with equivalent volume, a cube is now used. Thus the granular model shape factor is defined as the ratio of the surface of a cube with the same volume as the particle, over the actual surface area of the particle. The definition of the granular shape

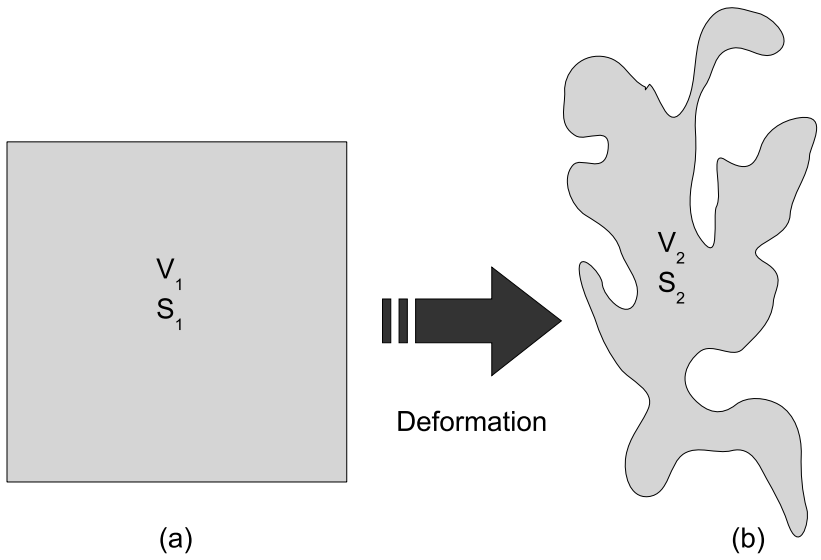

Figure 3.3: Schematic explanation of the shape factor in terms of the granular RUC model. (a) Cube with volume V_1 and (b) irregular shaped packing element with the same volume, $V_1 = V_2$.

factor is given as:

$$\phi_{gran} = \frac{6d_{gV}^2}{s_{fs}}, \tag{3.1.15}$$

with d_{gV} the length, breadth and height of the cube with the equivalent volume of the particle.

Following the same procedure as in section 3.1.4 the specific surface, a, can be expressed in terms of the granular RUC shape factor as follows:

$$a = \frac{6}{\phi_{gran}\, d_{gV}}(1-\epsilon). \tag{3.1.16}$$

Using equation (3.1.1) the volume of a particle can be expressed as:

$$V_p = \frac{s_{fs}(1-\epsilon)}{a}. \tag{3.1.17}$$

From the definition of the equivalent cube it follows that the particle and the equivalent cube has the same volume, namely d_{gV}^3. Using equation (3.1.8) it can be shown that the equivalent cubic dimension is given by:

$$d_{gV} = \sqrt[3]{\frac{(1-\epsilon)}{N}}, \tag{3.1.18}$$

given a cubic meter of packed section.

If the packing volume is divided into N volumes, the dimension of a granular RUC cube will be d (refer to section 2.1.2). Hence for $1m^3$ of packing d is given by:

$$d = \frac{1}{N^{1/3}}, \tag{3.1.19}$$

and it can be shown that d_s is then expressed as:

$$d_s = d(1-\epsilon)^{\frac{1}{3}} \tag{3.1.20}$$

$$= \sqrt[3]{\frac{(1-\epsilon)}{N}}. \tag{3.1.21}$$

Thus, given the definition of an equivalent cube, it follows that $d_{gV} = d_s$, given the packing volume is divided into N equal volumes and $U_o = 1$. If another packing volume is used, as in most practical cases, the particular volume must be included in the calculations. Equation (3.1.20) would then become:

$$d_s = \sqrt[3]{\frac{(1-\epsilon)U_o}{N}}, \tag{3.1.22}$$

with U_o the total packed bed volume. A general expression for the equivalent cubic dimension can also be formulated by not assuming $U_o = 1$ in equation (3.1.18) and hence is given by:

$$d_{gV} = \sqrt[3]{\frac{(1-\epsilon U_o)}{N}}. \tag{3.1.23}$$

As with the nominal diameter, the equivalent cubic dimension can also be expressed as:

$$d_{gV} = \sqrt[3]{\frac{s_{fs}(1-\epsilon)}{a}}. \tag{3.1.24}$$

Hence a variety of parameters can be used to determine the equivalent cubic dimension, depending on the information available.

Chapter 4

Experiments

4.1 Experimental setup

An experimental setup was built to validate the mathematical models that were described in the previous chapters. It consisted of a vertical tube with a diameter of $7cm$ and a height of $1m$. Nine different probes were inserted into the tube to measure the pressure at the particular points with respect to atmospheric pressure. Air was used as the gas phase, at atmospheric pressure and at a temperature of 20^oC. The assumption was made that CO_2 would behave the same as air as it moves through the packed bed. A pump providing normal air flow was available at the TUC. The use of CO_2 would have been more expensive.

The experimental rig is shown in Figure 4.1. The tower is connected to a detection system that converts a pressure into an electric signal. This signal is then sent to a computer where the signal is interpreted. It was found that with a pressure of $0psi$ an electrical signal of $1.6V$ was produced. The maximum voltage difference that the detector can produce is $5V$ and the maximum pressure that can be detected is $2psi$. With this data a linear interpolation was made to find a relationship between voltage readings and the corresponding pressure readings. These calibrations were taken into consideration when using the interface programme between the detectors and the computer. The pressure detectors that were used were made by *Honeywell sensing and control* [11], and were from the 140*/160/180 and 240PC* series. In this experiment a porous metal plate was used to create an almost uniform profile (see Figure 4.2). This is done because it is simpler to do numerical simulations with a uniform entry profile. In industry it is also common that a uniform entry profile is assumed when a fluid enters a porous packed section. Distributors are also used to ensure that the gas is uniformly spread over the cross section of the column. This is very important as a uniform distribution of the gas will help to combat channelling [5]. In the experimental setup, the gas flow can only be controlled by means of the gas flow rate, in other words in l/min. Knowing the column diameter, all of the flow rate measurements were converted into superficial velocities by means of trivial calculations.

A series of different packed beds were then inserted into the tower and were subjected to a range of different superficial velocities. Pressure readings were recorded alongside the altering superficial velocities and all of the experimental data were compared with theoretical and numerical approximations. The packing elements used are commonly used in industry. The packing material were provided by the TUC and all of the experiments were conducted there. The packing materials were weighed and then poured randomly into the tower. The porosity was then calculated using the volume of the resulting packing, its weight and the density of the substance of the packing material used. In Table 4.1 data for the packing struc-

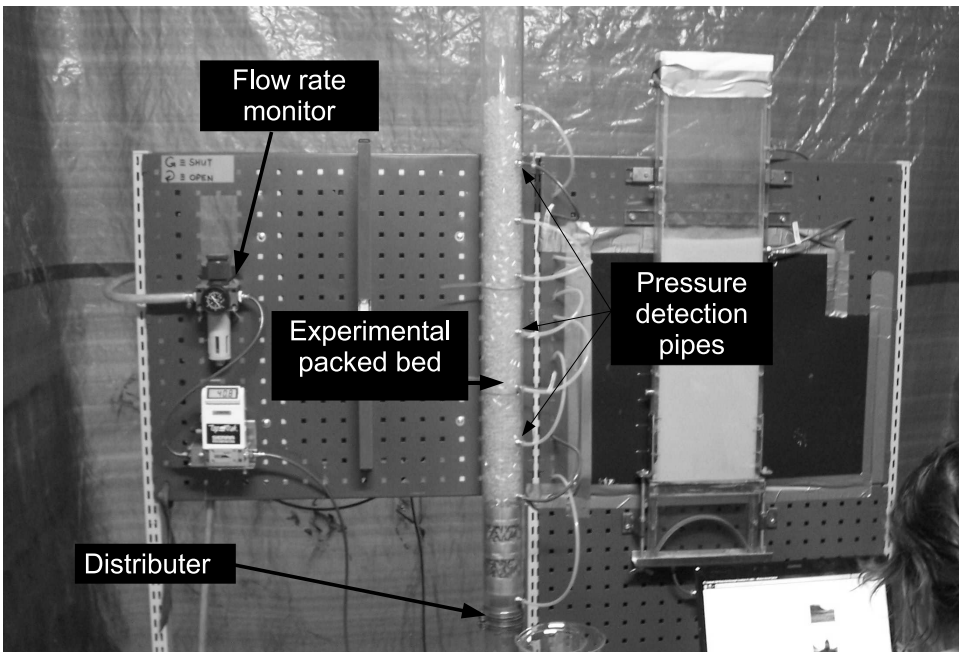

Figure 4.1: Experimental setup built at the TUC in Porsgrunn, Norway.

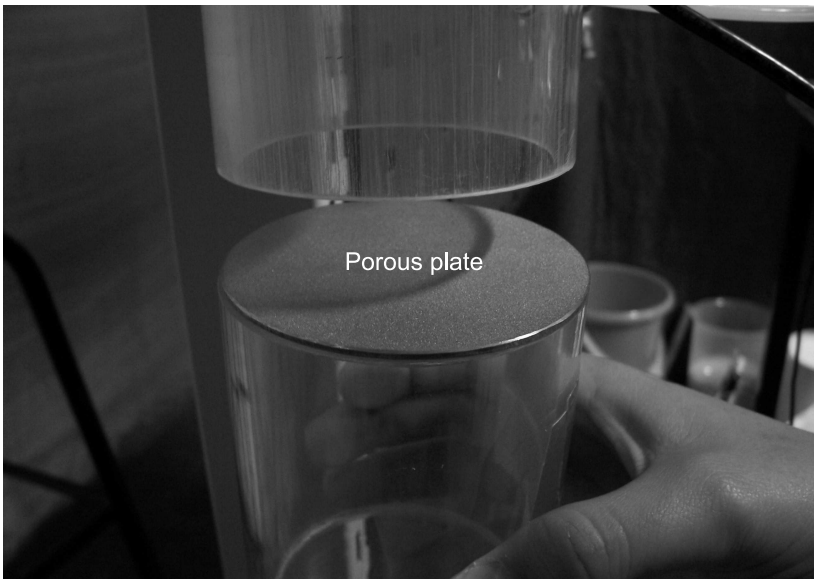

Figure 4.2: A distributor used in the experimental setup to create an almost uniform velocity profile.

tures created is given. Further specifications of the packing materials mentioned in Table 4.1 are discussed in the following two sections.

Packing material	Material	Packing height [m]	Packing volume [m^3]	Packing weight [g]	Porosity [-]
Raschig rings	Glass	0.72	0.00275	2025,83	0.71
Raschig rings	Metal	0.98	0.0037	3412	0.86
Intalox saddles	Metal	0.76	0.0029	923	0.95
Spherical particles	Glass				
$100 - 200\mu m$		0.978	0.00376	6084	0.35
$400 - 600\mu m$		0.922	0.0035	5935	0.32
$750 - 1000\mu m$		0.88	0.00338	5736	0.31

Table 4.1: Parameters of the Raschig rings used in the experiments.

4.2 Raschig rings

In Figure 4.3 examples of glass and metal Raschig rings are given. A Raschig ring is one of the first random packings used (1895-1950) and is still widely used today [14]. Second and third generation random packings like the Pall ring and the Nutter ring are all based on the Raschig ring design. Two types of Raschig rings were used in experiments, as mentioned in Table 4.1, and further physical characteristics of the Raschig rings used are provided in Table 4.2. The particles were weighed to determine the particular materials density and by using

Packing material	Material	Physical dimentions $(l \times b \times h)$[m]	Particle volume [m^3]	Particle surface [m^2]
Raschig rings	Glass	$0.007 \times 0.007 \times 0.009$	1.69×10^{-7}	3.7×10^{-4}
Raschig rings	Metal	$0.01 \times 0.001 \times 0.01$	1.49×10^{-7}	6.2×10^{-4}

Table 4.2: Parameters of the different packing structures used in the experiments.

the particle density and the bulk density, the porosity was determined. The glass- and metal Raschig ring's density were found to be $2.52 \times 10^3 kg/m^3$ and $6.59 \times 10^3 kg/m^3$ respectively. An example of Intalox saddles and the two kinds of Raschig rings used in the present study is given in Figure 4.3.

Raschig rings are a typical example of packing elements used in fixed bed reactors. Today there exists packing materials that are much more efficient than the classic Raschig rings, but successful modelling of flow through Raschig rings can lay a foundation for flow modelling through more complex packings. The Intalox saddle is one such complex irregularly shaped packing material that creates a very low pressure drop compared to that of the classical Raschig ring (refer to Figure 4.3 (c)).

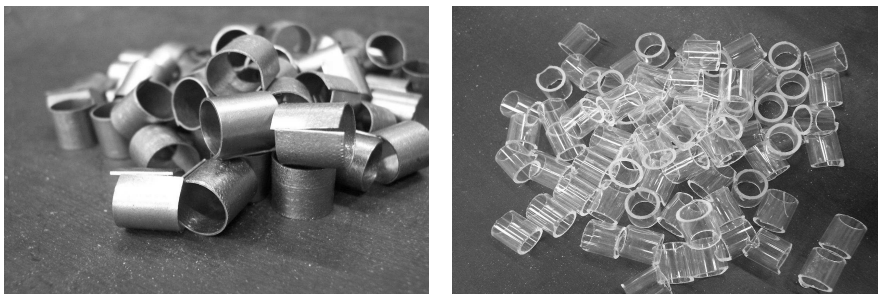

(a) (b)

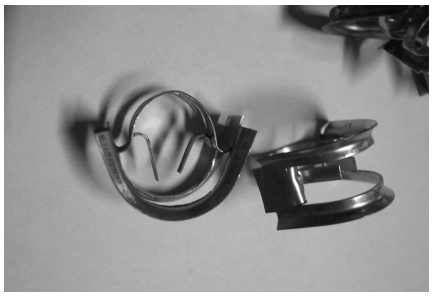

(c)

Figure 4.3: (a) Metal Raschig rings, (b) glass Raschig rings and (c) metal Intalox saddles packings.

4.3 Spherical glass particles

The motivation behind the use of spherical particles as packing elements is based on the Ergun equation (2.3.3). The Ergun equation is widely accepted to be accurate in predicting flow behavior in packed beds consisting of uniform spherical particles [8]. The spherical particles were thus used to confirm the Ergun equation (2.3.3), as well as to validate the experimental setup. Spherical particles are also popular in many types of reactors in the industry. Although it is not widely used for CO_2 absorption at present, better knowledge and understanding of these reactors may lead to its use in this particular field in the future. In Figure 4.4 a close-up photograph of spherical glass particles is given. All of the spherical particle beds used consisted of a range of particle sizes and were not uniform particle beds. Thus the data is expected to deviate from what the Ergun equation predicts.

According to Sookai [21] the pressure drop over the distributor (the porous plate in this case) must be greater than 30% of the total pressure drop across the bed. This criterion is introduced to prevent stagnant regions in the packed bed. This is only applicable in packed beds consisting of fine materials as described in the *Geldart's powder classification diagram* [21]. In the experimental setup pressure drops of 14.82% and 30.39% were calculated at a flow rate $50l/s$ across the distributor for the $400-600\mu m$ and $750-100\mu m$ size glass powders respectively. The pressure drop across the distributor was calculated at a flow rate of $50l/s$. The flow through the $100-200\mu m$ powder never reached such high flow rates and thus the percentage pressure drop across the distributor to the total pressure drop could not be calculated. According to Sookai [21] the experiment was in danger of forming stagnant regions.

It is common practice in the industry to use a mean particle diameter when working with particle size distributions. This help's to characterize the material. Some of the most common definitions are the *linear mean diameter*, *the area mean diameter*, *the volume mean di-*

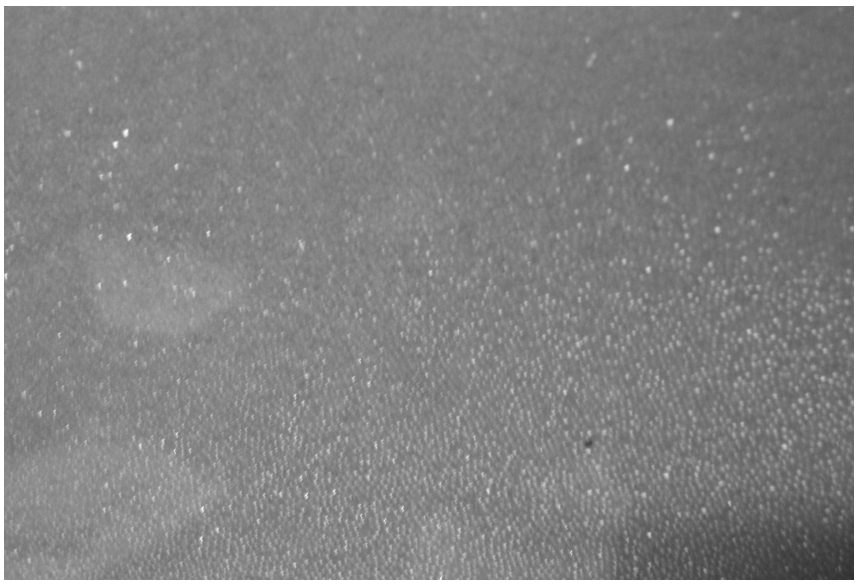

Figure 4.4: Photographic example of spherical glass particles. These particles vary between $750 - 1000\mu m$.

ameter and the *surface-volume mean diameter*. The *linear mean diameter* is common place and is trivially defined as:

$$\overline{d}_L = \frac{\sum_i d_i}{N}, \tag{4.3.1}$$

with d_i all of the particle diameters in the bed and N the total number of particles in the bed.

To be able to define the *surface, volume* and *surface-volume* mean diameters, two new shape factors have to be defined. The first is the *volume shape factor* and is defined as:

$$V_p = \Psi_V d_i^3, \tag{4.3.2}$$

with d_i the diameter of the particular particle. In equation (4.3.2) the volume shape factor is represented by Ψ_V. Similarly, the *surface shape factor* is defined as:

$$s_{fs} = \Psi_A d_i^2. \tag{4.3.3}$$

Using equation (4.3.2) and (4.3.3) the surface, volume and surface-volume mean diameters can now be derived. To determine the volume mean diameter the following definition is used:

$$U_o = \Psi_V \overline{d}_V^3 \times N, \tag{4.3.4}$$

with $\overline{d}_V$ the volume mean diameter. Quantifying equation (4.3.4) in terms of all of the incremental mean particle diameters it follows that:

$$\begin{aligned} U_o &= \sum_i (U_o)_i \\ &= \sum_i N_i \times \Psi_V d_i^3 \\ &= \sum_i \frac{M_i}{m_{pi}} \times \Psi_V d_i^3 \\ &= \sum_i \frac{M x_i}{\rho \Psi_V d_i^3} \times \Psi_V d_i^3, \end{aligned} \tag{4.3.5}$$

with M_i the mass in a particular range, m_{pi} the mass of a particle in that range and M the total mass of the powder. The fraction of each range's mass with respect to the total mass of the powder is represented by x_i. The total volume can thus trivially be reduced to the following expression:

$$U_o = \frac{M}{\rho} \sum_i x_i. \tag{4.3.6}$$

The number of particles in the bed can be expressed as:

$$N = \sum_i \frac{M x_i}{\rho \Psi_V d_i^3}. \tag{4.3.7}$$

Using equations (4.3.4) and (4.3.7) the total volume can be expressed as:

$$U_o = \Psi_V \overline{d}_V^3 \sum_i \frac{M x_i}{\rho \Psi_V d_i^3}. \tag{4.3.8}$$

From equations (4.3.6) and (4.3.8) the volume mean diameter is expressed as:

$$\overline{d}_V = \left[\frac{\sum_i x_i}{\sum_i \frac{x_i}{d_i^3}} \right]^{\frac{1}{3}}. \tag{4.3.9}$$

The surface mean diameter can be derived similarly to the previous derivation and the following expression for the mean surface diameter is found:

$$\overline{d}_A = \left[\frac{\sum_i \frac{x_i}{d_i}}{\sum_i \frac{x_i}{d_i^3}} \right]^{\frac{1}{2}}. \tag{4.3.10}$$

Finally using equations (4.3.9) and (4.3.10) and knowing that $\sum_i x_i = 1$, the surface-volume mean diameter is given as [10]:

$$\overline{d}_{sv} = \frac{1}{\sum_i x_i / d_i}. \tag{4.3.11}$$

The particle distribution of the $400 - 600\mu m$ spherical particle powder is given in Figure 4.5. The particle size distribution was determined by means of sieve analysis as described in Appendix A. When equation (4.3.11) is implemented with respect to the particle's mass fraction distribution, it follows that the nominal size (approximated by $\overline{d}_{sv}$) should be $482.9\mu m$ (refer to Figure 4.5).

Another definition is one that follows from the cumulative percentage mass fraction and is simply the average particle diameter that correlates with 50% of the total mass fraction (refer to Figure 4.6). According to the cumulative sum method a nominal size (D_{avg}) of $458\mu m$ is prescribed. Both methods thus give results that are in good agreement with one another.

From Figure 4.5 it is evident that even though the manufacturers claimed that the particle size distribution is only between 400 and $600\mu m$, particles with a smaller diameter were

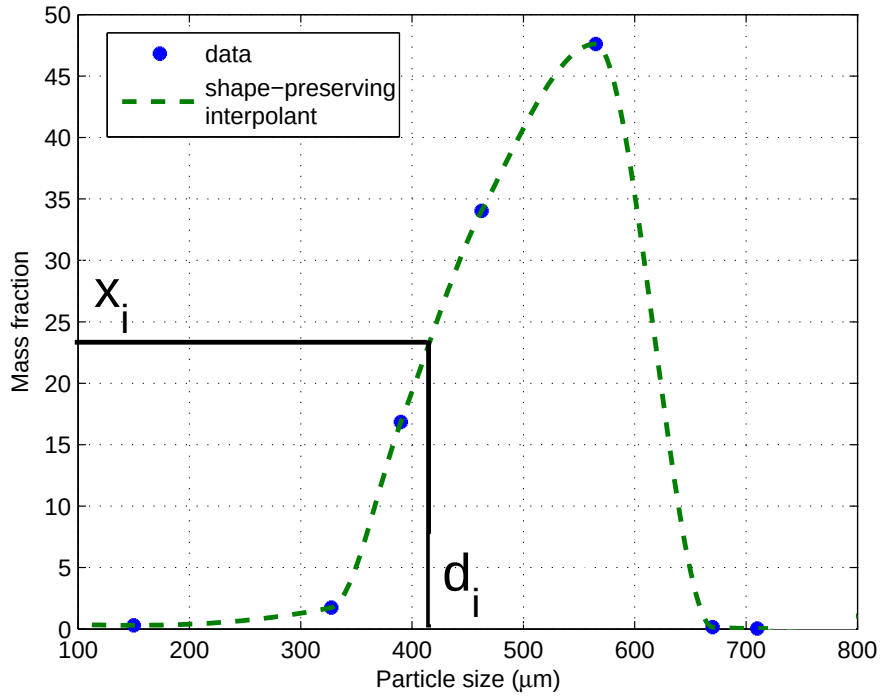

Figure 4.5: Distribution of particles sizes determined using sieve analysis as described in Appendix A.

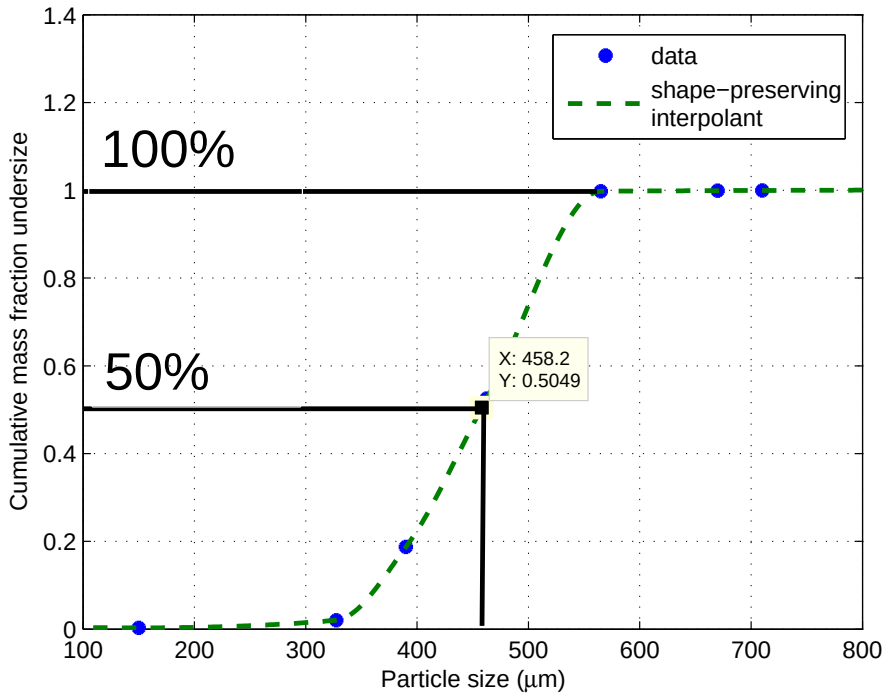

Figure 4.6: Cumulative sum of the mass fraction of particles under a particular diameter size for spherical glass particles with diameters between $400 - 600\mu m$.

measured via sieving analysis. This can also cause unforseen effects in the data retrieved from the powders.

Sieving analyses were only performed on the $400 - 600\mu m$ powder so the preceding analyses could not be performed on the other two powders.

Chapter 5

Applications

5.1 Pressure drop through random dumped packings

Accurate predictions of the pressure drop in a packed tower is of great importance in the industry. Packed bed reactors are the most widely used reactors. Their popularity is due to their low operation cost and high effectivity [19]. Since knowledge of the pressure drop in a packed bed is crucial to the effectiveness of a particular tower it should be modelled with great accuracy. Single-phase flow theory also forms the basis of two phase flow studies which is crucial in almost all of the industrial applications of packed beds.

5.1.1 Existing models for predicting single phase flow through porous media

To quantify the accuracy of the RUC model (section 2.1.2) and the Ergun equation, (equation (2.3.3)), empirical equations presented by Kolev [14] were used. Four empirical equations and tables of empirically determined constants are presented to calculate the pressure drop through a porous packed bed [14].

In comparing the models described, it was found that none of the packings that were used in this work were represented by the tables of empirical data that were provided. Most of the equations required empirical constants, so that when the packing used in this work was not listed, comparisons could not be made. The latter were the biggest problem faced with while trying to predict flow through porous media. The need for better models is highlighted by the difficulties in obtaining the empirical constants. Ideally one would like to derive theoretical equations entirely independent of empirical constants.

The first of these is:

$$\frac{\Delta p}{L} = \xi \frac{\rho q^2 a}{8\epsilon^3}, \tag{5.1.1}$$

with q the magnitude of the superficial velocity, L the packed bed depth, ρ the gas density, a the specific surface, ϵ the porosity and ξ a coefficient that takes into account the pressure drop caused by friction as the gas is moving through the packed bed and the pressure drop caused by the changing in direction of the gas as it makes its way through the packing [14]. To determine ξ the following equation was recommended [14]:

$$\xi = \frac{133}{Re_G} + 2.34, \tag{5.1.2}$$

where Re_G is the Reynolds number for the gas phase and is given by:

$$Re_G = \frac{q d_h \rho}{\mu \epsilon}. \tag{5.1.3}$$

The hydraulic diameter of the packing, d_h, is defined as:

$$d_h = \frac{4\epsilon}{a}. \tag{5.1.4}$$

Equation (5.1.4) can be applied to any packing since no empirical constants are required. No reference was made to how the equation was derived. Nevertheless it was compared to the Ergun equation [8] and the RUC model [7] [4] using data acquired from glass Raschig rings (as described in Chapter 4). The comparison is presented in Figure 5.1. Clearly none of the models predict the flow behavior through the Raschig rings accurately by using the porosity and specific surface alone. The coefficient that characterizes the type of packing, ξ, clearly fails to do so. Further investigation into equation (5.1.1) was not conducted as no reference to its derivation was provided. In the book of Kolev [14] a number of other models are also presented without reference to their origin. They will not be discussed as they could not be assessed properly. The following pressure drop equation is presented by Kast [12]:

$$\frac{\Delta p}{L} = \frac{K_w (1-\epsilon) q^2 \rho_G}{\epsilon^3 D_p} \left(\frac{64}{Re_G} + \frac{2.6}{Re_G^{0.1}} \right), \tag{5.1.5}$$

where K_w is the so called way factor, dependent on the type of packing elements used and is a measure of the average tortuous path of the gas over the bed height. In Table 5.1 some values of K_w are given for a few different packing elements. The Kast equation (5.1.5) could not be compared to the Ergun equation and the RUC model. The reason for this is because the packings used in this work are not represented in Table 5.1. Thus the appropriate value for the way factor, K_w, is not known.

The next empirical equation is an equation presented by Billet [1]:

$$\frac{\Delta p}{L} = C_d \left(q \sqrt{\rho_G} \right)^e. \tag{5.1.6}$$

The experimental constants, C_d and e, also depend on the packing used and some values of these constants are presented in Table 5.2 as given by Kolev [14]. All of the particles in Table 5.2 have a nominal size of $50mm$. The constants in equation (5.1.6) take into account the porosity of the packed bed as well as the packing's dimensions. None of the packings used in this work are represented in Table 5.2, so no comparison with or assessment of equation (5.1.6) could be made.

In equation (5.1.7) a relationship between the pressure drop and the superficial velocity in a packed bed is given, as developed by Darcy and Weibach [8]. It gives the pressure drop in a non-perforated channel with diameter d_h and length L (capillary model), namely:

$$\frac{\Delta p}{L} = \lambda \frac{q^2}{2\epsilon^2 d_h} \rho. \tag{5.1.7}$$

Here λ is called the resistance coefficient and d_h is called the hydraulic diameter and is defined as:

$$d_h = \frac{2\epsilon d_p K}{3(1-\epsilon)}, \tag{5.1.8}$$

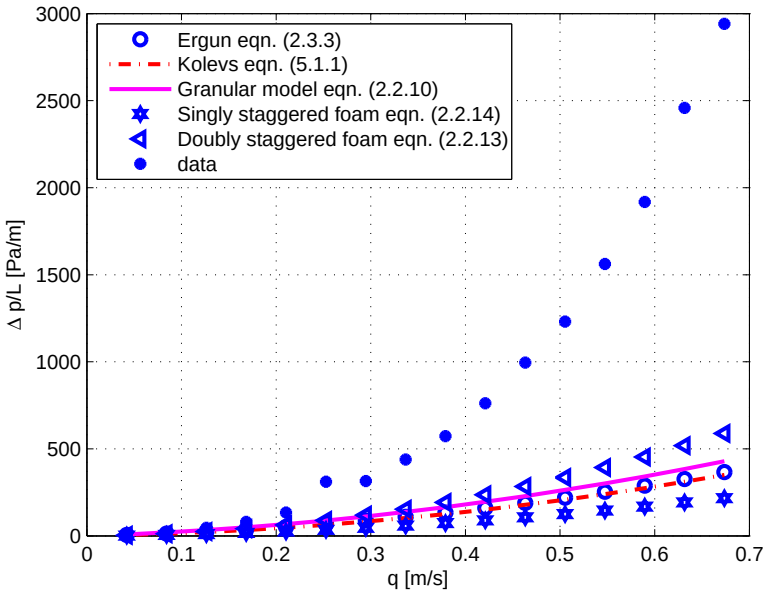

(a)

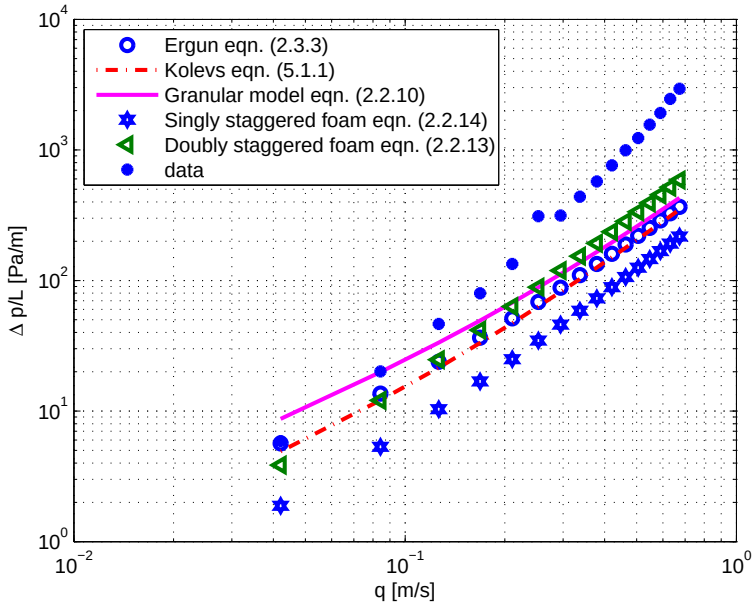

(b)

Figure 5.1: (a) Comparison of the RUC model [7] [4] and the Ergun equation [8] with equation (5.1.1) and (b) the previous comparison but on a log-log axis.

in the work by Mackowiak [15]. In equation (5.1.8) d_p represents the particle diameter and is defined as:

$$d_p = \frac{6(1-\epsilon)}{a}. \tag{5.1.9}$$

The K in equation (5.1.8) is called the wall factor and is given as:

$$K = \left(1 + \frac{2d_p}{3(1-\epsilon)d_s}\right)^{-1}, \tag{5.1.10}$$

Packing	Size [mm]	ϵ	K_w
Berl Saddle	50×50	0.725	1.93
	35×35	0.705	1.8
	35×35	0.75	1.95
	25×25	0.75	1.8
	15×15	0.758	1.95
Intalox Saddle	50×50	0.78	2.05
	35×35	0.74	1.95
	35×35	0.76	1.9
	35×35	0.978	2.04
	25×25	0.732	1.8
Pall Ring	50×55×5	0.77	2.2
	35×35×4	0.755	2.5
	35	0.773	2.1
	35	0.95	1.9
	25	0.742	1.75
Raschig Ring	50×55×5	0.77	3.35
	35×35×4	0.755	3.6
	35	0.773	3.2
	30	0.755	3.1
	25	0.705	3.1
	15	0.69	3.6
	15	0.657	3.1
Ceramic Ring	25.3×25.3×3.5	0.75	3.4
	25×15.9×3.5	0.743	3.5
	23.3×19.9	0.75	2.85
	23.3×10.9×3.5	0.75	2.82

Table 5.1: The way factor, K_w, for different packings according to Kolev [14].

and can be set equal to one for structured packings. Substituting equation (5.1.8) and (5.1.10) into equation (5.1.7) gives:

$$\frac{\Delta p}{L} = \lambda \frac{3(1-\epsilon)q^2\rho}{2\epsilon^3 d_p K}. \tag{5.1.11}$$

Setting $\psi = \frac{3}{2}\lambda$ and $F_v = q\sqrt{\rho}$, equation (5.1.11) yields:

$$\frac{\Delta p}{L} = \psi \frac{(1-\epsilon)F_v^2}{\epsilon^3 d_p K}. \tag{5.1.12}$$

The resistance coefficient, ψ, is defined empirically. In the work by Mackowiak [15], two well known correlations for the resistance coefficient are given. The major draw back of these correlations, is that they depend on empirically defined constants. The packings used in this work were not represented in the supplied tables and the result was that the resistance coefficient could not be determined for the packings used.

Packing	Material	C_d	e	N
Pall ring	Metal	5.5	1.85	6358
	Plastic	6.15	1.864	6765
	Ceramic	8.8	1.896	6455
Nor Pac ring	Plastic	2.15	1.83	7119
Hiflow ring	Metal	2.6	1.86	4739
	Plastic	2.6	1.96	6723
	Ceramic	4.5	1.89	4630
Hiflow saddle	Plastic	2.32	1.95	9939
Top pak	Metal	4.3	1.91	6950
Dinpak	Plastic	2.35	1.95	6700
Ralu ring	Plastic	2.35	1.99	5913
Intalox saddle	Plastic	7.0	1.98	8656
	Ceramic	7.0	1.88	8180

Table 5.2: Experimental constants as required by Billets equation (5.1.6).

The last empirical equation presented by Kolev [14] is another formulated by Billet [1] and is given as:

$$\frac{\Delta p}{L} = C_P \left(\frac{64}{Re_{Gl}} + \frac{1.8}{Re_{Gl}^{0.08}} \right) \frac{a}{\epsilon^3} \frac{F_v}{2} \frac{1}{K_p}, \tag{5.1.13}$$

where

$$\frac{1}{K_p} = 1 + \frac{2}{3} \frac{1}{1-\epsilon} \frac{D_a}{d_c}, \tag{5.1.14}$$

and

$$Re_{Gl} = \frac{qD_a}{(1-\epsilon)\mu\epsilon}. \tag{5.1.15}$$

The arithmetical diameter, D_a, is the equivalent diameter of spheres that would create the same porosity and specific surface as the real packing. The constant d_c in equation (5.1.14) refers to the column diameter. As the Ergun equation and RUC model do not take into account the effects of the column wall but assume a very large column compared to the element size, the value of d_c may present a problem in this study's particular application as the column had a diameter of only $7cm$. Table 5.3 gives a few parameters of some packings, as well as the corresponding values of C_P. This work's packings are not represented in Table 5.3. Thus no correlation between the data collected in the present study and equation (5.1.13) could be made.

The few equations that were briefly discussed in this section emphasizes the need of a general equation for modelling flow through packed beds. Of course, if tables are studied, like the ones in this chapter, before packing materials are bought the correct empirical data will be available and the problem with empirical constants will not arise. To take into account all of the physical effects that can exist in different packings is no trivial task. Therefore an adaptive model not depending on experimental constants would be very useful in the industry.

According to Nemec [19] the Ergun equation [8] systematically under predicts the pressure drop for packed beds consisting of non-spherical particles. The Ergun equation [8] has been adapted by Nemec to take into account phenomenological and empirical analysis

Packing	Material	Nominal size $[mm]$	N $[1/m^3]$	a $[m^2/m^3]$	ϵ $[m^3/m^3]$	C_P
Pall ring	Metal	50	6242	112.6	0.951	0.763
		35	19517	139.4	0.965	0.967
		25	53900	223.5	0.954	0.957
	Plastic	50	6765	111.1	0.019	0.698
		35	17000	151.1	0.906	0.972
		25	52300	225	0.887	0.865
	Ceramic	50	7502	155.2	0.754	0.233
Telerete	Plastic	25	37037	190	0.93	0.538

Table 5.3: Some characteristic data and constants for randomly dumped packings according to Kolev [14] .

to better describe the pressure drop through non-spherical packed beds [19]. Nemec has claimed that this approach is far superior to any other method available at that time [19].

Mackowiak developed a new method based on the extended channel model to determine the pressure drop in packed beds [15]. Using this new method no empirical data is required for packings with simple shapes and the pressure drop can thus be calculated theoretically (as is the case with Raschig rings). This model was also verified for a large range of different packing materials including Raschig rings. It should also be mentioned that geometrical data, like the specific surface and porosity, is required by Mackowiak's equation. Mackowiak's pressure drop equation is also only valid in the range of $Re_v \in (200, ..., 2000)$.

In the following two sections Nemec's and Mackowiak's improvement on the pressure-drop predictions through random dumped packings will be discussed and data acquired at the TUC.

5.1.2 Description and assessment of Nemec's [19] model for single phase flow through packed beds.

5.1.2.1 Description

In industry most researchers have accepted the fact that the Ergun constants must be determined empirically for every bed used. Even the well known correction of McDonald [17] is only a limited correction and cannot account for all non-spherical particles' pressure-drop. It has been shown that the column to wall diameter ratio (d_c/d_p) should be greater than 10 [19]. If this criteria is met then the effect of the wall upon the pressure drop can be neglected. Both of the Raschig rings used in this work had values of approximately ten for this ratio. Thus wall effect are not necessarily a negligible effect on the overall pressure drop [19]. The experimentally determined constants for the Ergun equation do not take into account wall effects. Thus Nemec's equation holds only for packing with a particle-to-column ratio that is greater than 10.

Nemec claimed that, instead of finding general constants for the Ergun equation, packings should be treated as families. In other words packings within the same family of shapes should be treated with more or less the same constants in the Ergun equation. The ring packings were one of the first packings that showed that the change in specific surface (sur-

face per volume) is not enough to compensate for different shapes of packings. The Ergun equation consistently under estimated the pressure drop. Sonntag [20] postulated that there might exist dead zones in the flow through rings. After experimental correlations he stated that only approximately 20% of the inner volume of the ring is available for flow. The effect of the decrease in the volume available for flow is a decrease in the porosity (as seen by the fluid). A small change in the porosity has a large impact on the pressure drop and thus this effect can have a large influence on the pressure drop, predicted by the models. This stagnant region within the rings can also be the reason for the under prediction of the Ergun equation. Applying Sonntag's correction [18] in the derivation of the Ergun equation is briefly discussed in the following subsection.

5.1.2.2 Derivation of the corrected Ergun constants for flow through rings as described by Nemec [18].

In determining the modified Ergun constants the concept of the hydraulic radius is required. The hydraulic radius is used in the derivation of the capillary model rather than the radius of a circular tube. For particles with uniform shape and size the hydraulic radius can be defined as:

$$
\begin{aligned}
r_h &= \frac{cross\ section\ available\ for\ flow}{wetted\ perimeter} && (5.1.16)\\
&= \frac{volume\ available\ for\ flow}{total\ wetted\ surface} \\
&= \frac{V_{voids}/V_{total}}{S_{total}/V_{total}} && (5.1.17)\\
&= \frac{\epsilon}{NS_p/\left(NV_p/(1-\epsilon)\right)} && (5.1.18)\\
&= \frac{\epsilon V_p}{(1-\epsilon)S_p}, && (5.1.19)
\end{aligned}
$$

as given by Nemec [18]. In equation (5.1.19) V_p denotes the particle volume and S_p denotes the particle surface area. To compensate for the stagnant region inside of the rings that exist in packed beds made up out of Raschig rings, the hydraulic radius must be recalculated. In Figure 5.2 some parameters that will be used in the following derivation are graphically defined. The use of these parameters results in an adapted Ergun equation valid only for flow through rings and can thus not be used as a general case for determining the Ergun constants. Using equation (5.1.16), the hydraulic radius for a ring-bed is given as:

$$
\begin{aligned}
r_h &= \frac{cross\ section\ available\ for\ flow}{wetted\ perimeter} && (5.1.20)\\
&= \frac{volume\ available\ for\ flow}{total\ wetted\ surface} && (5.1.21)\\
&= \frac{V_{total} - \sum_1^N V_{fc} + m\sum_1^N V_i}{\sum_1^N S_{fc} + m\sum_1^N S_i} && (5.1.22)\\
&= \frac{\epsilon_{fc} + m\epsilon_i}{(N/V_{total})\left(S_{fc} + mS_i\right)}, && (5.1.23)
\end{aligned}
$$

where ϵ_{fc} is the porosity of a packed bed if it were made of hypothetical solid cylinders with the same outer dimensions as the rings [18]. In equation (5.1.22) the inner volume and

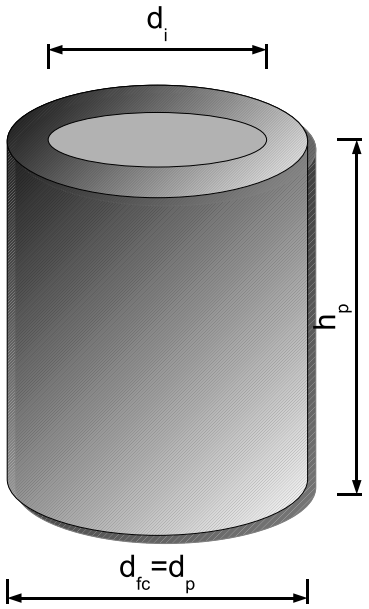

Figure 5.2: Graphical representation of a ring used in the derivation of the corrected Ergun constants for flow through a packed bed consisting of rings [18].

surface area of a ring is represented by V_i and S_i respectively. The volume and surface area of a hypothetical solid cylinders is denoted by V_{fc} and S_{fc} respectively. Sonntag's correction [18] is denoted by m in equations (5.1.22) and (5.1.23). The hypothetical porosity, ϵ_{fc}, is thus given by the following equation:

$$\epsilon_{fc} = \frac{V_{total} - NV_{fc}}{V_{total}} \tag{5.1.24}$$

$$= 1 - (1-\epsilon)\frac{V_{fc}}{V_p}. \tag{5.1.25}$$

In equation (5.1.23) the parameter ϵ_i represents the fraction of the total volume that is occupied by the inner volume of all the rings and can be expressed as:

$$\epsilon_i = \frac{NV_i}{V_{total}} \tag{5.1.26}$$

$$= (1-\epsilon)\frac{V_i}{V_p}. \tag{5.1.27}$$

If equations (5.1.24) and (5.1.26) are substituted into equation (5.1.20) the corrected hydraulic radius can be expressed as:

$$r_h = \frac{V_p - (1-\epsilon)(V_{fc} - mV_i)}{(1-\epsilon)(S_{fc} + mS_i)}. \tag{5.1.28}$$

Nemec described the magnitude of the superficial velocity as:

$$q = \frac{v\epsilon}{\chi}, \tag{5.1.29}$$

with χ the tortuousity. The actual path travelled by the fluid through a porous medium is also not equal to L. In some cases it has been postulated that the path can be up to twice the height of the bed [18]. Thus the effective path the fluid takes through the porous medium can be defined as:

$$L_e = L\chi. \tag{5.1.30}$$

If Sonntag's correction [20] is employed the superficial velocity is also influenced and equation (5.1.29) becomes:

$$v = \frac{q}{\epsilon_{fc} + m\epsilon_i}\chi. \tag{5.1.31}$$

To account for frictional losses through the porous medium the interstitial velocity is determined by adapting the Hagen-Poiseuille law. This law gives an expression for the average velocity in a tube. Using the hydraulic radius, r_h, and the tortuous path length, L_e, in the Hagen-Poiseuille law, an expression for the interstitial velocity in a porous medium is given as follows:

$$v = \frac{\Delta P r_h^2}{2\mu L_e}. \tag{5.1.32}$$

Substituting the hydraulic radius (equation (5.1.28)) and the adapted interstitial velocity (equation (5.1.31)) into the expression for laminar flow through porous media (equation (5.1.32)) yields:

$$\frac{\Delta p}{L} = 72\chi^2 \frac{\mu q}{d_e^2} \frac{(1-\epsilon)^2}{\epsilon^3} \left[\frac{\epsilon^3}{\left(1-(1-\epsilon)(V_{fc} - mV_i/V_p)\right)^3} \right] \times \left[\frac{(S_{fc} + mS_i)}{V_p} \frac{d_e}{6} \right]. \tag{5.1.33}$$

Whilst the fluid is flowing through the porous medium, energy is lost due to contractions, expansions and general flow effects coupled with flow through the medium. Inertial effects are normally associated with high Reynolds numbers but can also have and effect even in fluid flow with relatively low superficial velocities.

The force associated with the kinetic behavior of the fluid has the same direction as the superficial velocity. According to Nemec [18] this force can be expressed as the product of the characteristic area, S, characteristic kinetic energy per volume, K, and the dimensionless friction factor denoted by f. The previous relationship is given as:

$$F_k = SKf. \tag{5.1.34}$$

For flow in a tube, equation (5.1.34) can be expressed in terms of the wetted surface area, $2\pi RL_e$, and the kinetic energy, $\frac{1}{2}\rho v^2$. Thus for flow in a tube with radius R the kinetic force can be given as follows:

$$F_k = (2\pi RL_e)\left(\frac{1}{2}\rho v^2\right) f. \tag{5.1.35}$$

Again, inserting the hydraulic radius (equation (5.1.28)) and the adapted interstitial velocity (equation (5.1.31)) into equation (5.1.35) the following is obtained:

$$\frac{\Delta p}{L} = 3f\chi^3 \frac{\rho q^2}{d_e} \frac{(1-\epsilon)}{\epsilon^3} \left[\frac{\epsilon^3}{\left(1-(1-\epsilon)(V_{fc} - mV_i/V_p)\right)^3} \right] \times \left[\frac{(S_{fc} + mS_i)}{V_p} \frac{d_e}{6} \right]^2. \tag{5.1.36}$$

The well known Ergun equation is given in the following form by Nemec [18]:

$$\frac{\Delta p}{L} = A\frac{\mu q}{d_e^2}\frac{(1-\epsilon)^2}{\epsilon^3} + B\frac{\rho q^2}{d_e}\frac{(1-\epsilon)}{\epsilon^3}. \tag{5.1.37}$$

In Nemec's work [18], the experimentally determined values for the tortuousity, χ, and the friction factor, f, are kept the same as stated by Ergun. The reasoning is that when Sonntag derived his 20% criterion he used the original Ergun equation. Thus if adapted values for the tortuousity, χ, and the friction factor, f, are used, say for a bed consisting of equivalent solid cylinders, the value of Sonntag's correction would change. Finally from equations (5.1.33), (5.1.36) and (5.1.37), the corrected Ergun constants are given as:

$$\begin{aligned} A &= 150\left[\frac{\epsilon^3}{\left(1-(1-\epsilon)\left(V_{fc}-mV_i\right)/V_p\right)^3}\right] \\ &\quad\times\left[\frac{d_e\left(S_{fc}+mS_i\right)}{6V_p}\right] \end{aligned} \tag{5.1.38}$$

and

$$\begin{aligned} B &= 1.75\left[\frac{\epsilon^3}{\left(1-(1-\epsilon)\left(V_{fc}-mV_i\right)/V_p\right)^3}\right] \\ &\quad\times\left[\frac{d_e\left(S_{fc}+mS_i\right)}{6V_p}\right]^2, \end{aligned} \tag{5.1.39}$$

respectively, with V_i the volume of the inner void cylinder, V_p the particle volume and V_{fc} the volume of a hypothetical full cylinder with the same outer dimensions. In equations (5.1.38) and (5.1.39) the surfaces are represented with an S and the subscripts have the same meaning as previously mentioned volumes. The fraction of the inner void of each ring available for flow is denoted by m and can be taken as 20% according to Sonntag [20]. The equivalent particle diameter is defined as $6V_p/S_p$ and is denoted by d_e in equations (5.1.38) and (5.1.39). Parameters for these equations, for the particular Raschig rings used in this work, are given in Table 5.4. To assess Nemec's model data from the Raschig rings used in

Packing material	Material	V_i (m^3)	V_{fc} (m^3)	V_p (m^3)
Raschig rings	Glass	1.76×10^{-7}	3.46×10^{-7}	1.70×10^{-7}
Raschig rings	Metal	6.36×10^{-7}	7.85×10^{-7}	1.49×10^{-7}
		S_i (m^2)	S_{fc} (m^2)	S_p (m^2)
Raschig rings	Glass	1.41×10^{-4}	2.74×10^{-4}	3.70×10^{-4}
Raschig rings	Metal	2.82×10^{-4}	4.71×10^{-4}	6.20×10^{-4}

Table 5.4: Parameters of the different packing structures used in the experiments.

the present study was employed.

5.1.2.3 Assessment

To test the accuracy of the model presented by Nemec [19], it was used in conjunction with parameters from the experiments conducted at the TUC in Norway. It was calculated that there were 4737 glass Raschig rings used in the $0.00275m^3$ packed bed. The specific surface, a, and porosity of the packing were calculated to be 637.34 (m^2/m^3) and 0.71 respectively. The results obtained for the metallic Raschig rings is provided in Appendix C. When Sonntag's [20] correction for the stagnant regions within a particle is employed, the effective porosity drops to 0.46 and thus the resulting specific surface decreases to 454.5 (m^2/m^3). To test the validity of Nemec's equation it is represented in Figures 5.7- 5.16 alongside the Ergun equation [8] and the granular- [7] and foam RUC models [4].

In assessing the Ergun equation and the RUC model there exist parameters that are not yet clearly defined. They are the numerical value for the drag factor, c_d, and Sonntag's correction, m. Although Sonntag found that only 20% of the interior of a ring is available for flow, other percentages were also investigated as a means of verification.

The effect of the shape factors was investigated and the results are given in Figures 5.3 and 5.4. The Sonntag fraction, m, is kept at the suggested 20% and the drag factor, c_d, is kept equal to 1. For the granular RUC the volume of the bed was divided into N volumes and a particle diameter, d_s, was calculated according to model [7]. For the foam models the diameter, d, of a RUC volume was used as defined by the RUC foam model [4]. For the Ergun equation, the accompanying nominal diameter, D_p, was used. It is clear that, to a large extent, the sphericity factor can compensate for the higher drag existing in the bed.

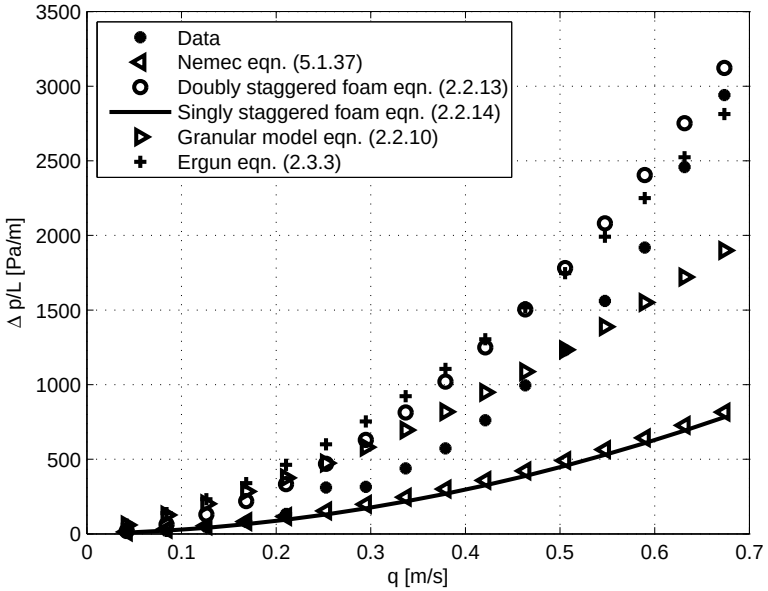

(a)

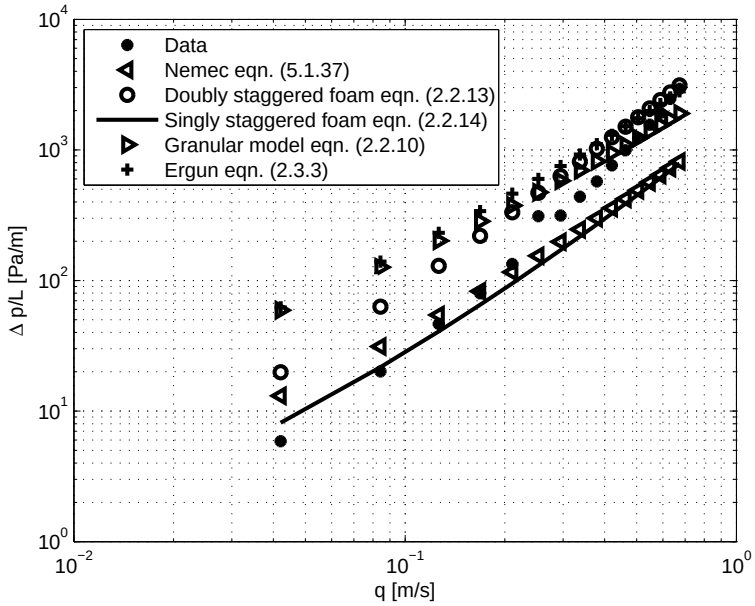

(b)

Figure 5.3: (a) Investigation of the effect of the sphericity on the Ergun equation and the granular RUC model. (b) The same comparison but on a log-log axis.

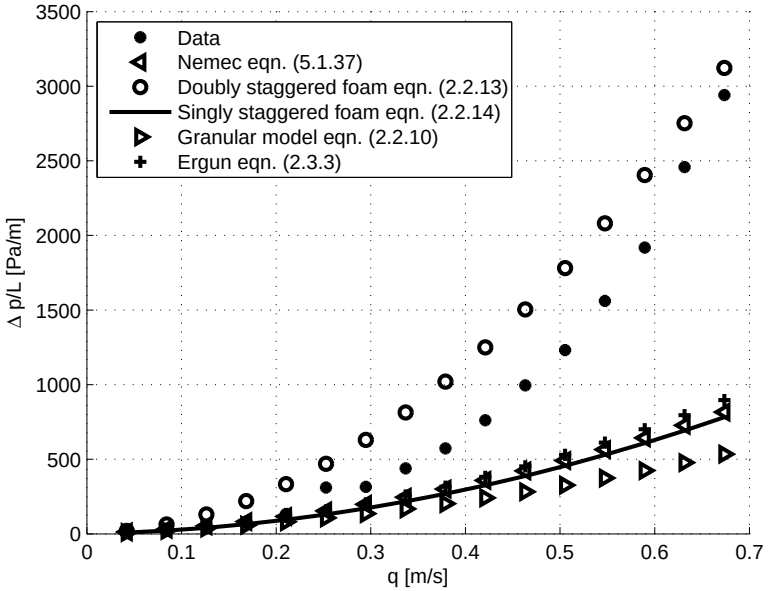

(a)

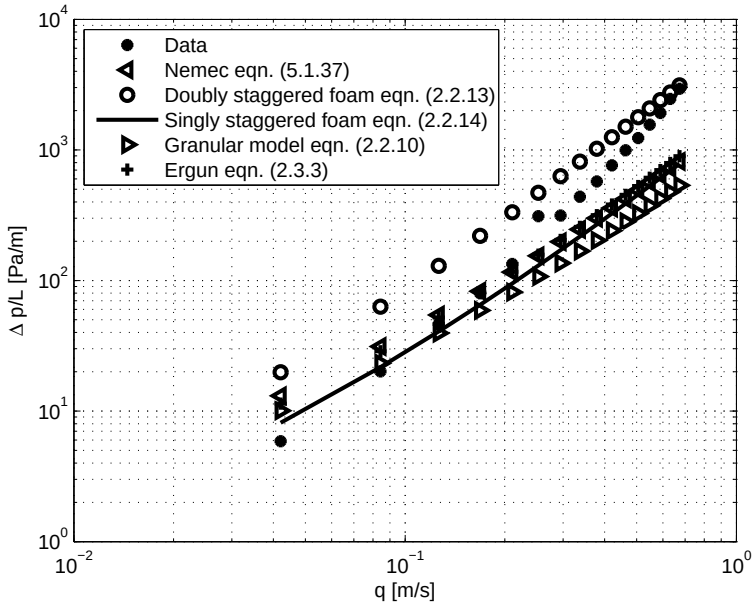

(b)

Figure 5.4: (a) Investigation of the effect of a sphericity equal to one on the Ergun equation and granular RUC model. (b) The same comparison but on a log-log axis.

To further assess the effect of the shape factor, the nominally defined shape factor was compared to the newly defined cubic shape factor, as described in Section 3.1.4 and 3.1.5 respectively. It is clear from Figure 5.5 that the commonly used shape factor seems to perform better than the cubic shape factor. It is not trivial to decide which shape factor performs the best given that all the models describe a different curvature than the data. Thus the commonly used shape factor will be used in the rest of this work to keep the results in accordance with theory used in industry. The same result can be deduced for the Ergun equation. This

is deduced since the Sonntag correction was taken to be equal to 20% thus implying that the porosity will be equal to 0.46 (refer to Table 5.5). In the region of porosities between 0.35 and 0.55 the Ergun equation, granular RUC model and the Ergun equation with the McDonald correction [17], predict approximately the same values for the Ergun constants, A and B [7]. Thus the shape factor will have approximately the same effect on the Ergun equation [8] as it did on the granular RUC model [7] in Figure 5.5.

The Ergun equation's constants were determined through experiments on packed beds consisting of uniform spherical particles and the geometrical limitation of such a packing implies a porosity range of $0.35 < \epsilon < 0.55$ [7]. It thus follows trivially that the Ergun equation is not applicable for beds with a porosity outside this range.

The granular RUC model's constants however, are derived from physical reasoning and take into account a changing porosity. Beds with a porosity from 0 through 1 can be modelled with the granular RUC model and the Ergun constants, A and B, will change with the variance in porosities [7]. This characteristic is shown in Figure 5.6 with a drag factor, c_d, equal to 1.9 as proposed by du Plessis [7]. The RUC model thus shows more flexibility regarding packings encountered in industry.

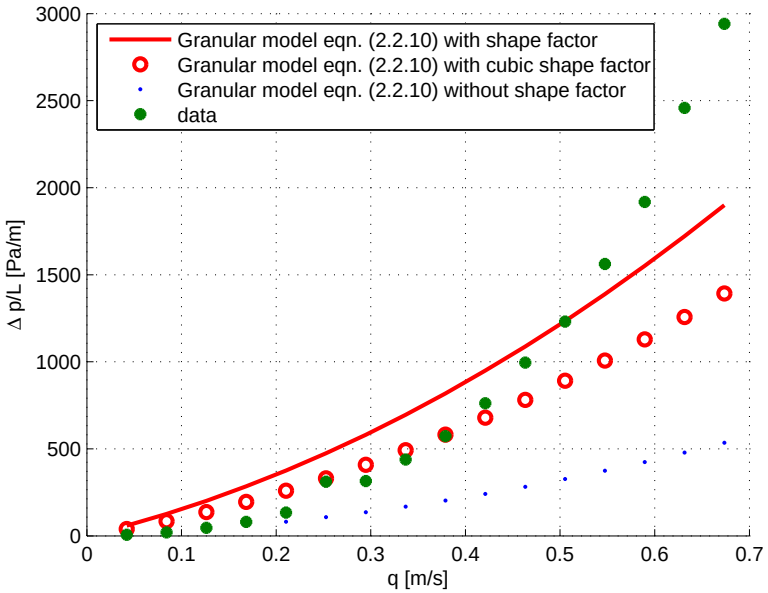

(a)

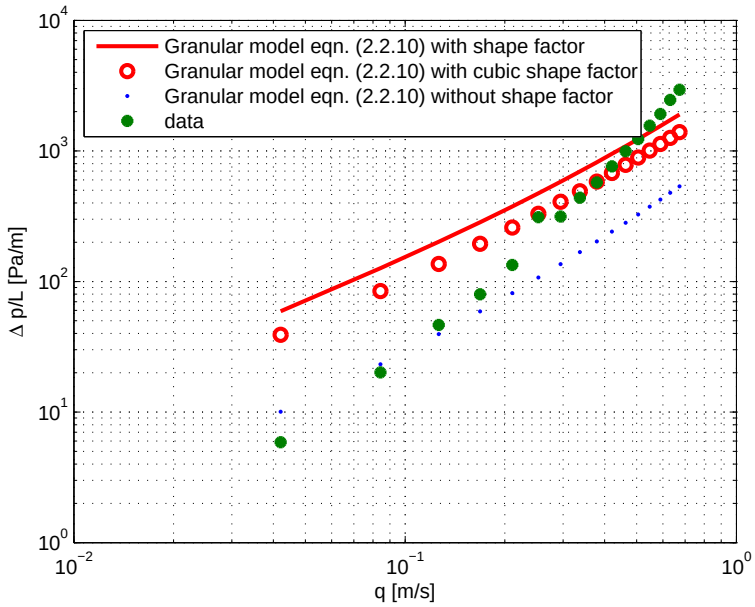

(b)

Figure 5.5: (a) Comparison of different shape factors, (b) comparison of different shape factor on a log-log axis.

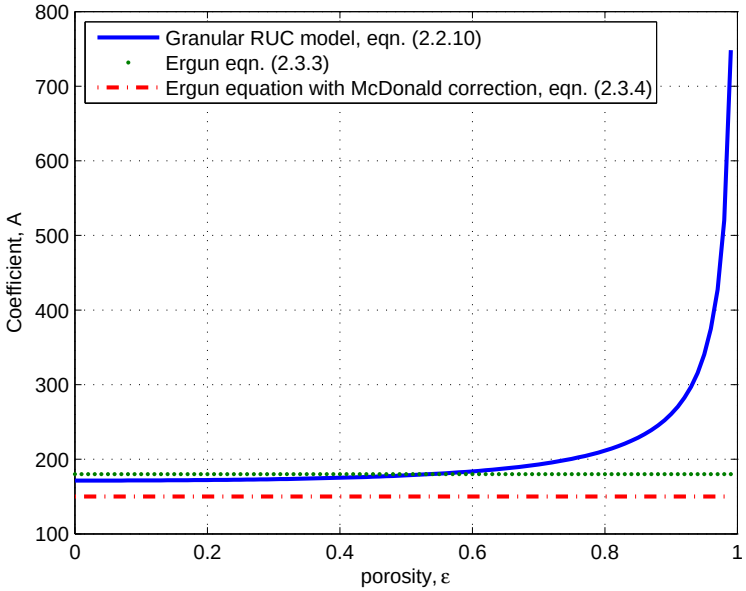

(a)

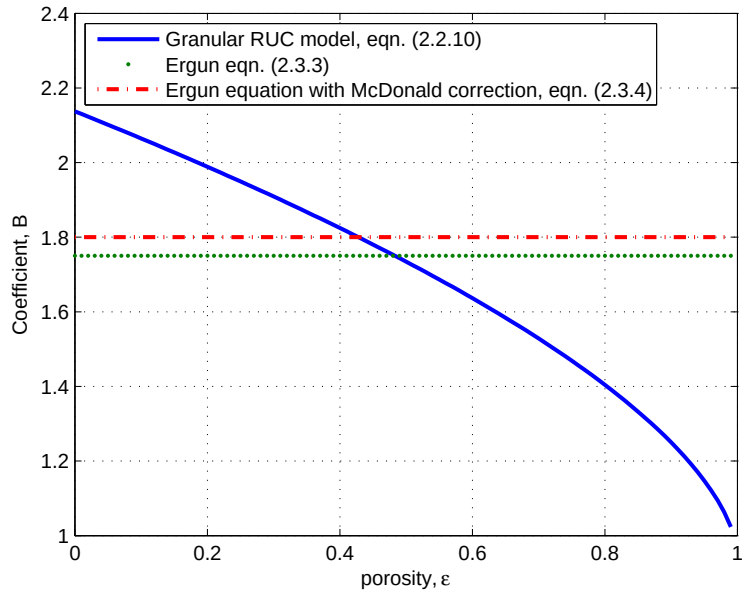

(b)

Figure 5.6: (a) Comparison of the A coefficients and (b) comparison of the B coefficients of the Ergun equation as given by du Plessis [7].

The next parameter to be investigated is the percentage of the volume inside of the ring available for flow (Sonntag's correction, m). To be able to assess the effect of the changing porosity and specific surface on all of the investigated models, the porosity and specific surface associated with each value of *m* are tabulated in Table 5.5.

m	a $[m^2/m^3]$	ϵ [-]
0.1	430.38	**0.43**
0.2	454.73	**0.46**
0.3	479.07	**0.49**
0.4	503.41	**0.52**
0.5	527.75	**0.55**
0.6	552.10	0.58
0.7	576.44	0.61
0.8	600.78	0.64
0.9	625.13	0.67
1	649.47	0.70

Table 5.5: Parameters associated with the different percentages of the volume available for flow inside of the ring.

Figures 5.7 to 5.16 show the influence of the Sonntag correction. The form drag factor, c_d, was kept equal to one. It is clear that the models' best correlation to the data occurs at 20 and 30 percent. Thus the results presented in Figures 5.7 to 5.16 agree with Sonntag's findings.

The packed beds under which Nemec's equation has been verified, was for porosities in the range of $0.37 < \epsilon < 0.52$. The bed formed in this work had a porosity of 0.71 before Sonntag's correction. The deviation of Nemec's model from the data, when the porosity is outside of the before mentioned range, may thus be attributed to the porosity. Only after Sonntag's correction do the porosities comply with the bed porosities tested by Nemec. So after Sonntag's correction Nemec's effective bed porosities would have been even lower than the previously mentioned porosity range. Thus when working with too high or too low porosities, the result may be expected to deviate from the data. In Table 5.5 the acceptable porosities are indicated with bold print.

The Ergun equation with its unchanging porosities will be inaccurate for all porosities associated with a Sonntag correction greater that 50%. The RUC model however takes into account the influence of the higher porosity as mentioned earlier (refer to Figure 5.6).

At a superficial velocity of $0.25 m/s$ a data point is found that does not follow the same trend as the rest of the data. It can be assumed that that particular data point is associated with an experimental error and should be overlooked. This data point is indicated in Figure 5.7.

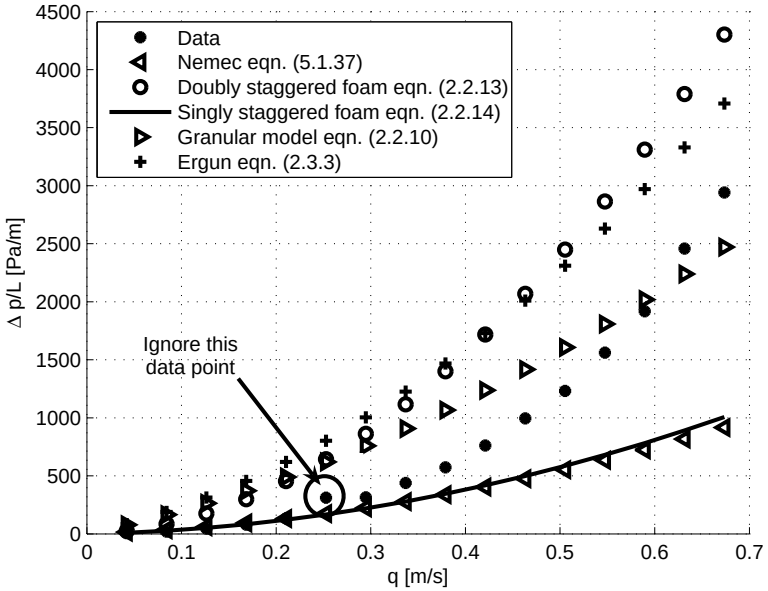

(a)

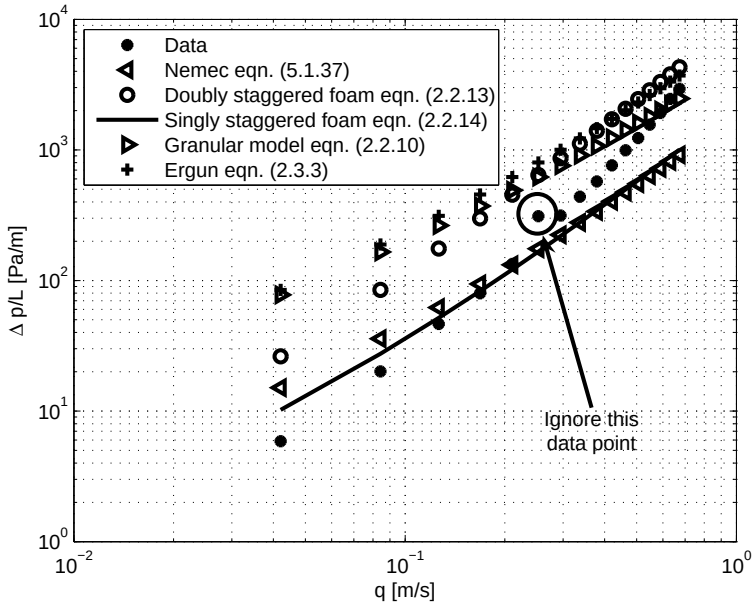

(b)

Figure 5.7: (a) Comparison of models with the Sonntag correction equal to 10%. (b) Pressure gradients from the different models and the data.

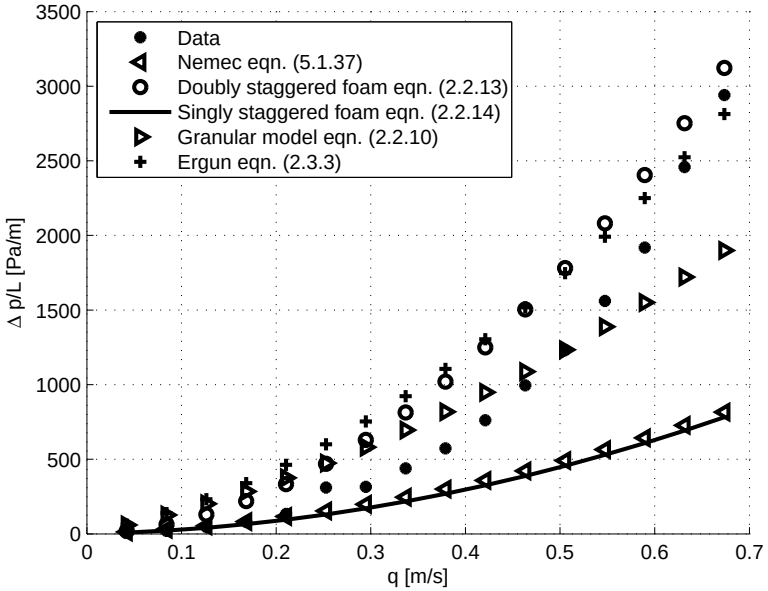

(a)

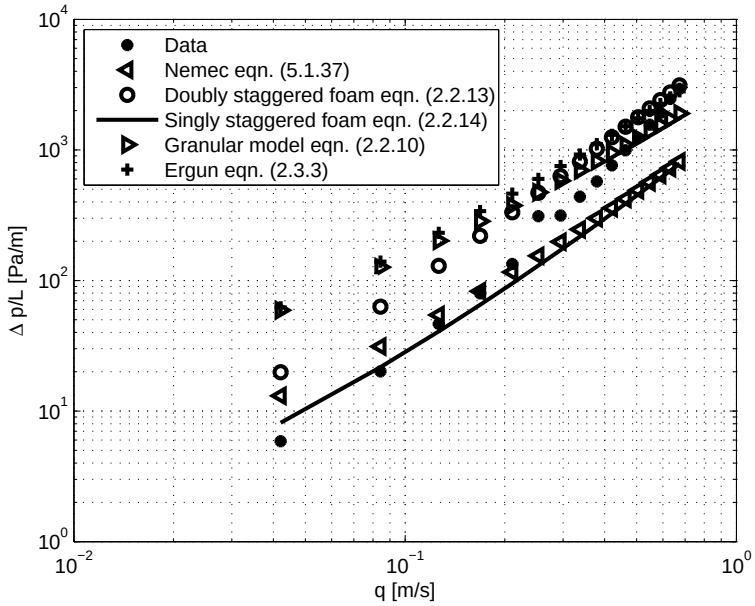

(b)

Figure 5.8: (a) Comparison of models with the Sonntag correction equal to 20%. (b) Pressure gradients from the different models and the data.

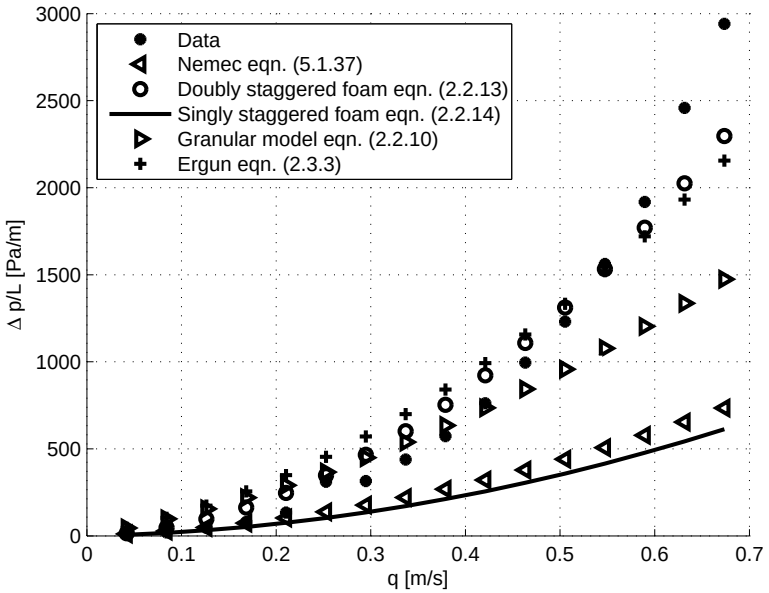

(a)

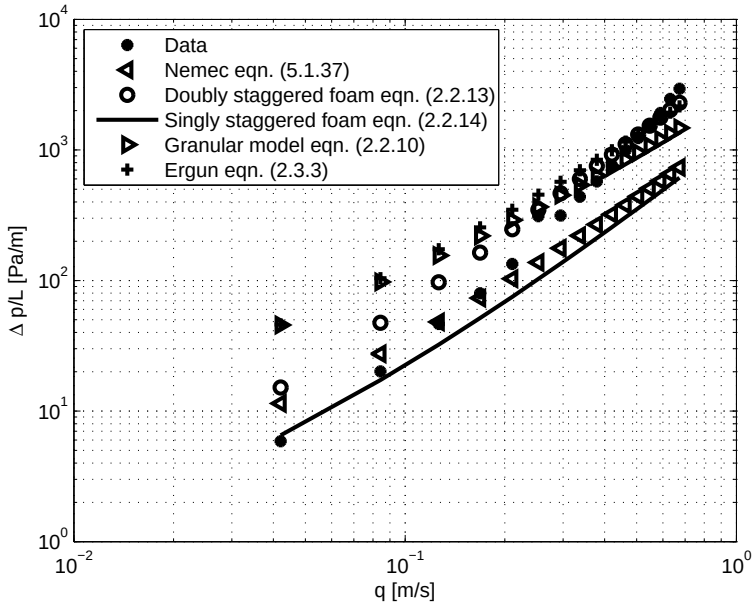

(b)

Figure 5.9: (a) Comparison of models with the Sonntag correction equal to 30%. (b) Pressure gradients from the different models and the data.

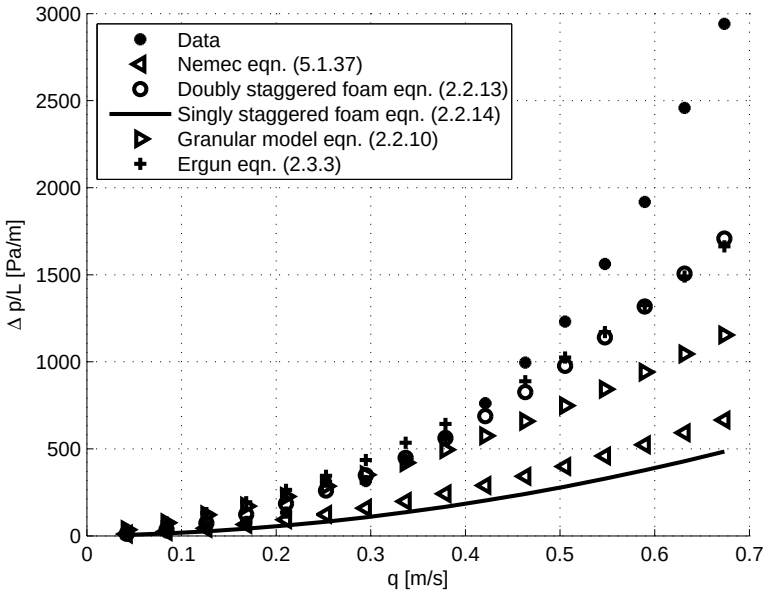

(a)

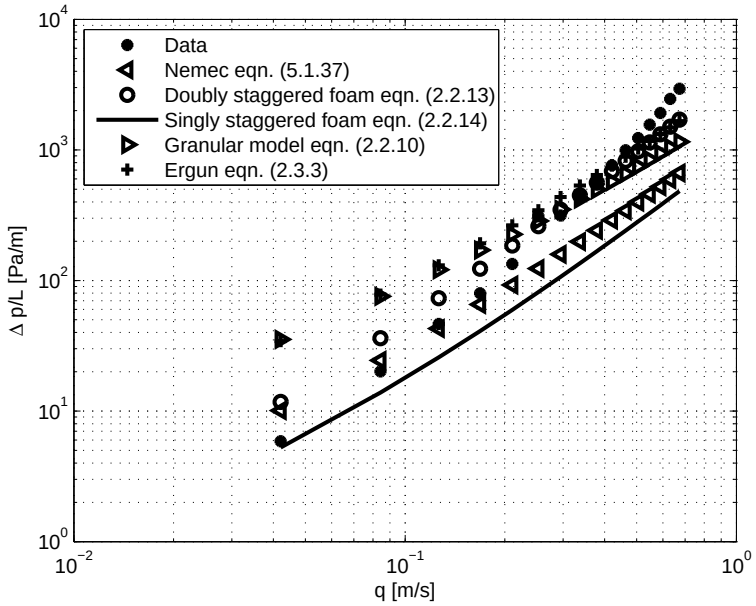

(b)

Figure 5.10: (a) Comparison of models with the Sonntag correction equal to 40%. (b) Pressure gradients from the different models and the data.

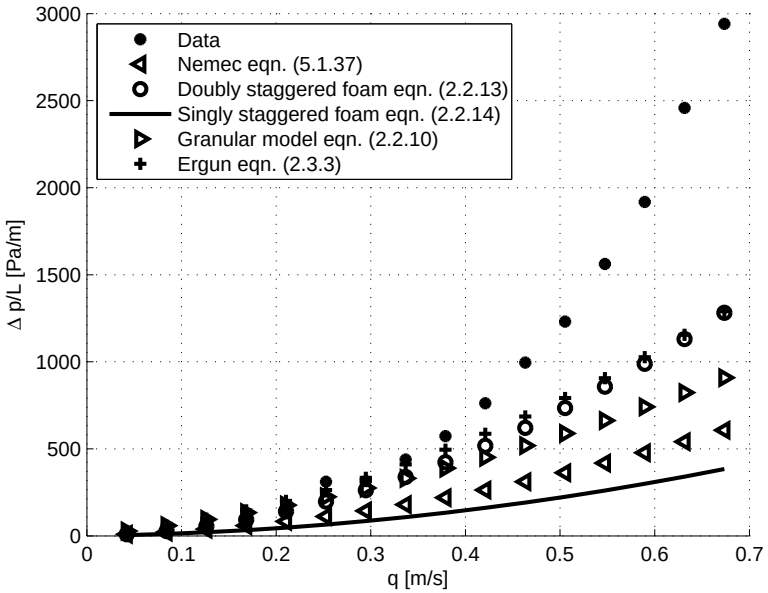

(a)

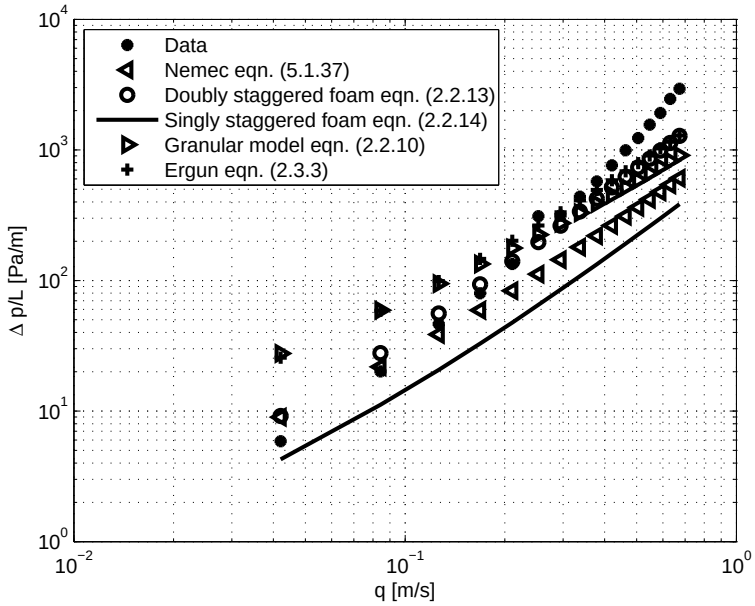

(b)

Figure 5.11: (a) Comparison of models with the Sonntag correction equal to 50%. (b) Pressure gradients from the different models and the data.

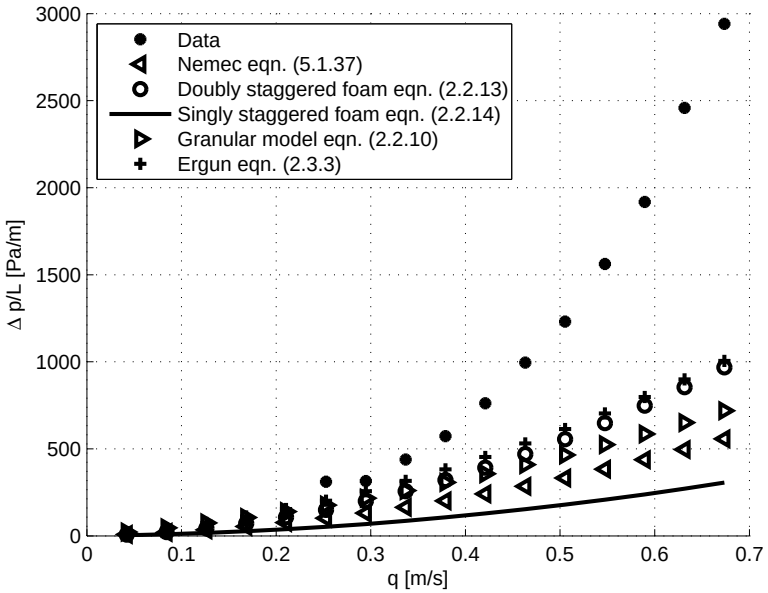

(a)

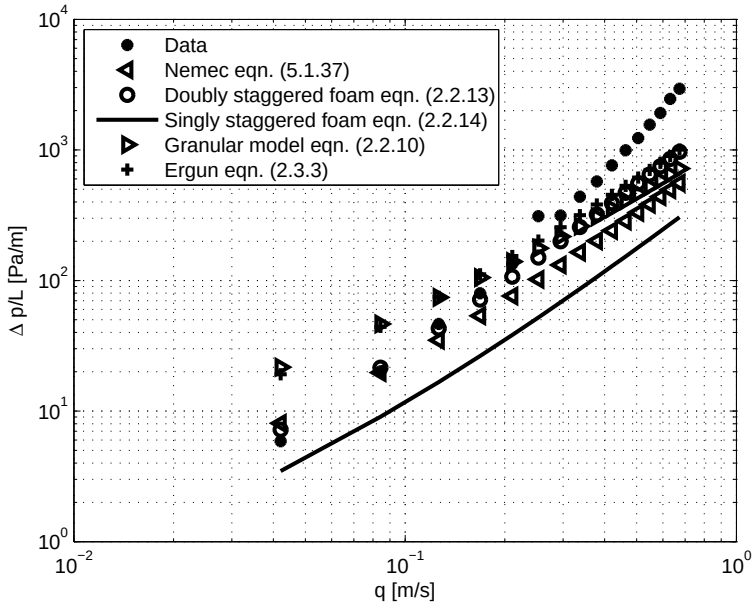

(b)

Figure 5.12: (a) Comparison of models with the Sonntag correction equal to 60%. (b) Pressure gradients from the different models and the data.

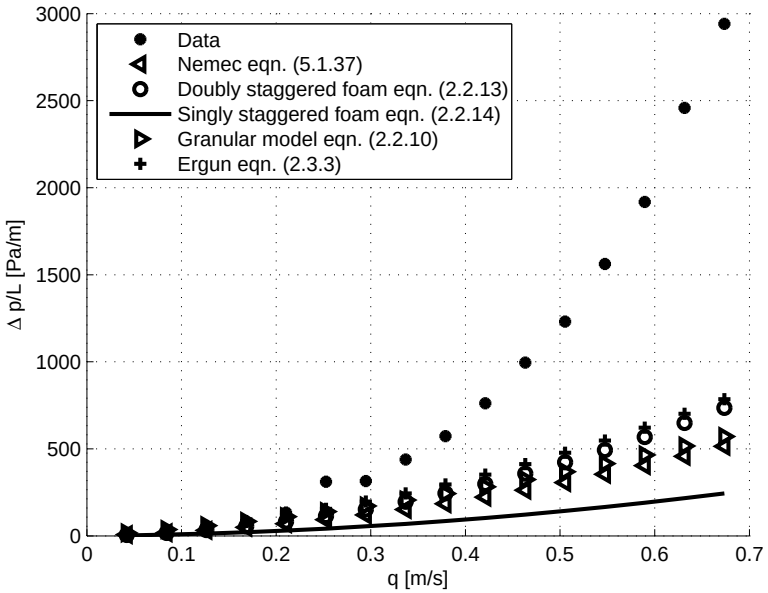

(a)

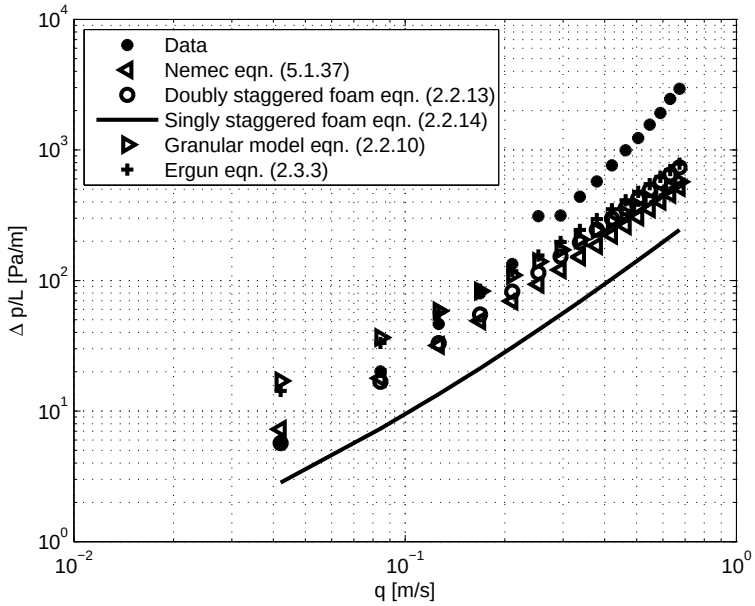

(b)

Figure 5.13: (a) Comparison of models with the Sonntag correction equal to 70%. (b) Pressure gradients from the different models and the data.

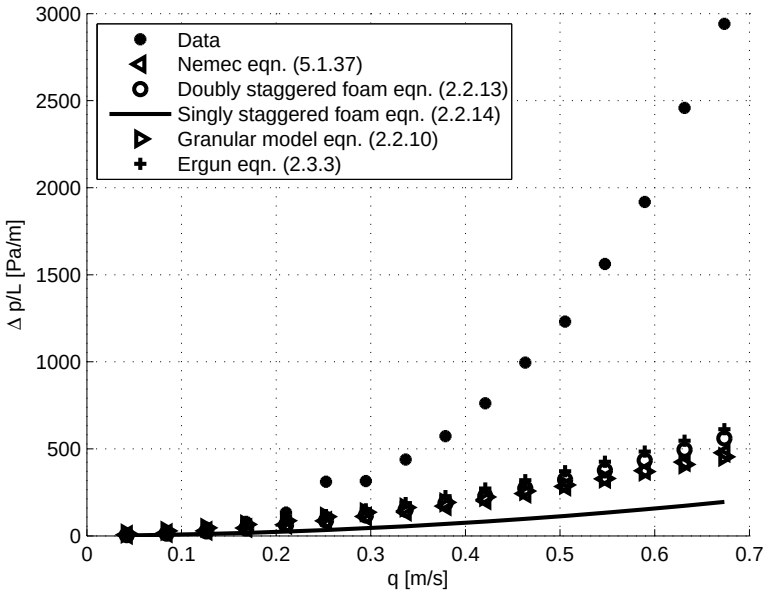

(a)

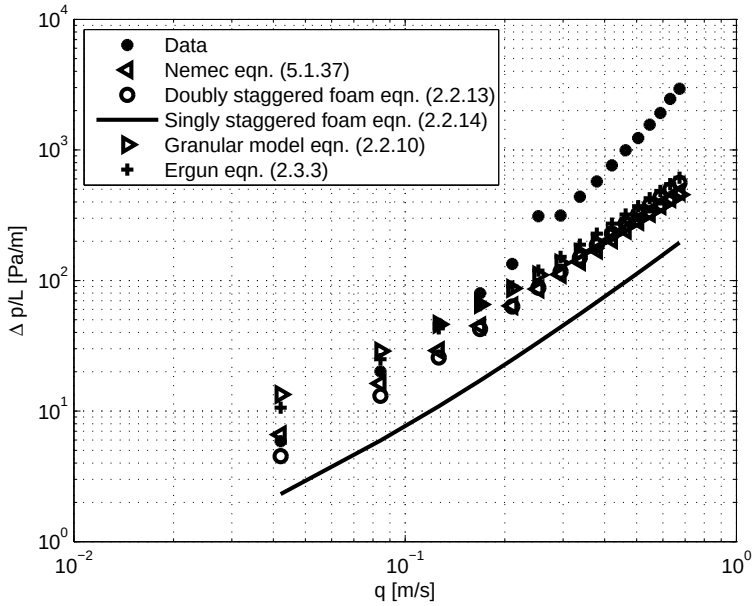

(b)

Figure 5.14: (a) Comparison of models with the Sonntag correction equal to 80%. (b) Pressure gradients from the different models and the data.

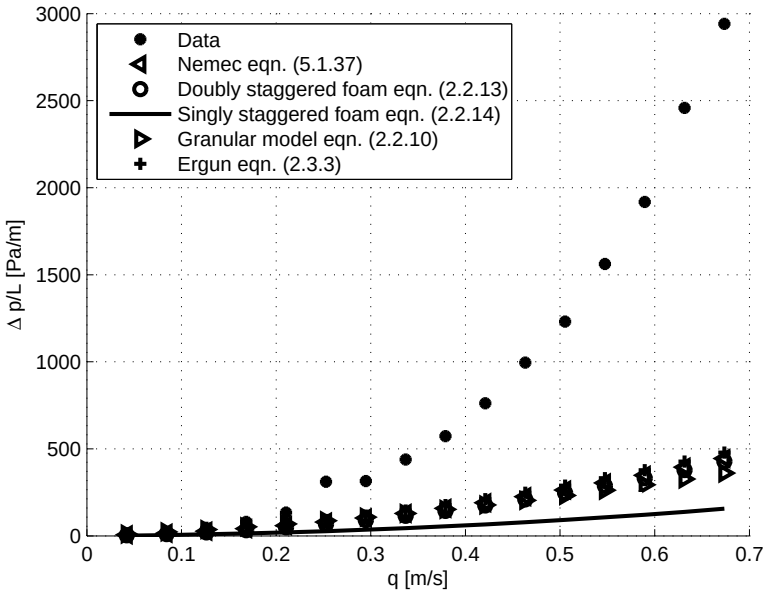

(a)

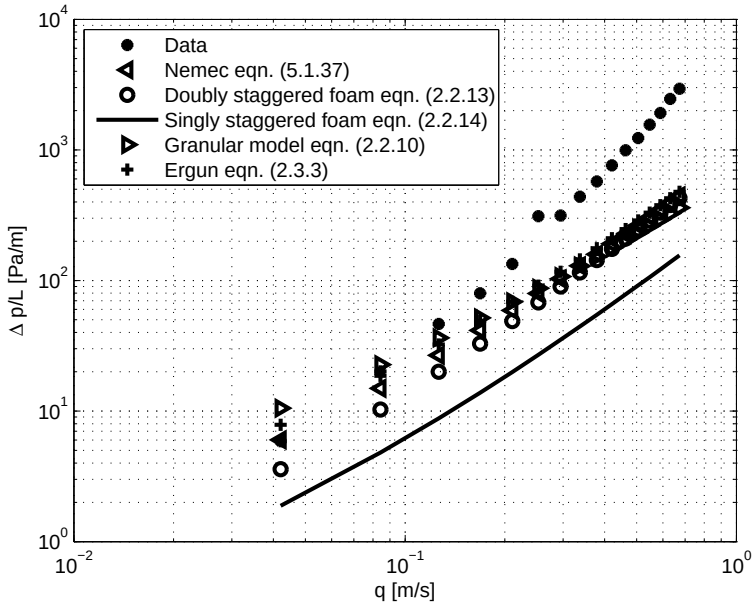

(b)

Figure 5.15: (a) Comparison of models with the Sonntag correction equal to 90%. (b) Pressure gradients from the different models and the data.

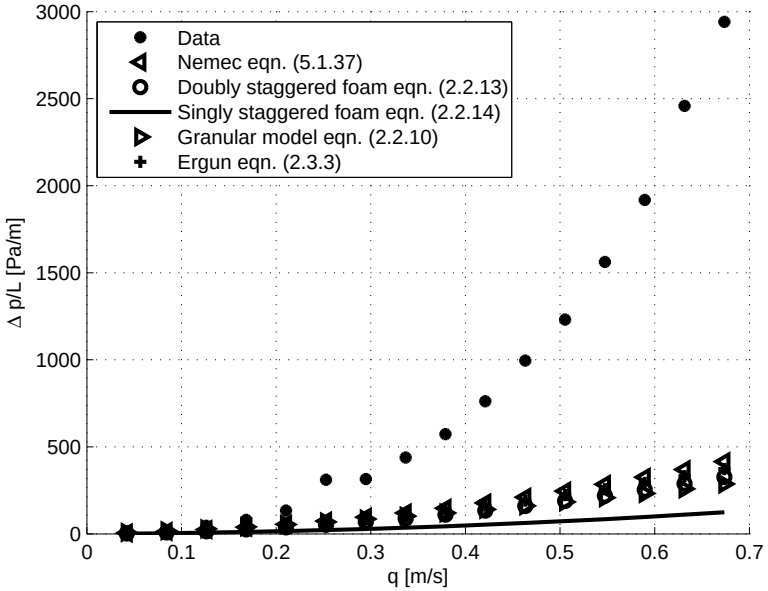

(a)

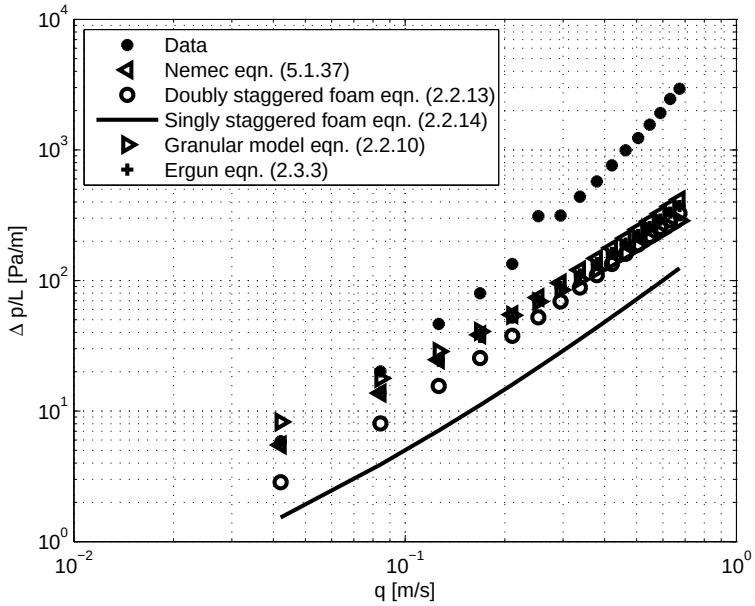

(b)

Figure 5.16: (a) Comparison of models with the Sonntag correction equal to 100%. (b) Pressure gradients from the different models and the data.

Figures 5.17 to 5.20 show the effect of the form drag factor, c_d. In Figure 5.17 the Sonntag correction was kept at 20% and the form drag factor was increased to 2. The effect is an over prediction of the pressure drop by the foam model but reasonably good results from the granular RUC model.

In Figure 5.18 the total inner volume of the ring was made available for flow and the drag factor kept at 2. The result was an under prediction of the pressure drop by both

the granular and the foam model. The result emphasizes the importance of the Sonntag's correction when working with rings.

In Figure 5.19 a form drag factor of 1.9 was used a suggested by du Plessis [7]. Results produced by the granular RUC model are in excellent agreement with those of the Ergun equation (2.3.3). With a drag factor equal to 1.5 the granular model [7] also gives a good approximation if no attention is given to the discrepancy in the curvature of the data and the models. To determine the correct value of c_d numerical analysis is reguired [7]. These results serve as a sensitivity analysis and cannot replace numerical analysis.

According to Nemec [19] there exists an annular wall zone where the porosity is greater than the porosity in the rest of the bed. This can lead to serious channelling effects. The reason for the increase in the porosity at the wall can be attributed to the particles whose arrangement have to conform to the shape of the tower at the wall. As the column to particle ratio was equal to approximately 10, for both Raschig rings, the viscous friction of the wall could not necessarily be neglected. The reason is that the influence of the wall friction increases as the particle to column ratio (d_c/d_p) decreases. The curvature difference noted between the respective models and the data may thus be caused by wall effects.

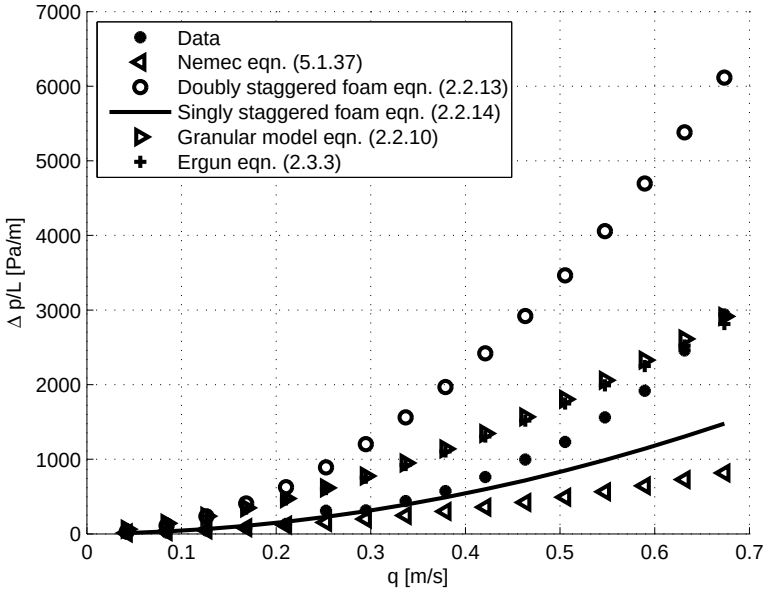

(a)

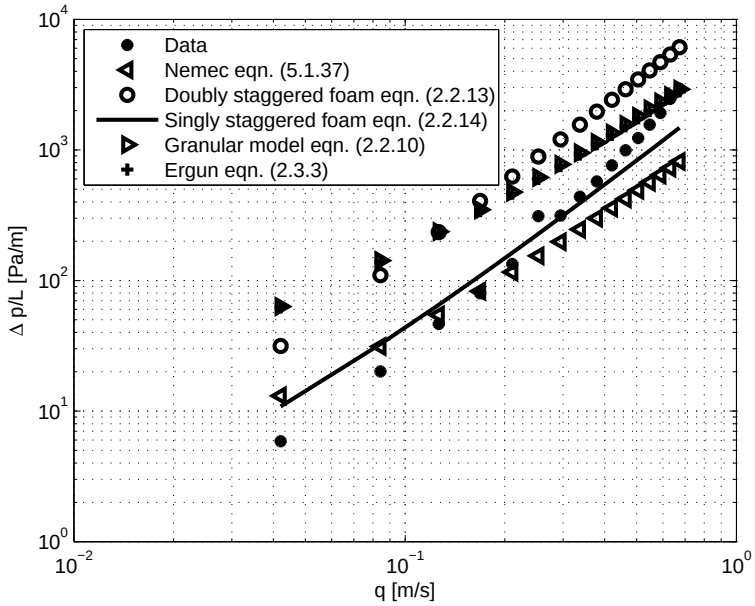

(b)

Figure 5.17: (a) Influence of the drag factor, c_d. The value for c_d was set equal to 2 in the present figure. (b) Pressure gradients of the different models and the data.

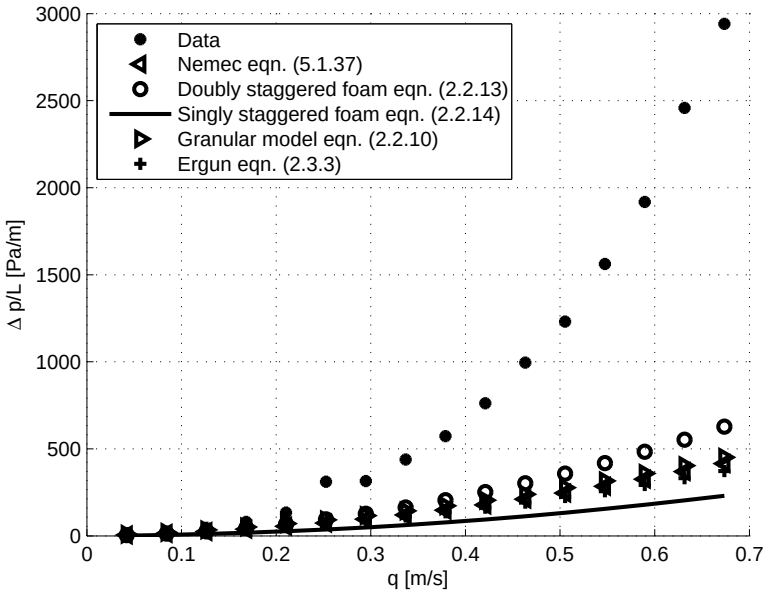

(a)

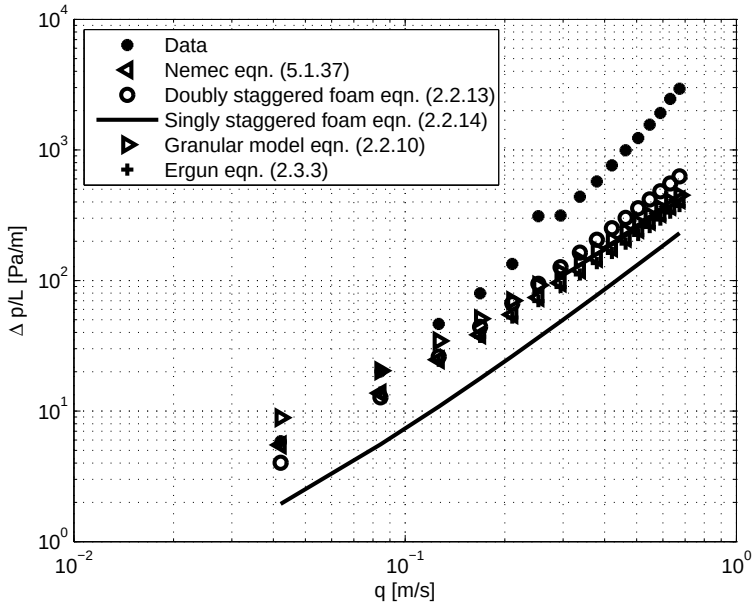

(b)

Figure 5.18: (a) Influence of the drag factor equal to 2 with the hole inner volume of the rings available for flow. (b) Pressure gradients of the different models and the data.

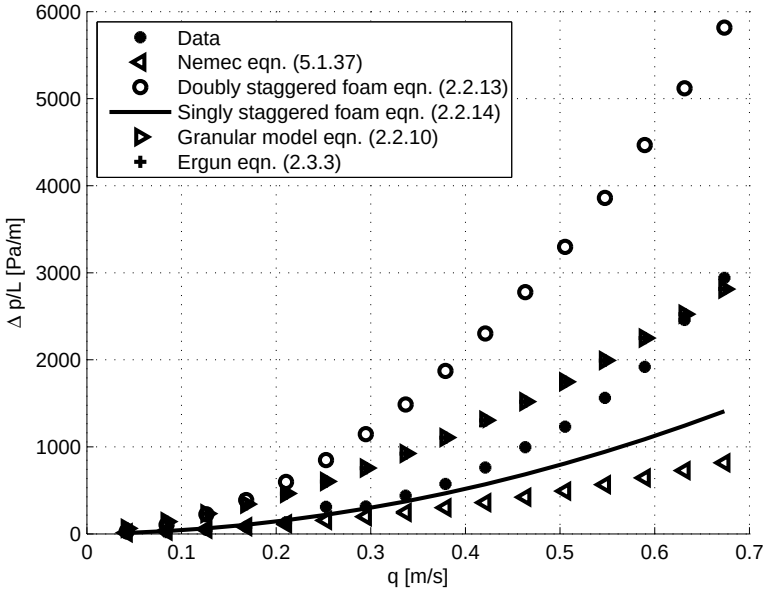

(a)

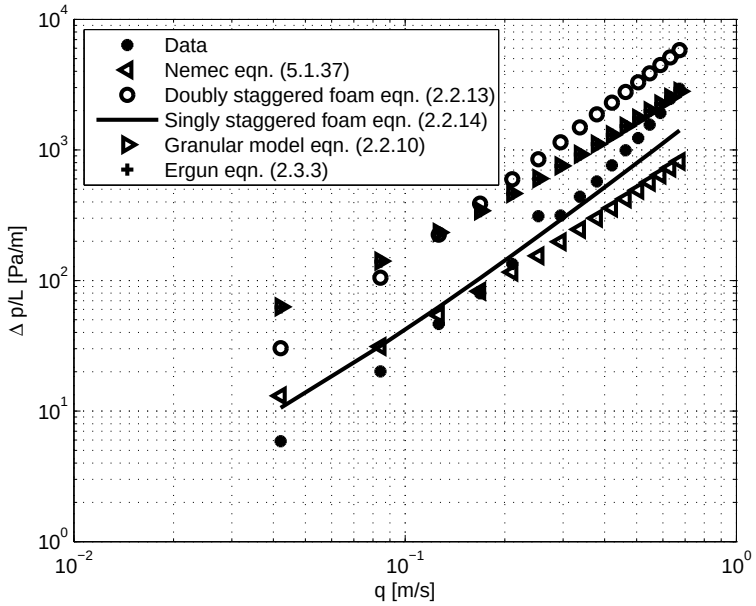

(b)

Figure 5.19: (a) Influence of the drag factor equal to 1.9 with the 20% of the inner volume of the rings available for flow. (b) Pressure gradients of the different models and the data.

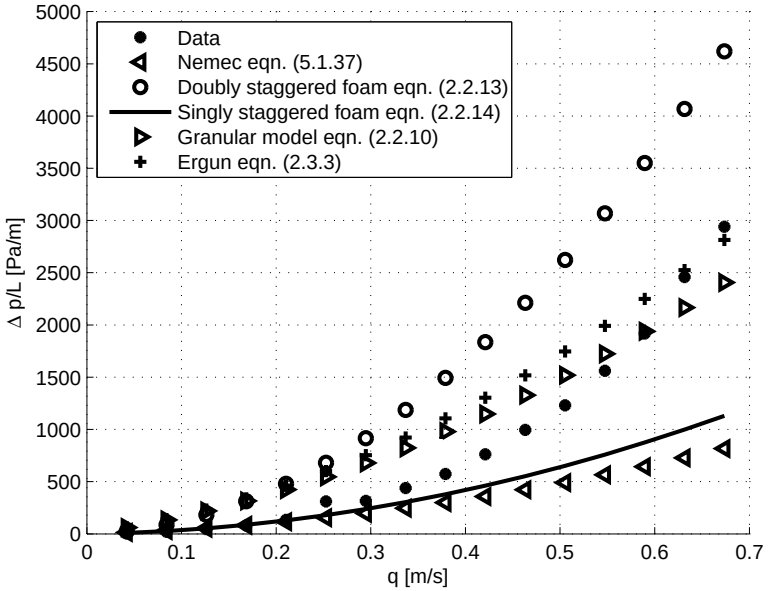

(a)

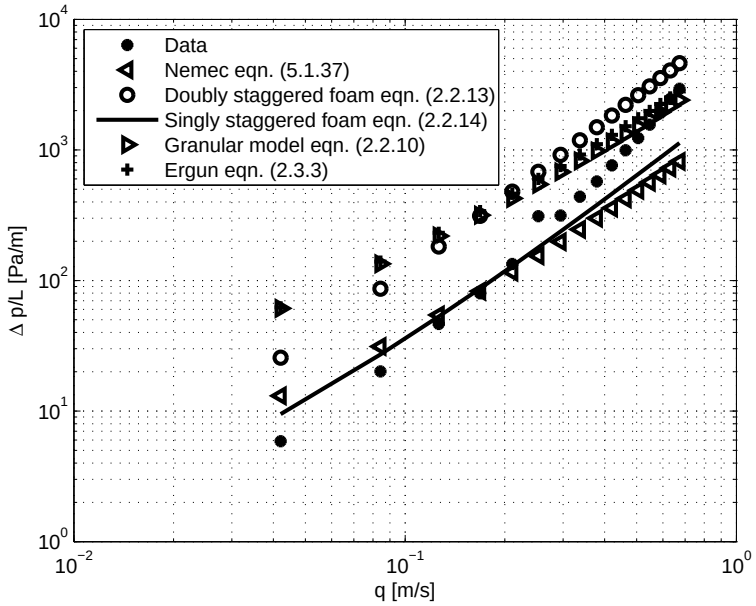

(b)

Figure 5.20: (a) Influence of the drag factor equal to 1.5 with the 20% of the inner volume of the rings available for flow. (b) Pressure gradients of the different models and the data.

5.1.3 Mackowiak's model for single phase flow through packed beds.

Mackowiak presented an extension of the channel model by introducing the concept of partially perforated walls.

5.1.3.1 Description and derivation of Mackowiak's equation

According to Mackowiak [15] the pressure drop in a channel with non-perforated walls and with a channel of length l can be expressed by:

$$\frac{\Delta p}{L} = \frac{\lambda F_v^2}{2 d_h \epsilon^2}, \tag{5.1.40}$$

with F_v the gas capacity factor and d_h the hydraulic diameter of the packing as described in equation (5.1.8). The resistance coefficient is represented by λ. A pressure drop through a porous medium is mainly caused by frictional forces at the fluid-solid interface. If the pressure drop associated with the tortuousity of the flow paths is assumed negligible against the pressure drop associated with the frictional drag, it can be said that the pressure drop is directly linked to the total surface area of the packing. Thus it follows that the pressure drop decreases in perforated packings as opposed to non-perforated packing due to the decrease in the frictional area. A perforated packing can therefore be represented by the channel model with a smaller effective area. It is illustrated in Figure 5.21. The form factor of the perforated wall φ [15] is trivially defined as the ratio of the total perforated surface area over the total surface area of the packing. This is given in equation (5.1.41) with A being the total area of a packing element and A_o the total perforated surface area of the particular packing element and is expressed as:

$$\varphi \equiv \frac{A_o}{A}. \tag{5.1.41}$$

The ratio of the pressure drop of the perforated to non-perforated packing would hence be the same as the ratio of the effective packing heights (refer to Figure 5.21). Due to the

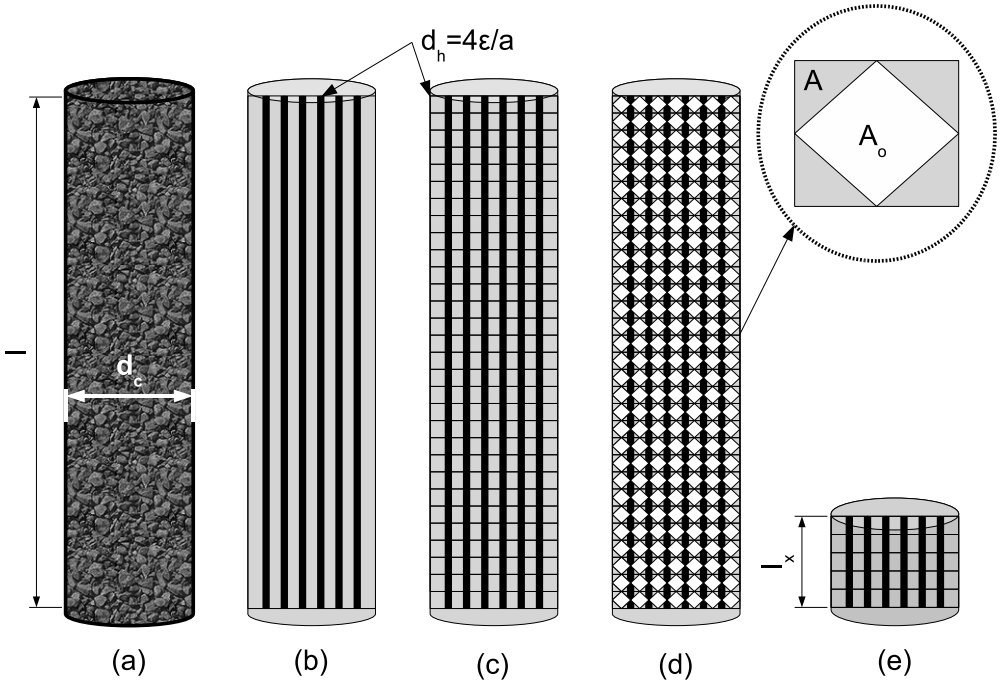

Figure 5.21: (a) Representation of a packed column, (b) representation of the channel model, (c) channel model divided into areas representing each packing element, (d) perforated packings in the channel model and (d) the effective channel model for perforated packings.

constant pressure gradient, an equation can be formulated from Figure 5.21 as follows:

$$\frac{\Delta p_{l_x}}{\Delta p_l} = \frac{l_x}{l}. \tag{5.1.42}$$

Equation (5.1.42) also relates to the proportion of non-perforated wall surface area in the packing, namely $1 - \varphi$, as follows:

$$\frac{l_x}{l} = 1 - \varphi. \tag{5.1.43}$$

Hence it can be deduced that:

$$\frac{\Delta p_{l_x}}{\Delta p_l} = 1 - \varphi. \tag{5.1.44}$$

Combining equation (5.1.12) and (5.1.44) the following equation can be formulated:

$$\frac{\Delta p}{L} = \psi_0(1 - \varphi)\left(\frac{1-\epsilon}{\epsilon^3}\right)\left(\frac{F_v^2}{d_p K}\right), \tag{5.1.45}$$

with ψ_0 the resistance coefficient for non-perforated packings like Raschig rings. The factor $(1 - \varphi)$ in equation (5.1.45) thus accounts for the decrease in the pressure drop due to perforation in packings for example Pall rings.

According to Mackowiak [15] the value for ψ_0 has been determined experimentally and has been found to be given by:

$$\psi_0 = \left(\frac{725.6}{Re_v} + 3.203\right), \tag{5.1.46}$$

with Re_v the modified Reynolds number and is defined as:

$$Re_v = \frac{q d_p}{(1-\epsilon)\mu} K, \tag{5.1.47}$$

by Mackowiak [15]. Substituting equation (5.1.46) into equation (5.1.45) the final result to predict pressure drop in perforated and non-perforated packings is given as:

$$\frac{\Delta p}{L} = \left(\frac{725.6}{Re_v} + 3.203\right)(1 - \varphi)\left(\frac{1-\epsilon}{\epsilon^3}\right)\left(\frac{F_v^2}{d_p K}\right). \tag{5.1.48}$$

It should be mentioned that in the case of non-perforated packings, like Raschig rings, the form factor, φ, would be equal to zero.

5.1.3.2 Assessment

To assess equation (5.1.48) it was compared to the data obtained at the TUC. It was assessed with the data obtained for glass Raschig rings as discussed in Chapter 4. As assumed in section 5.1.2 the nominally defined shape factor is used in the current section. The same packing data is used as in section 5.1.2 so the shape factors will exhibit the same behaviour. The form drag factor, c_d, is kept equal to unity during the assessment of the influence of Sonntag's correction on equation (5.1.48).

Figures 5.22 to 5.31 show the effect of Sonntag's correction. The value of the Sonntag's correction was varied from 10% to a 100%. Mackowiak's equation (5.1.48) compares well to all of the other models. Again, with the Sonntag correction equal to 20% the best fit is

obtained. When the total volume of the inner cylinder is available for flow and m set equal to 1, equation (5.1.48) performs better than all of the other models. It can be concluded that Mackowiak's equation with the Sonntag correction performs much better with than without the correction.

It must be kept in mind that Mackowiak's equation only applies to $Re_v \in (200, ..., 2000)$. The range of the adapted Reynolds numbers for the glass Raschig rings used is $Re_v \in (26, ..., 430)$. Thus it would be no surprise should equation (5.1.48) not predict the pressure drop accurately below $Re_v = 200$.

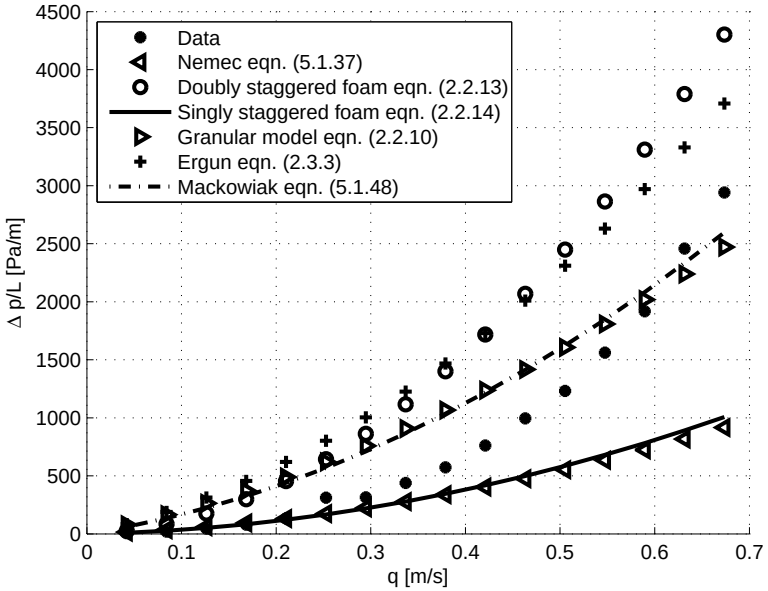

(a)

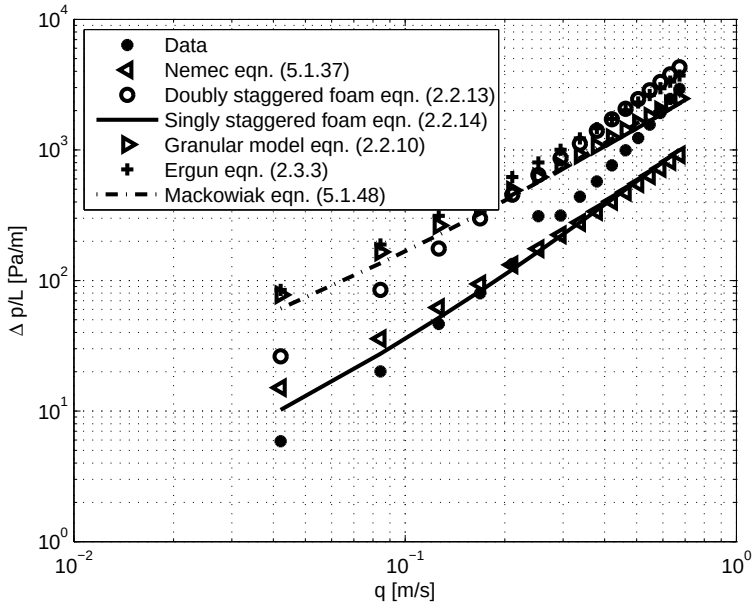

(b)

Figure 5.22: (a) Comparison of models with the Sonntag correction equal to 10%. (b) Pressure gradients of the different models and the data.

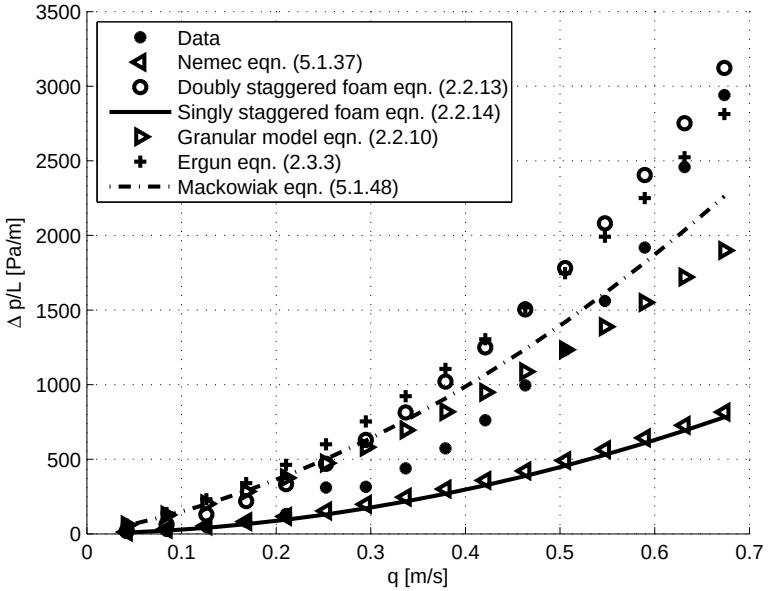

(a)

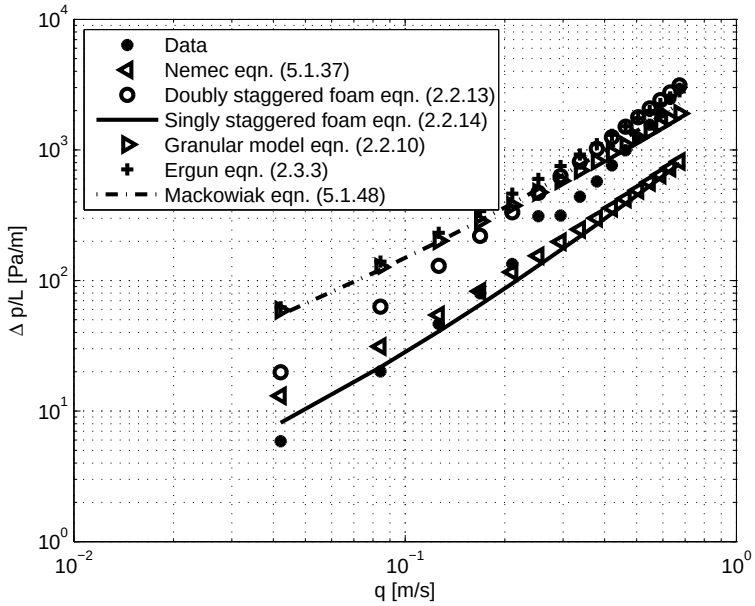

(b)

Figure 5.23: (a) Comparison of models with the Sonntag correction equal to 20%. (b) Pressure gradients of the different models and the data.

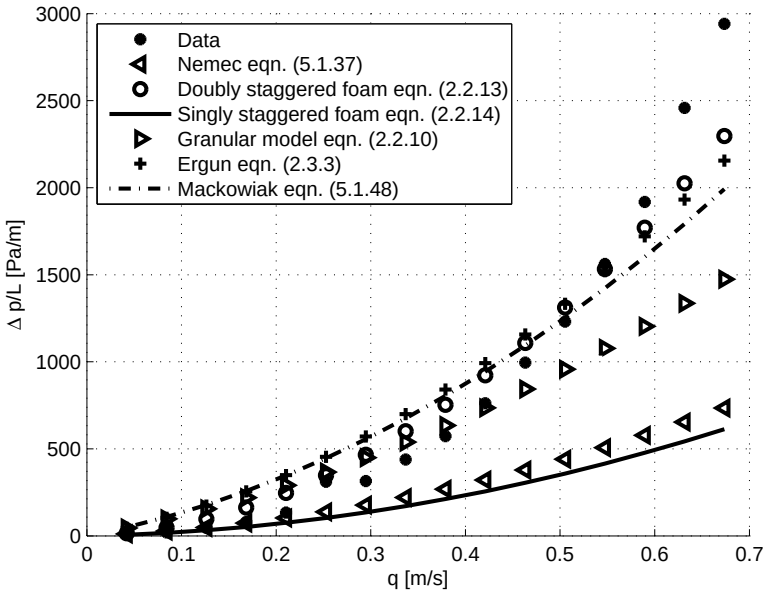

(a)

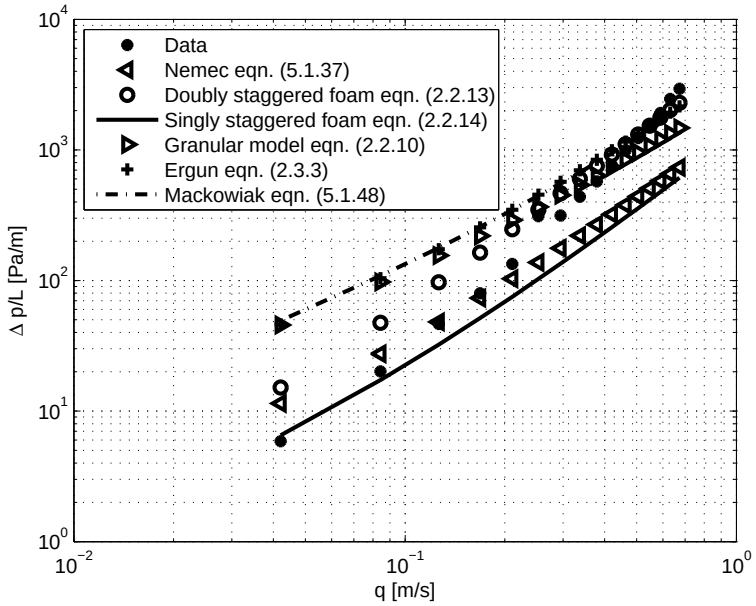

(b)

Figure 5.24: (a) Comparison of models with the Sonntag correction equal to 30%. (b) pressure gradients of the different models and the data.

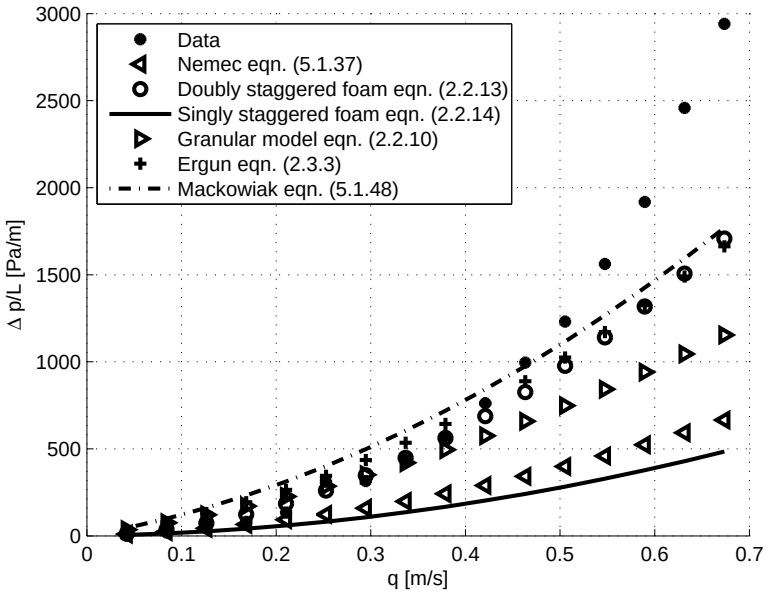

(a)

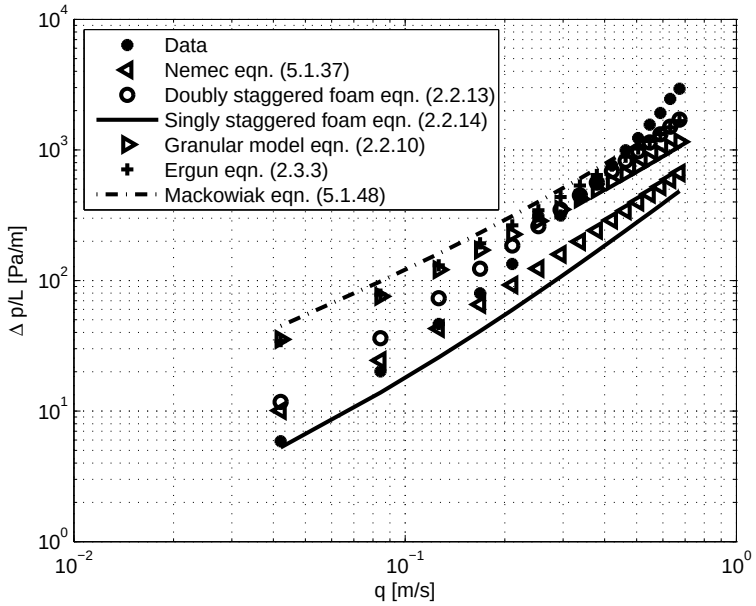

(b)

Figure 5.25: (a) Comparison of models with the Sonntag correction equal to 40%. (b) Pressure gradients of the different models and the data.

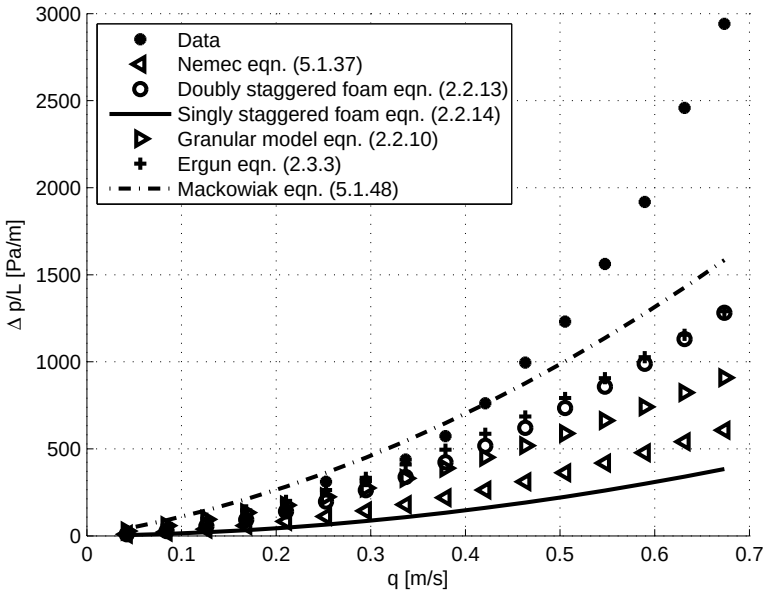

(a)

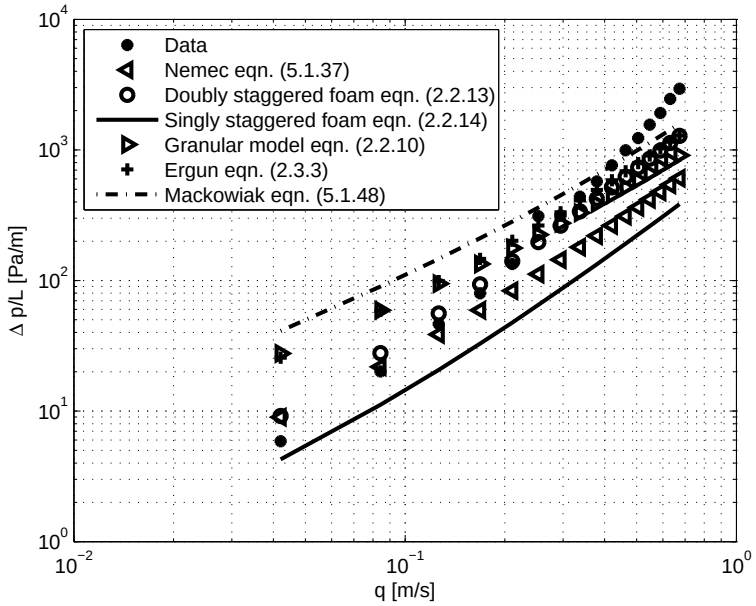

(b)

Figure 5.26: (a) Comparison of models with the Sonntag correction equal to 50%. (b) Pressure gradients of the different models and the data.

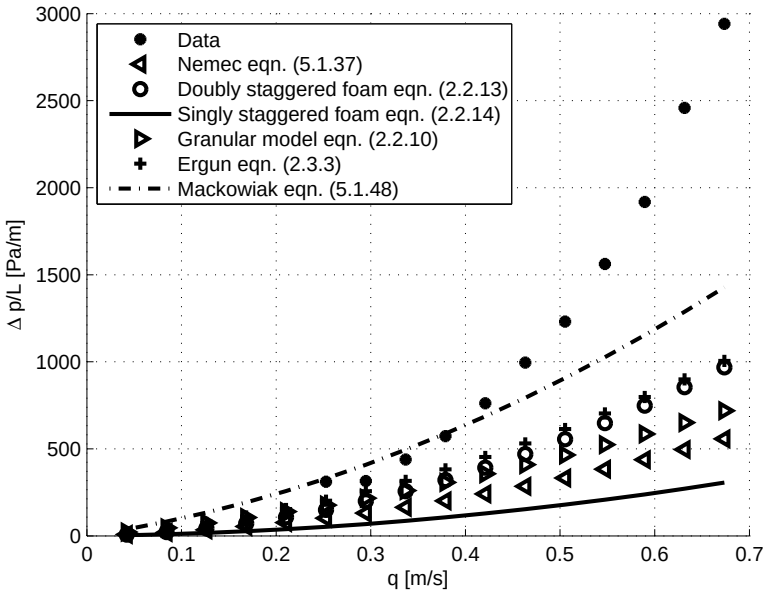

(a)

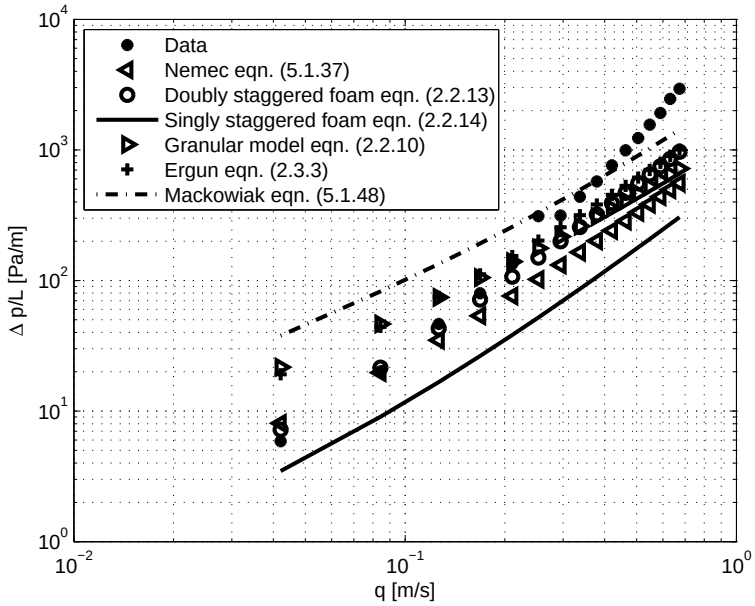

(b)

Figure 5.27: (a) Comparison of models with the Sonntag correction equal to 60%. (b) Pressure gradients of the different models and the data.

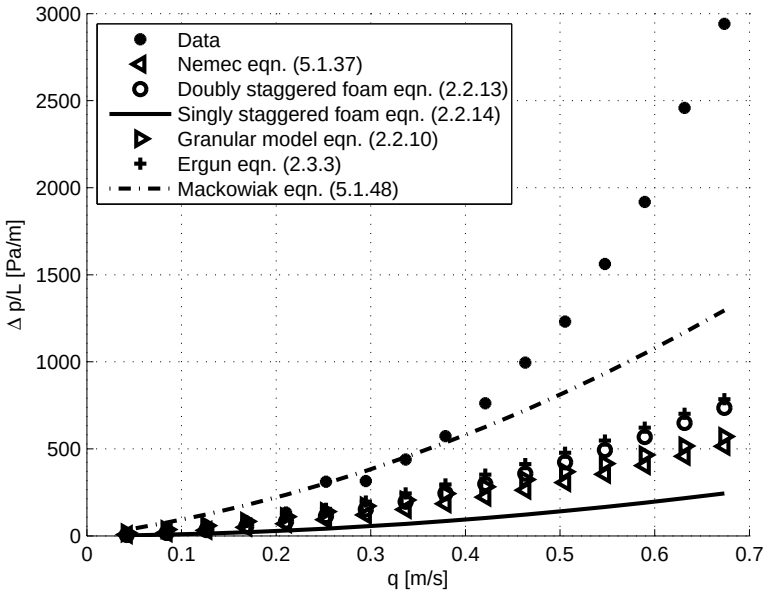

(a)

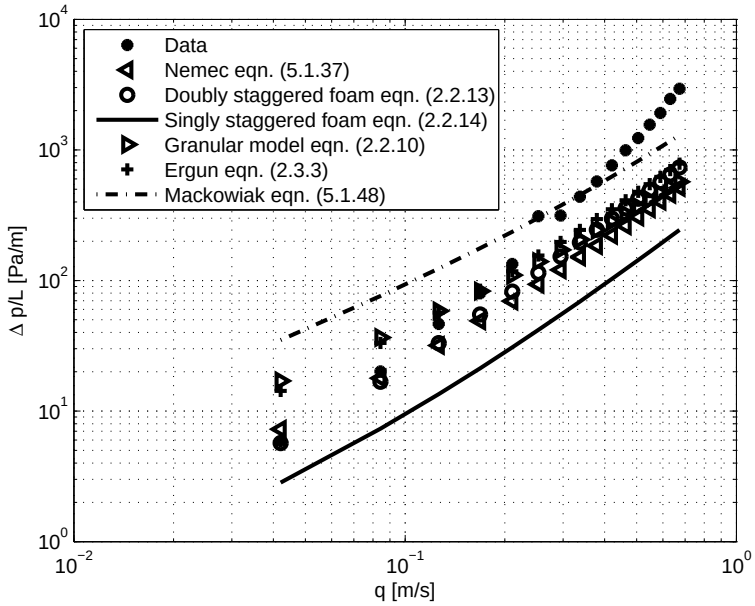

(b)

Figure 5.28: (a) Comparison of models with the Sonntag correction equal to 70%. (b) Pressure gradients of the different models and the data.

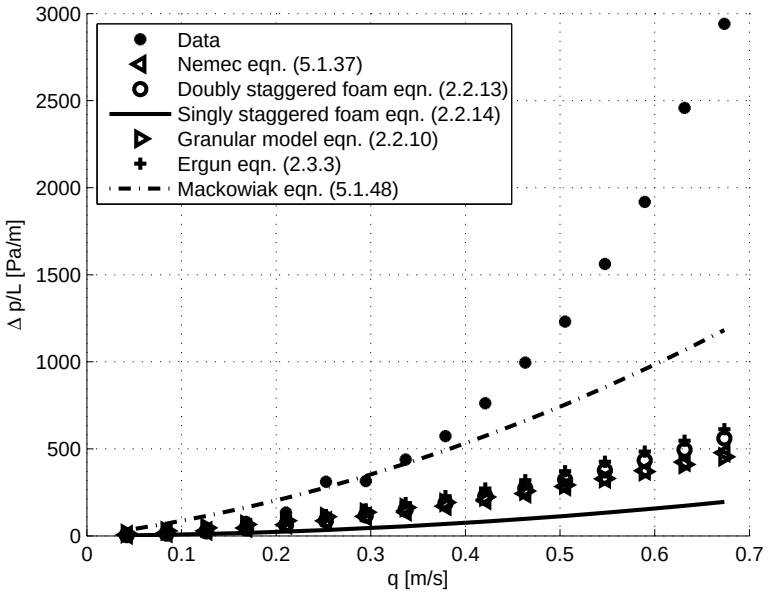

(a)

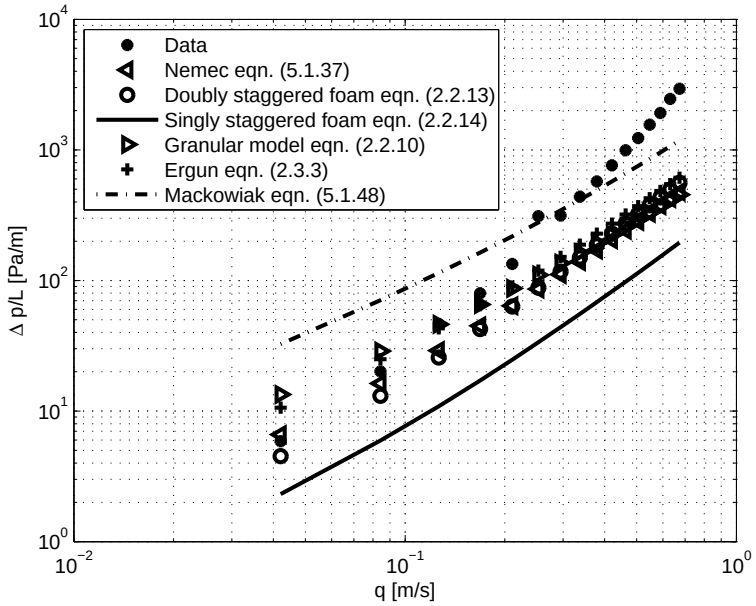

(b)

Figure 5.29: (a) Comparison of models with the Sonntag correction equal to 80%. (b) Pressure gradients of the different models and the data.

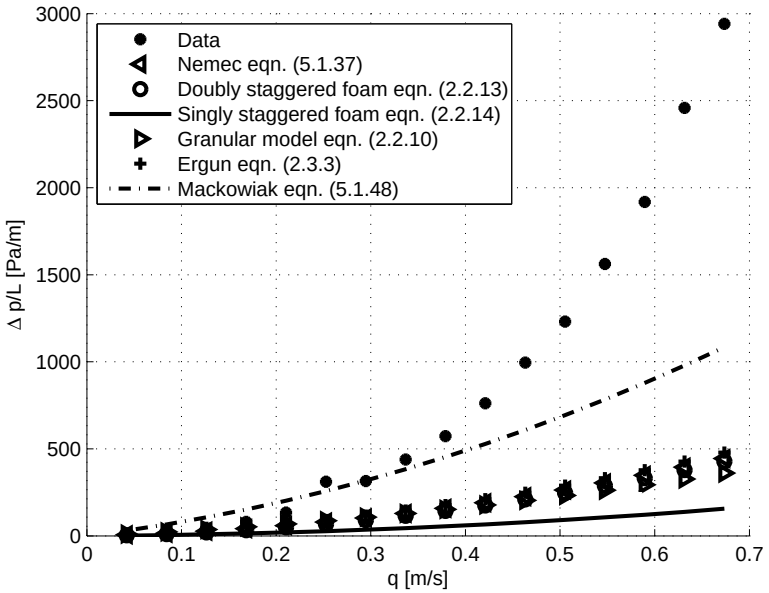

(a)

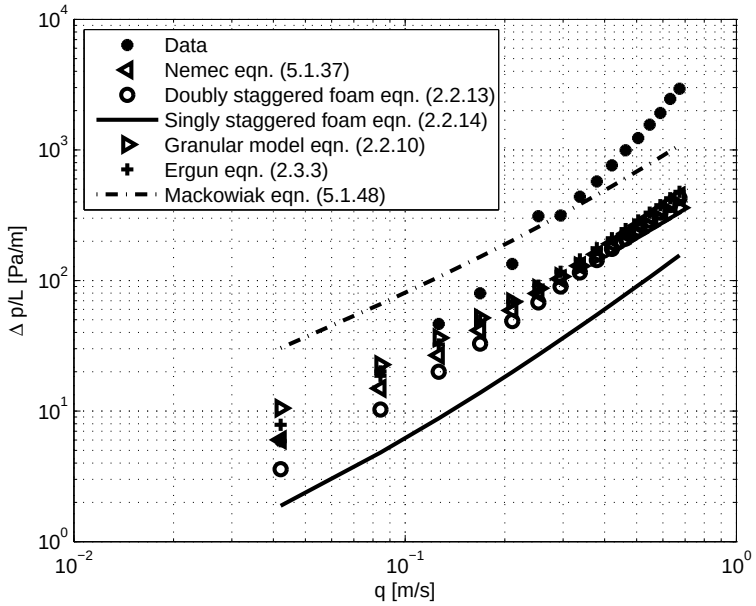

(b)

Figure 5.30: (a) Comparison of models with the Sonntag correction equal to 90%. (b) Pressure gradients of the different models and the data.

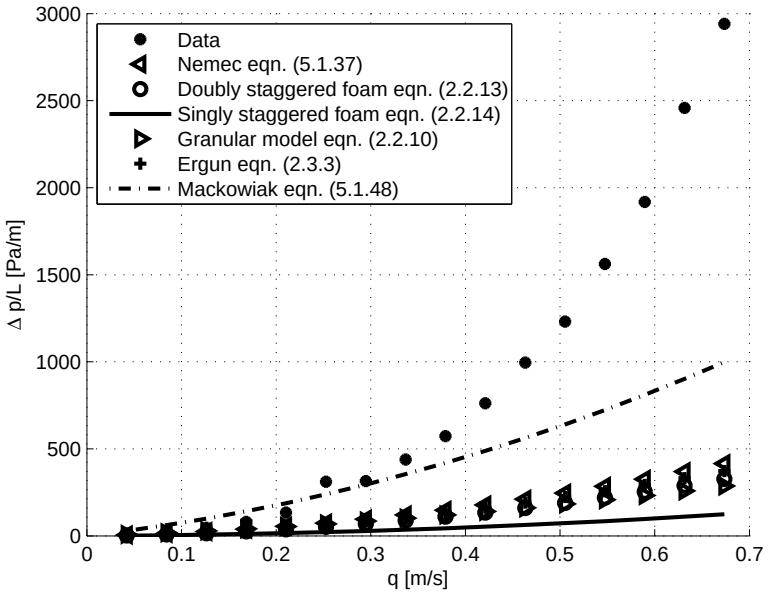

(a)

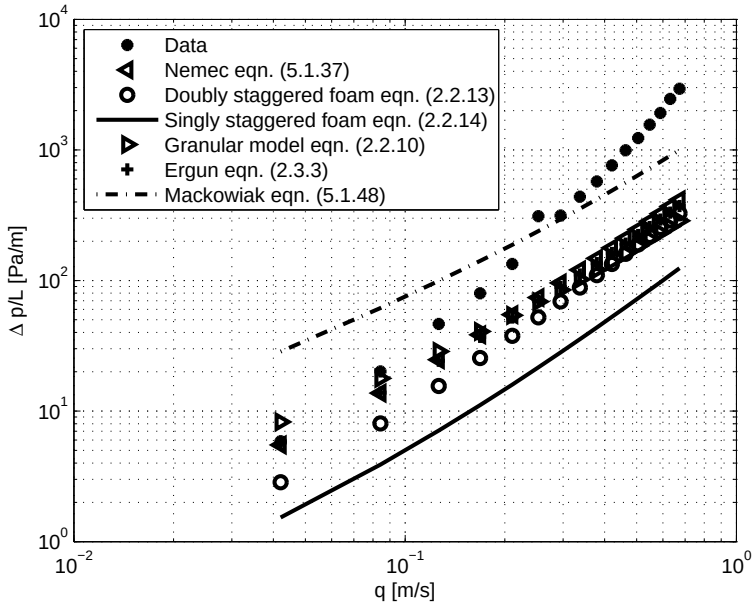

(b)

Figure 5.31: (a) Comparison of models with the Sonntag correction equal to 100%. (b) Pressure gradients of the different models and the data.

Chapter 6

Numerical simulation of flow in an absorption tower

Computational fluid dynamics (CFD) is widely used in industry. It serves as a tool to predict complex flow behavior. CFD is normally used in conjunction with physical data. The data is used to verify the output of the programme. CFD is thus a means to model analytical equations in complex flow regimes, and remains only an approximation to the real world event. The accuracy of the particular simulation depends on a variaty of factors such as grid size, fluid species, fluid speed and analytical assumptions regarding the fluid, to name only a few.

One of the most useful aspects of CFD is that one is able to simulate flow conditions in areas and situations that are analytically too complex or even impossible to solve. The comparison of empirically and analytically derived equations with CFD produce results which will prove highly useful in the further development of our understanding of flow through porous media.

The aim of the numerical simulation in *FORTRAN* is to compare results to the results of the analytical equations. More specifically, to compare the pressure drop given by numerical and analytical methods for a range of different superficial velocities. The accuracy of all of the predictive methods will be determined by the data acquired at the TUC.

6.1 One-dimensional flow simulation in cylindrical coordinates

To start the numerical process, the Navier-Stokes equation in cylindrical coordinates will be used. If the direction of the upward flow in the empty column is defined as the z-direction it follows that, for fully developed flow, the velocity will only have components in the z-direction. Thus the Navier-Stokes equation reduces to:

$$\rho\left(\frac{\partial v_z}{\partial t}+v_r\frac{\partial v_z}{\partial r}+\frac{v_\theta}{r}\frac{\partial v_z}{\partial \theta}+v_z\frac{\partial v_z}{\partial z}\right) = -\frac{\partial p'}{\partial z}+\rho g_z+\mu\left[\frac{1}{r}\frac{\partial}{\partial r}\left(r\frac{\partial v_z}{\partial r}\right)+\frac{1}{r^2}\frac{\partial^2 v_z}{\partial \theta^2}+\frac{\partial^2 v_z}{\partial z^2}\right], \tag{6.1.1}$$

where $\underline{v}=v_r\underline{e}_r+v_\theta\underline{e}_\theta+v_z\underline{e}_z$ and gives the velocity in the tower. The radius of the tower is given as the variable r and θ is the angle coordinate in the cylindrical coordinate system. In the case of fully developed flow the z-component of the velocity is independent of the angle,

θ and is also constant in the z-direction due to the constant pressure gradient. In addition fully developed flow is time independent so that Equation (6.1.1) reduces to:

$$0 = -\frac{\partial p'}{\partial z} + \rho g_z + \frac{1}{r}\mu\frac{\partial}{\partial r}\left(r\frac{\partial v_z}{\partial r}\right). \tag{6.1.2}$$

Gravity is a uniform vector field thus it follows that $\nabla \times \underline{g} = \underline{0}$. There exists a potential function ϕ such that $\underline{g} = grad\ \phi = \nabla\phi$. Due to the fact that the curl of a gradient is always equal to zero ($\nabla \times \overline{\nabla}\phi = 0$). The gravitational acceleration, $\underline{g}$, can thus be replaced by the gradient of its associated potential ϕ. Thus the body force term of the Navier-Stokes equation can be written as $\rho\underline{g} = \nabla\Omega$, with Ω the potential function that includes the density. It thus follows that the body force term and pressure gradient term in equation (6.1.2) can be simplified as follows:

$$\begin{aligned} -\frac{\partial p'}{\partial z} + \rho g_z &= -\frac{\partial p'}{\partial z} + \frac{\partial \Omega}{\partial z} \\ &= \frac{\partial}{\partial z}(\Omega - p') \\ &= \frac{\partial p}{\partial z}. \end{aligned} \tag{6.1.3}$$

Here p would be the actual static pressure measured in the tower. Equation (6.1.2) then simplifies to:

$$-\frac{dp}{dz} = \mu\frac{1}{r}\frac{\partial}{\partial r}\left(r\frac{\partial v_z}{\partial r}\right), \tag{6.1.4}$$

with $-\frac{dp}{dz}$ the constant pressure gradient in the z-direction.

6.1.1 Finite volume method for one-dimensional fully developed flow

6.1.1.1 Grid generation

The first step is to divide the domain into control volumes. In Figure 6.1 an example of a control volume is given. The nodal points are positioned midway between the boundaries of the control volumes as described by Versteegs Appendix B [23]. The number of nodal points used depends on the accuracy required. In Figure 6.1 five nodal points are used to serve as an example. Each node is surrounded by a control volume. The usual convention of CFD will be used as defined by Versteeg *et al* [23] and is given in Figure 6.1. A general nodal point is depicted by P and the adjacent points are depicted by W and E respectively. The *west* side face of the control volume is denoted by 'w', and the *east* side by 'e'. The distance between two nodal points is given as δr, and thus the length of a control volume is δr. Boundary values at the end points are prescribed as v_{zA} and v_{zB} respectively. In Figure 6.2 the graphical depiction given in Figure 6.1 is shown in a column. Figure 6.2 shows how Figure 6.1 occurs in the actual tower. The whole tower is thus divided into control volumes to make numerical simulations possible.

6.1.1.2 Discretisation

The most important step in the finite volume method is the integration of the governing equation over the control volume to yield a discretised equation at each nodal points. In

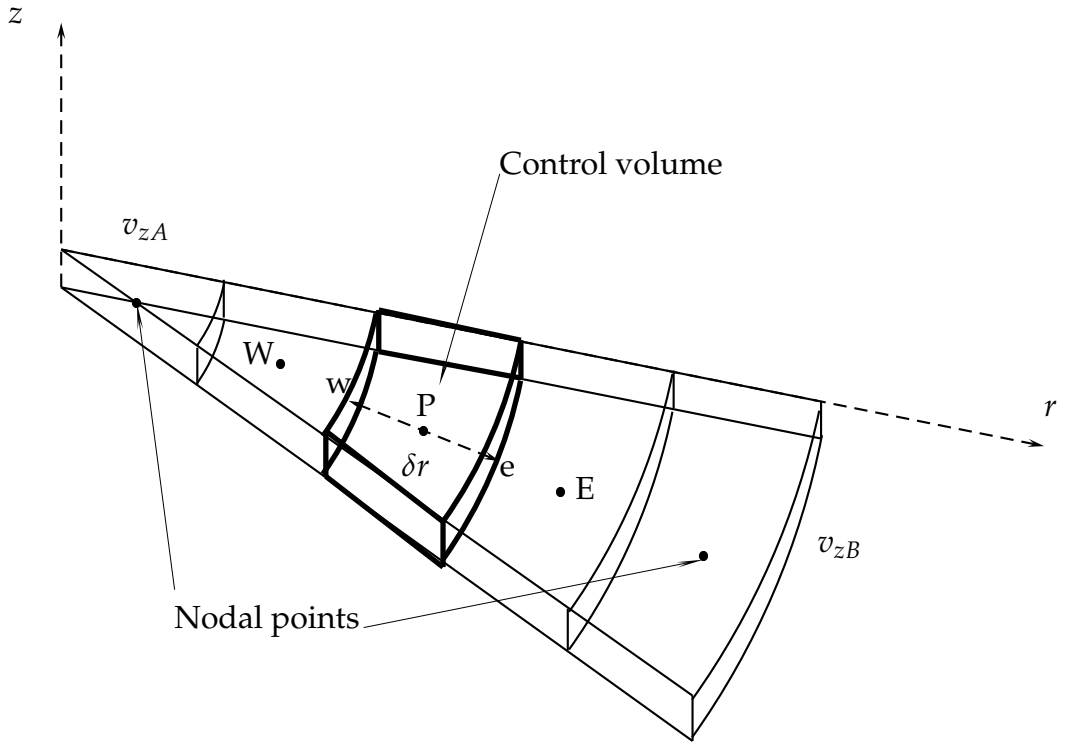

Figure 6.1: Discretisation in cylindrical coordinates with a graphical depiction of a control volume.

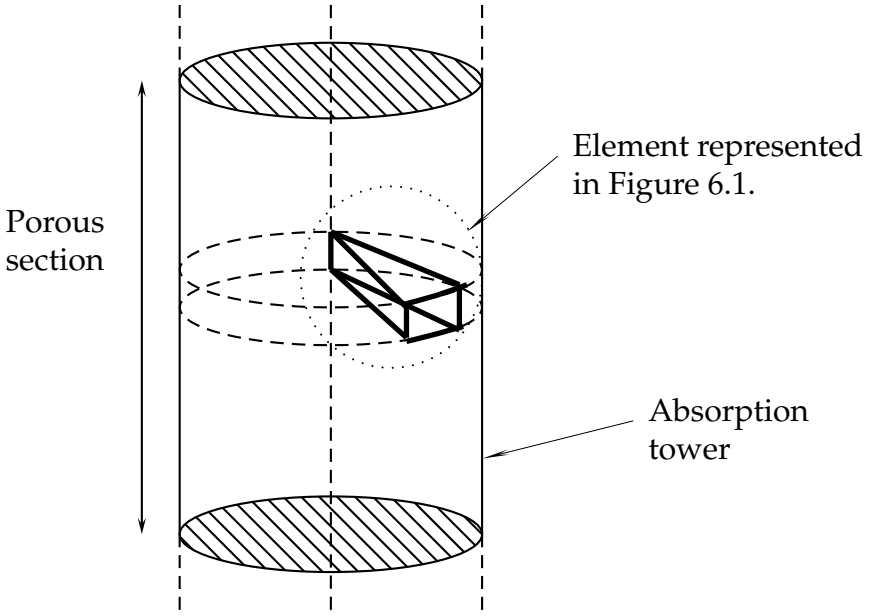

Figure 6.2: Schematic representation of an absorption tower with representation of a section of control volumes as depicted in Figure 6.1.

this case equation (6.1.4) is the governing equation and integrating over the control volume

gives:

$$\int_{\Delta V} \frac{1}{r}\,\mu\frac{\partial}{\partial r}\left(r\frac{\partial v_z}{\partial r}\right)\mathrm{d}V = -\int_{\Delta V}\frac{dp}{dz}\,\mathrm{d}V, \tag{6.1.5}$$

were V is the control volume. Rewriting equation (6.1.5) in terms of cylindrical coordinates as depicted in Figure 6.1, yields:

$$\int_0^L\int_0^{\delta\theta}\int_{r_w}^{r_e}\frac{1}{r}\,\mu\frac{\partial}{\partial r}\left(r\frac{\partial v_z}{\partial r}\right) r\,\mathrm{d}r\,\mathrm{d}\theta\,\mathrm{d}z = -\int_0^L\int_0^{\delta\theta}\int_{r_w}^{r_e}\frac{\partial p}{\partial z}\,r\,\mathrm{d}r\,\mathrm{d}\theta\,\mathrm{d}z, \tag{6.1.6}$$

with L the height of a control volume. The angle, θ, is taken from zero to $\delta\theta$ radials, because the control volume must be as small as possible where $\delta\theta \to 0$. After integrating equation (6.1.6) it follows that:

$$\left(\mu r\frac{\partial v_z}{\partial r}\right)\Bigg|_{r_w}^{r_e} = -\frac{\partial p}{\partial z}\frac{1}{2}\left(r_e^2 - r_w^2\right). \tag{6.1.7}$$

Each partial derivative becomes an ordinary derivatives as the pressure and the velocity are only dependent on one variable. In full, equation (6.1.7) becomes:

$$2\mu\left[\left(r\frac{dv_z}{dr}\right)_{r_e} - \left(r\frac{dv_z}{dr}\right)_{r_w}\right] = -\frac{dp}{dz}\left(r_e^2 - r_w^2\right). \tag{6.1.8}$$

Using the central differencing practice described by Versteeg [23] it follows that equation (6.1.8) in discretized form is given by:

$$2\mu\left[r_e\frac{v_{zE} - v_{zP}}{\delta r} - r_w\frac{v_{zP} - v_{zW}}{\delta r}\right] = -\frac{dp}{dz}\left(r_e^2 - r_w^2\right). \tag{6.1.9}$$

After gathering like terms it follows that:

$$\left(\frac{2\mu r_e}{\delta r} + \frac{2\mu r_w}{\delta r}\right)v_{zP} = \left(\frac{2\mu r_e}{\delta r}\right)v_{zE} + \left(\frac{2\mu r_w}{\delta r}\right)v_{zW} + \frac{dp}{dz}\left(r_e^2 - r_w^2\right). \tag{6.1.10}$$

Defining the coefficient of v_{zP} as a_P and the coefficients of v_{zW} and v_{zE} as a_W and a_E respectively, equation (6.1.10) becomes:

$$a_P v_{zP} = a_W v_{zW} + a_E v_{zE} + S_u, \tag{6.1.11}$$

were S_u is part of the source term defined as $S_u + S_p v_{zP}$. The coefficients of equation (6.1.11) for one dimensional flow in a column described in cylindrical coordinates are given in Table 6.1.

a_W	a_E	a_P	S_p	S_u
$\left(\frac{2\mu r_w}{\delta r}\right)$	$\left(\frac{2\mu r_e}{\delta r}\right)$	$a_W + a_E - S_p$	0	$\frac{dp}{dz}\left(r_e^2 - r_w^2\right)$

Table 6.1: Coefficients of the discretized equation (6.1.11).

From equation (6.1.11) a set of discreet equations is produced, describing the velocity at each nodal point. Thus given initial conditions at every point, the system of equations defined at each point can be solved using any linear algebraic technique. The *tri-diagonal matrix algorithm* (TDMA) is a technique especially designed to solve these matrices in the context of CFD [23].

The boundaries must be handled separately. Equation (6.1.8) is used but just the boundary nodal points are used, one at a time. The resulting coefficients for the first and last boundary nodes are given in Table 6.2.

Boundary	a_W	a_E	a_P	S_p	S_u
v_{zA}	0	$\left(\frac{2\mu r_e}{\delta r}\right)$	$a_E - S_p$	$-\frac{2\mu r_w}{\delta r/2}$	$\frac{dp}{dz}\left(r_e^2 - r_w^2\right) + \frac{2\mu r_w}{\delta r/2} v_{zA}$
v_{zB}	$\left(\frac{2\mu r_w}{\delta r}\right)$	0	$a_W - S_p$	$-\frac{2\mu r_e}{\delta r/2}$	$\frac{dp}{dz}\left(r_e^2 - r_w^2\right) + \frac{2\mu r_e}{\delta r/2} v_{zB}$

Table 6.2: Coefficients of the discretized equation (6.1.11) at the first and last boundary nodes.

6.1.1.3 Results

After implementing the TDMA, the velocity profile of one-dimensional flow through a tower is obtained. The profile is depicted in Figure 6.3. To verify the numerical results, known analytical equations for Poiseuille flow were used. It is well known that the maximum velocity in fully developed Poiseuille flow is given by:

$$v_{max} = -\frac{R^2}{4\mu}\frac{dp}{dz}, \tag{6.1.12}$$

with R the radius of the particular column. Choosing the radius of the column as $0.01m$, the viscosity as $0.001kg/ms$ and the pressure gradient as $200Pa/m$ it follows theoretically that the maximum velocity is equal to $5m/s$. In Figure 6.3 it is shown that the theoretical maximum value is exactly what the numerical procedure predicted.

6.2 Simulation of flow through porous media in one dimension

If the fluid under consideration is a Newtonian fluid, the interstitial Navier-Stokes equation is given by the following equation:

$$\rho\frac{\partial \underline{v}}{\partial t} + \nabla\cdot(\rho\underline{v}\,\underline{v}) + \nabla p - \mu\nabla^2\underline{v} = \underline{0}. \tag{6.2.1}$$

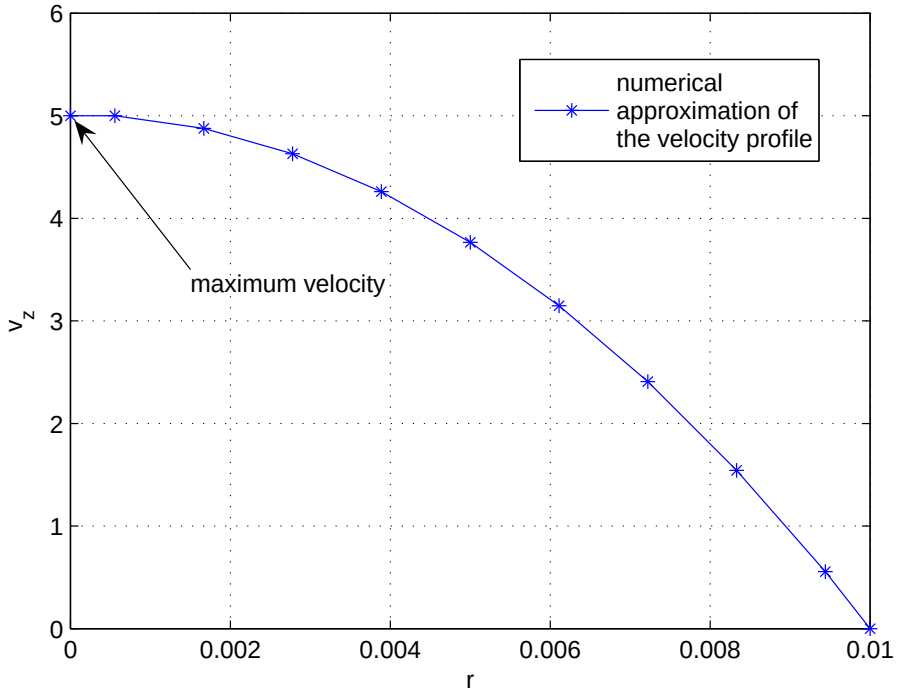

Figure 6.3: Half the velocity profile of one-dimensional flow in cylindrical coordinates.

Taking the phase average of the Navier-Stokes equation (6.2.1) then gives [6]:

$$\rho\frac{\partial q}{\partial t} + \rho\nabla\cdot\left(\underline{q}\underline{q}/\epsilon\right) + \epsilon\nabla p_f - \mu\nabla^2\underline{q} + \rho\nabla\cdot\langle\{\underline{v}\}\{\underline{v}\}\rangle = -\frac{1}{\mathcal{U}_o}\iint\limits_{S_{fs}}(\underline{n}\{p\} - \mu\,\underline{n}\cdot\nabla\underline{v})\,\mathrm{d}S. \tag{6.2.2}$$

To calculate the integrals by means of the finite volume method, a certain number of assumptions must be made. The first assumption is that $\nabla\cdot\langle\{\underline{v}\}\{\underline{v}\}\rangle = 0$ everywhere. Here a uniform superficial velocity profile is assumed throughout the porous medium. At the boundaries the superficial velocity, q, is assumed to be zero. The higher the porosity the more reasonable this assumption. But with low porosities this assumption will be invalid. The higher the porosity the greater the extent to which the fluid is forced to move alongside the boundary. The exact velocity at the boundary is not known. Implementing these assumptions with the flow fully developed and occurring only in the z-direction, equation (6.2.2) becomes:

$$\frac{\partial p_f}{\partial z} - \mu\frac{1}{r}\frac{\partial}{\partial r}\left(r\frac{\partial q_z}{\partial r}\right) = -\frac{1}{\mathcal{U}_o}\iint\limits_{S_{fs}}(\underline{n}\widetilde{p} - \mu\,\underline{n}\cdot\nabla\underline{v})\,\mathrm{d}S. \tag{6.2.3}$$

After closure with the RUC it follows that the integral in equation (6.2.3) reduces to $\mu q_z F$, with F the overall shear factor and expressed by:

$$Fd_s^2 = \frac{25.4(1-\epsilon)^{4/3}}{\left(1-(1-\epsilon)^{1/3}\right)\left(1-(1-\epsilon)^{2/3}\right)^2} + \frac{c_d(1-\epsilon)}{2\epsilon\left(1-(1-\epsilon)^{2/3}\right)^2} Re_{qd_s}, \tag{6.2.4}$$

for granular porous media [7]. Thus equation (6.2.3) becomes:

$$\frac{\partial p_f}{\partial z} - \mu \frac{1}{r}\frac{\partial}{\partial r}\left(r\frac{\partial q_z}{\partial r}\right) = -\mu q_z F. \tag{6.2.5}$$

Applying the finite volume method it follows that:

$$\int_0^L\int_0^{\partial\theta}\int_{r_w}^{r_e} \frac{\partial p_f}{\partial z}\, r\, \mathrm{d}r\mathrm{d}\theta\mathrm{d}z - \mu\int_0^L\int_0^{\partial\theta}\int_{r_w}^{r_e} \frac{\partial}{\partial r}\left(r\frac{\partial q_f}{\partial r}\right)\mathrm{d}r\mathrm{d}\theta\mathrm{d}z = -\int_0^L\int_0^{\partial\theta}\int_{r_w}^{r_e} \mu q_z F r\, \mathrm{d}r\mathrm{d}\theta\mathrm{d}z, \tag{6.2.6}$$

and after integration is reduced to:

$$\frac{dp_f}{dz}\left(r_e^2 - r_w^2\right) - 2\mu\left(r\frac{dq_z}{dr}\right)\Big|_{r_e} + 2\mu\left(r\frac{dq_z}{dr}\right)\Big|_{r_w} = -\mu F q_z\left(r_e^2 - r_w^2\right). \tag{6.2.7}$$

After discretisation is carried out and like terms are gathered the resulting discretised equation is given by:

$$\left(\frac{2\mu r_w}{\delta r} + \frac{2\mu r_w}{\delta r} + \mu F\left(r_e^2 - r_w^2\right)\right) q_{zP} = \left(\frac{2\mu r_e}{\delta r}\right) q_{zE} + \left(\frac{2\mu r_w}{\delta r}\right) q_{zW} - \frac{dp_f}{dz}\left(r_e^2 - r_w^2\right). \tag{6.2.8}$$

Writing equation (6.2.8) in the form of equation (6.1.11), the coefficients are easily extracted and are given in Table 6.3. The shear factor , F, is taken as the factor derived in the RUC model with general closure. This is a further assumption as the expression for F was derived with a uniform superficial velocity. Closure cannot be performed if q is not taken as uniform,

a_W	a_E	a_P	S_p	S_u
$\left(\frac{2\mu r_w}{\delta r}\right)$	$\left(\frac{2\mu r_e}{\delta r}\right)$	$a_W + a_E - S_p$	-$\mu\left(r_e^2 - r_w^2\right) F$	$-\frac{dp_f}{dz}\left(r_e^2 - r_w^2\right)$

Table 6.3: Coefficients of the discretized equation (6.1.11) for flow in porous media.

so the true expression for the shear factor, F, is not known. The expression for F depends on which of the RUC models are used, as described in Section 2.2. Equation (6.2.8) was implemented in the programming language *FORTRAN* and the result obtained is discussed in the following subsections.

6.2.1 Sensitivity analysis

According to Versteeg [23] there are three mathematical concepts that determine the success of the numerical solution. They are *convergence*, *consistency* and *stability*. These three criteria will be investigated and discussed for the numerical program used in this work. The parameters of the programme are based on the data of glass Raschig rings with a Sonntag correction of 20%, as described in Chapter 5.

6.2.1.1 Convergence

To adhere to the condition of convergence, the numerical solution should approach the exact solution as the control volume size is reduced to zero. Of course this is not practically possible as the roundoff errors would influence the solution long before a grid spacing close to zero is achieved. The analytical solution for the superficial velocity calculated with the granular RUC model is exactly equal to the numerical solution, namely $1.014938 m/s$. The latter is achieved at a pressure gradient equal to $2000 Pa/m$ and a porosity of 0.46. This result was achieved with the radius of the column divided with 7 grid points. In comparing the numerical solution to the analytical solution, the boundary conditions were made adiabatic at both walls. The reason for this is that the RUC model assumes a uniform superficial velocity, q, through the porous medium. Since the boundaries are adiabatic the most accurate correlation to the RUC model will be retrieved.

When the porous medium is removed out of the tower the problem reduces to Poiseuille flow. The analytical solution for the maximum value of the fully developed velocity profile in the column can thus easily be calculated. In Figure 6.4 the velocity profile through an open column is given. Using equation (6.1.12) the maximum value of the velocity profile through an open column is calculated to be equal to $3.336 \times 10^4 m/s$ (refer to Figure 6.4). This is confirmation of the accuracy of the numerical solution.

6.2.1.2 Consistency

The numerical solution should also produce a consistent answer. This is achieved by showing that the numerical solution tends to the analytical solution as the grid spacing tends to zero. To test the consistency, 7, 11 and 15 grid points were used respectively. The result of the average superficial velocities were $1.014938 m/s$ for all three grid sizes respectively. Thus with the decrease in control volume size the numerical solution remained constant.

6.2.1.3 Stability

The column diameter was varied from $7 cm$ to $70 cm$ and the answer remained constant and stable. Neither the change in the boundary conditions, column diameter nor porosity caused the numerical solution to diverge. Thus the program can be assumed stable. An example of the programs stability for a changing porosity is given in Figure 6.5.

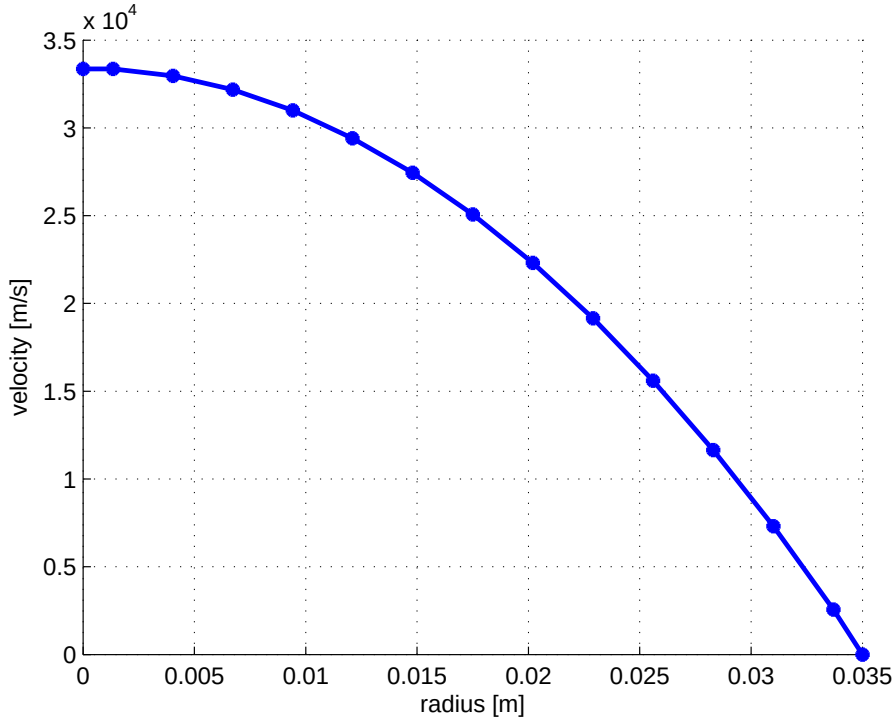

Figure 6.4: Half the velocity profile of one-dimensional flow in cylindrical coordinates through an open column.

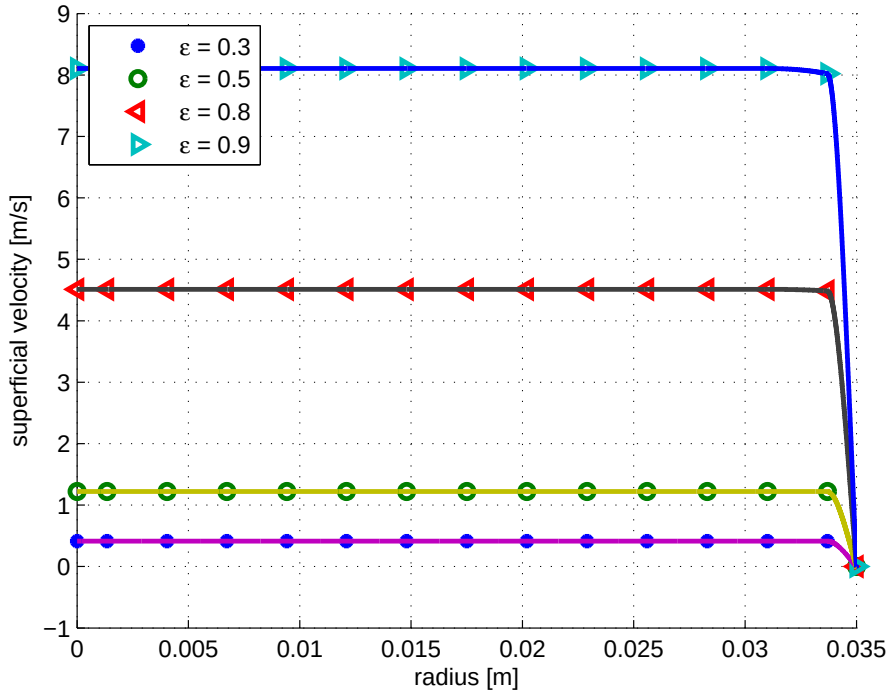

Figure 6.5: Half the velocity profile of one-dimensional flow in cylindrical coordinates through column with a porous medium present.

It is evident from Figure 6.5 that as the porosity decreases the superficial velocity decreases. This is thought to be due to the increase of resistance to the flow.

6.2.2 Comparison to experimental data

In comparing the numerical simulations to the experimental data, the superficial velocity was set to zero at the boundaries. Although this is not totally accurate it is at least more feasible than a constant superficial velocity. The velocity would probably not be equal to zero at the boundary. Further simulations or experiments should be carried out to determine the actual velocity at the boundary. In this study the superficial velocity at the boundary will however be kept zero.

In Figure 6.6 and 6.7 the comparison of the numerical solution to the experimental data for glass Raschig rings are given. The results of the analytical models described in chapter 5 are also provided. The numerical approximations were carried out with and without the sphericity-factor. A Sonntag correction of 20% was implemented and a form drag value of 1.9 [7]. As expected, the numerical solution predicts the same result as the theoretical granular RUC model with a sphericity-factor.

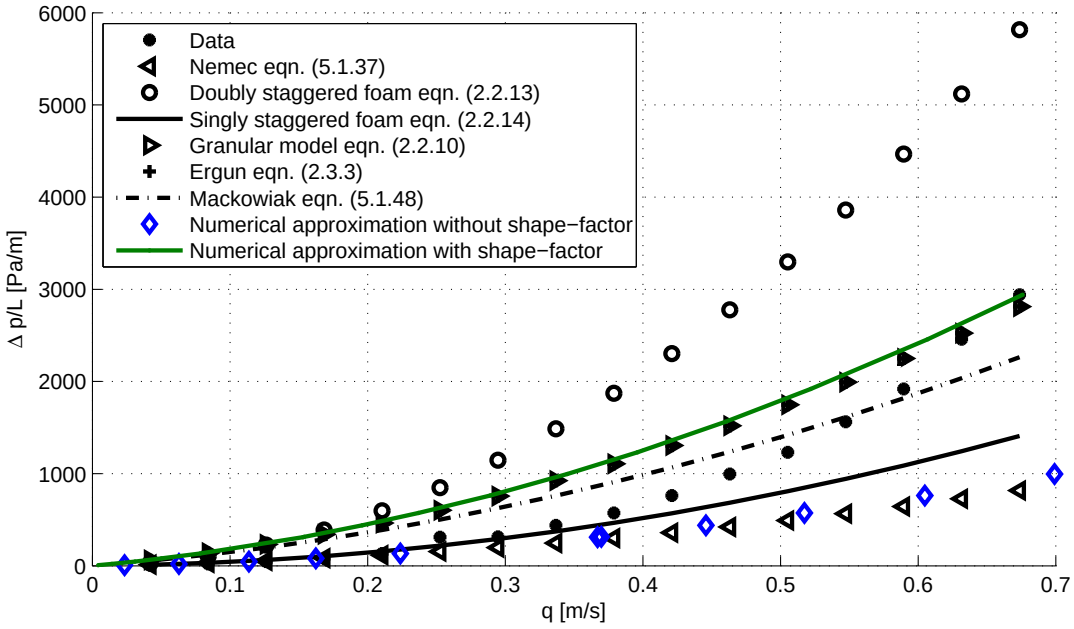

Figure 6.6: Comparison of the numerical approximations with the experimental data acquired. The theoretical models described in chapter 5 are also presented. Glass Raschig rings were used.

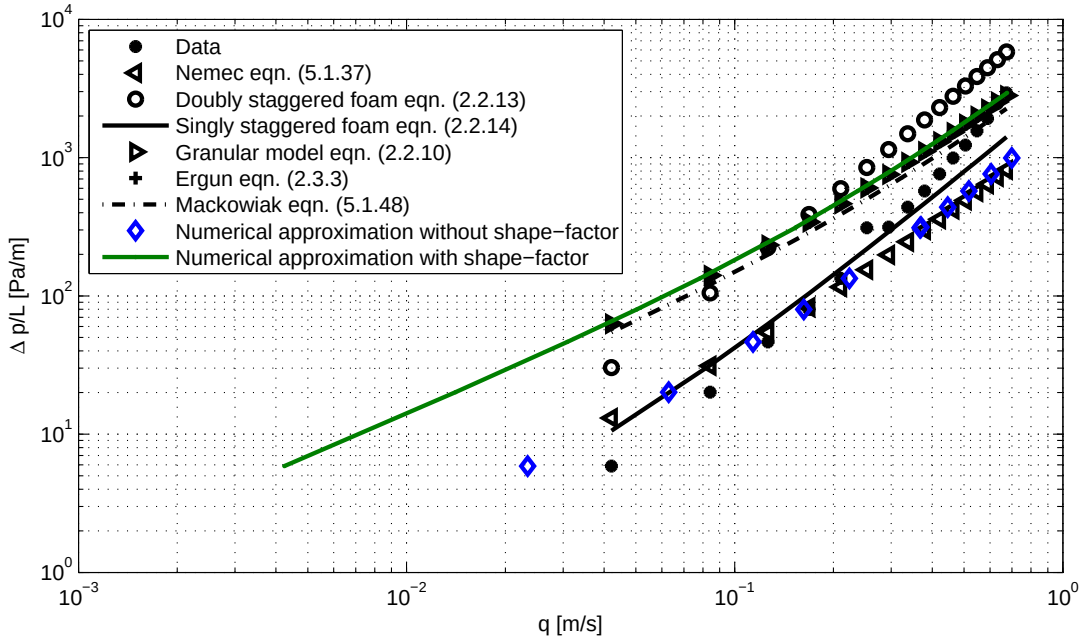

Figure 6.7: Comparison on a log-log scale of the numerical approximations with the experimental data acquired. The theoretical models described in chapter 5 are also presented. Glass Raschig rings were used.

Chapter 7

Fluidization

A fluidized bed is a packed bed for which the gas velocity is so high that the particles become loose and the particle-fluid mixture exhibits a fluid-like behaviour.

Consider the situation where the superficial velocity is increased from zero to past the velocity for fluidization and then back down to zero again (refer to Figure 7.1).

As the superficial velocity is increased the pressure drop increases. This is the region where the Ergun equation is typically applicable. As point *B* is reached the superficial velocity increases but the pressure drop remains constant. This is the point where the packing material begins to float in the fluid, as can be seen in Figure 7.1 (a). The packed bed height starts to increase while the superficial velocity increases 7.1 (b). From point *C* to point *D*, the pressure drop stays constant while the superficial velocity increases further and the bed height also increases somewhat.

Proceeding backwards on the curve from point *D* through *C* to *E* and finally *O*, it is evident that point *C* is a point of significance. This point is called the point of minimum fluidization, U_{mf}, as this is the point where fluidization will begin if the superficial velocity is increased from zero to the velocity corresponding to point *D*. Path *ABCD* will thus be followed only once [5]. This is at the initial increase of the superficial velocity. This is seen in Figure 7.1. As the superficial velocity is decreased past that velocity corresponding to point *E*, the bed height remains higher than the bed height for the same superficial velocity on path *ABCD* (refer to Figure 7.1 (b)). This happens because the particles that have been fluidized, settle back into a looser arrangement compared to the case of the pre-fluidization packing. In a powder packed bed there exists two regimes, namely the dense phase regime and the transport phase regime [21]. Figure 7.2 shows the four stages of the dense phase regime. The particulated regime occurs when the bed expands without bubbling. With the powder used in this study the transition from particulated to bubbling regimes were not clearly defined. Thus once the bed starts to bubble it is no trivial task to determine the effective bed height. To compile a result such as in Figure 7.1 (b), the bed has to be left for a period of time while the bed height is frequently measured. Following a method described by Sookai [21] the effective height can be measured by interpolation. Due to time constraints this interpolation technique could not be experimentally verified for the acquired data. The bed is only completely fluidized if the entire weight of the bed is supported by the fluid. The turbulent and the transport regimes are shown in Figure 7.2 and mentioned for interest's sake and fall outside of the scope of this study. In Figure 7.3 a photograph is provided of physical bubbles formed in the experiments carried out. To verify the preceding theory, three powder samples were used, as described in Chapter 4, to retrieve data before and after fluidization. In Figures 7.4, 7.5 and 7.6 the results of the fluidization of the three powders

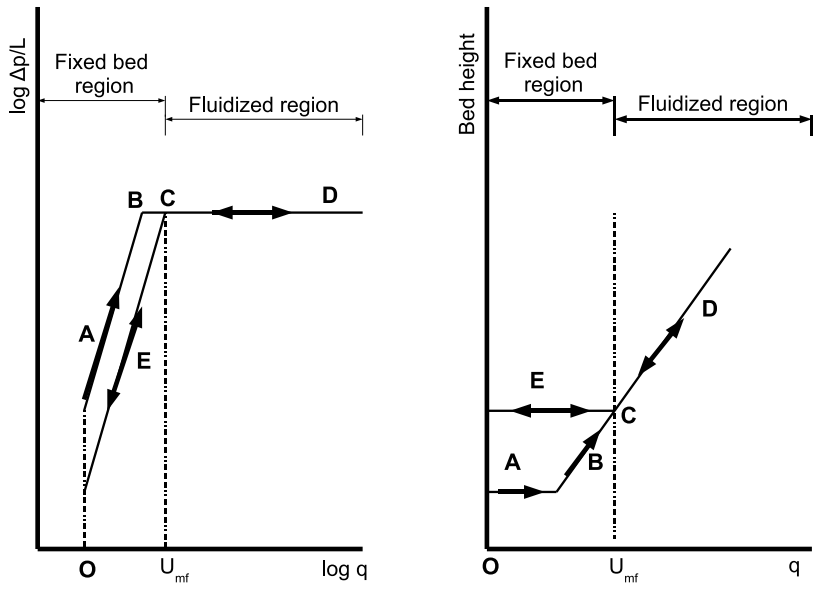

(a) (b)

Figure 7.1: (a) Behavior of the pressure drop with increase and decrease in superficial velocity in a particle bed and (b) the behavior of the bed height with an increase and decrease in superficial velocity in a particle bed .

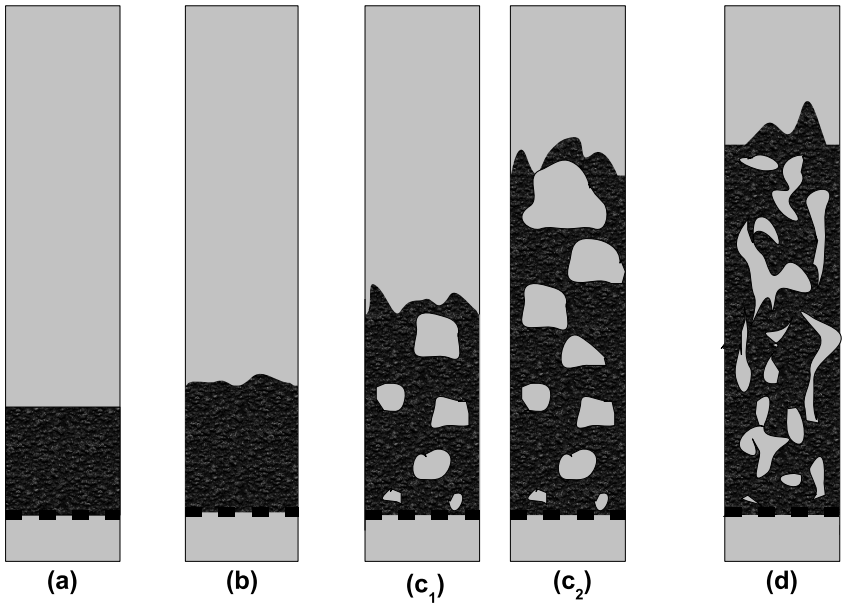

Figure 7.2: (a) The fixed bed regime, (b) the particulated regime, (c_1) and (c_2) is the bubbling regime and (d) is the turbulent regime.

are given. The dash-dot curves are with the initial increase of gas velocity while the solid curves are the decrease in superficial velocity after fluidization. Any further fluidization would then follow the solid curve. The effect of the loose arrangement of particles is best seen with the large particles ($750 - 1000\mu m$). There occurs a great decrease of the pressure

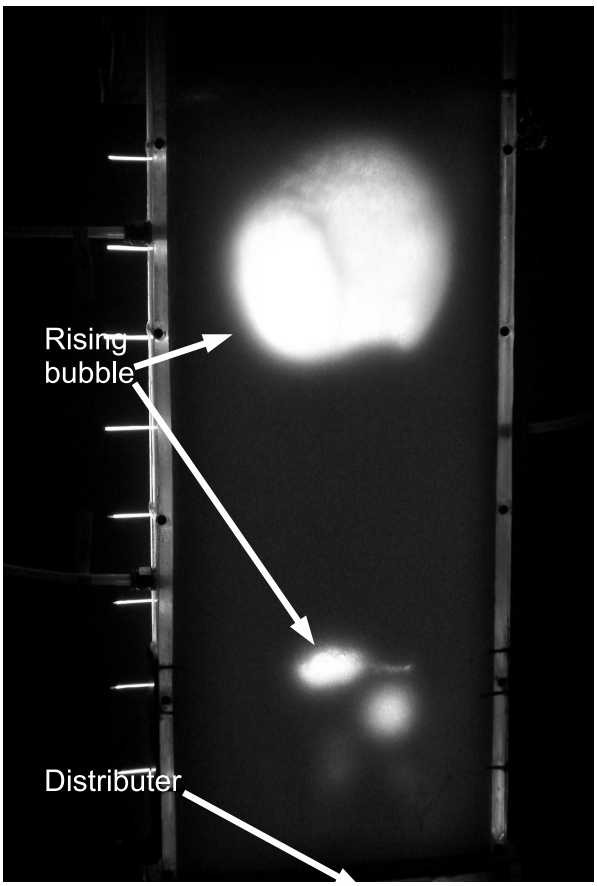

Figure 7.3: A rising bubble in a two-dimensional bubbling bed .

drop after fluidization as compared with the pressure drop associated with the other two powders.

With the smallest particles ($100 - 200\mu m$) the point of fluidization is not clearly defined. A small "hump" occurs in the region where fluidization was expected to occur (refer to Figure 7.4). The behavior depicted in Figure 7.1 (a)/(b) is ideal behavior and many deviations from this behavior can occur. According to Davidson [5] the "hump" mentioned earlier can occur as a result of the relatively small column used. The particles can interlock with each other and thus the wall can exert an additional force on the bed. The overshoot of the pressure drop can thus be attributed to this frictional force of the walls on the bed. When working with the particles with a size distribution between $400 - 600\mu m$, the point of fluidization is not perfectly defined. This may be attributed to the non-uniform distribution of particles in the bed. Preferential flow can form, resulting in some areas starting to fluidize, while other areas still exist as a fixed bed. The effect of is that a more gradual transition from a fixed to a fluidized bed will be created [5] (refer to Figure 7.5). In Figure 7.6 the fluidization of the large powder sizes ($750 - 1000\mu m$) is given. Deviations from the ideal model can be attributed to various physical phenomena. If the distributor does not distribute the gas uniformly, channelling may occur [5]. In Figure 7.7 a photographic example is provided to illustrate channelling. The channelling is caused by a large particle size distribution. After fluidization the larger particles will settle at the bottom of the tower while the finer particles will settle at the top part of the tower. As illustrated in Figure 7.7 the larger particles function as a pore distributor for the finer particles and the result are channels between the finer par-

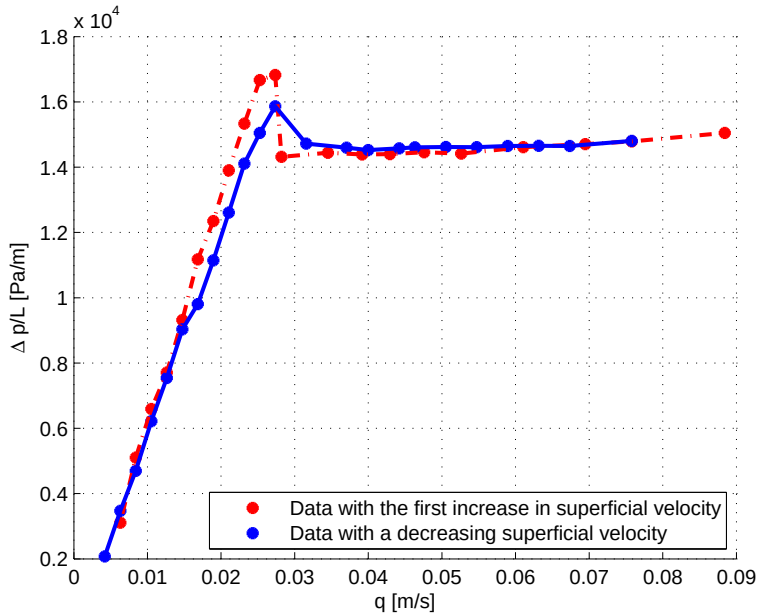

Figure 7.4: Fluidization of a glass powder with a distribution of particle sizes between $100 - 200\mu m$.

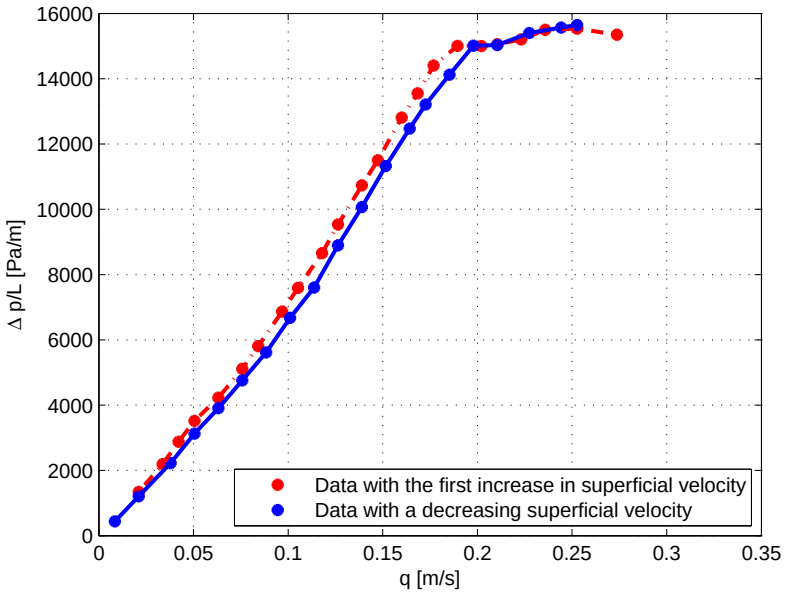

Figure 7.5: Fluidization of a glass powder with a distribution of particle sizes between $400 - 600\mu m$.

ticles. Circulation patterns may also occur which cause abnormal behavior of the pressure drop [5]. Many more causes for deviations from the ideal model may be listed, however, a considerable amount of information regarding these deviations can be retrieved just by looking at the point of minimum fluidization. The point of fluidization can be determined both experimentally and theoretically. Both methods will be discussed and compared in the following two sections.

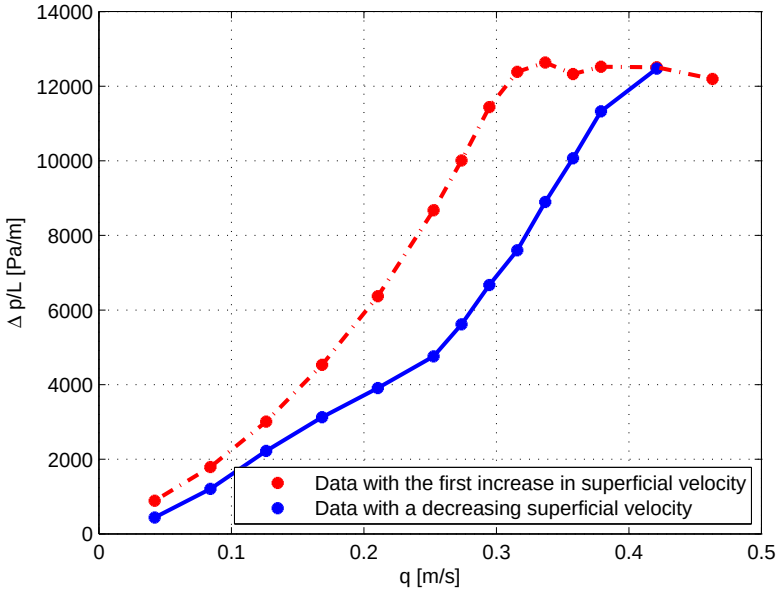

Figure 7.6: Fluidization of a glass powder with a distribution of particle sizes between $750 - 1000\mu m$.

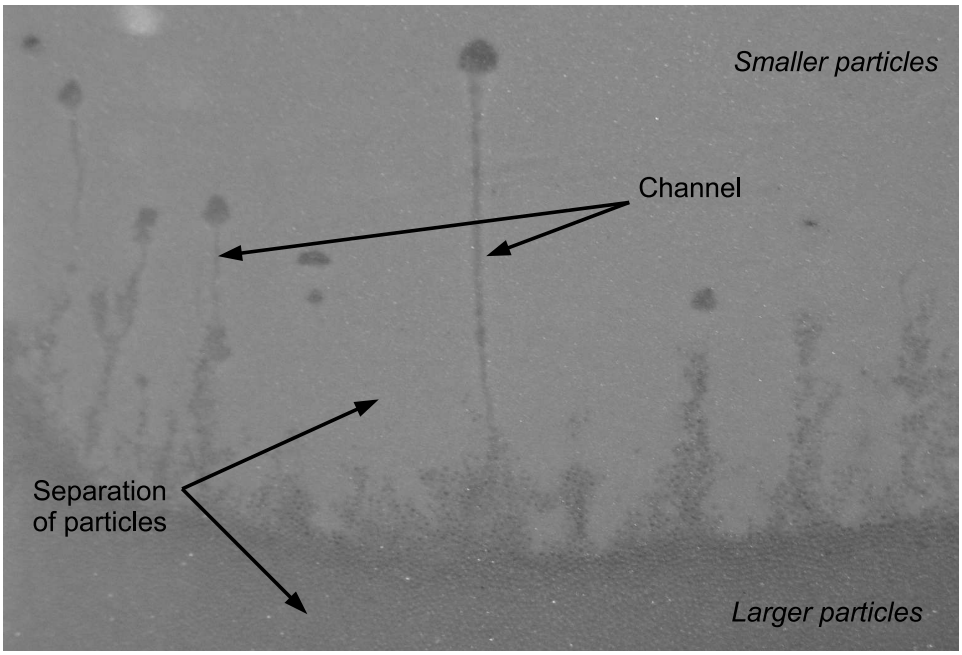

Figure 7.7: Channelling in a particle bed reactor consisting of a mixture of a $100 - 200\mu m$ and a $750 - 1000\mu m$ powder.

7.1 Experimental determination of the point of minimum fluidization

For all practical applications the minimum fluidization velocity can be determined from the intersection of the pressure drop lines of the fixed- and fluidized bed regimes. This is illustrated in Figures 7.8, 7.9 and 7.11. When the superficial velocity is decreased after fluidization the bed settles in a looser configuration, as mention earlier. Thus it is advisable to use the pressure drop lines of the decreasing superficial velocity [5]. In most practical

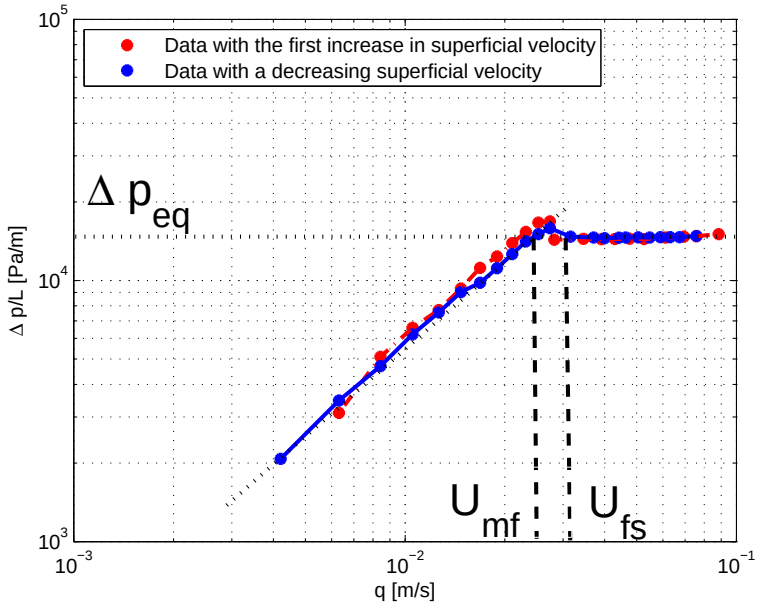

Figure 7.8: Fluidization of a glass powder with a distribution of particle sizes between $100 - 200\mu m$. The effect of non-fluidized regions and interlocking of particles is also visible.

situations the theoretical minimum fluidization velocity does not coincide with those found in practice. The velocity at which the entire weight of the packed bed is fully supported by the upward flowing fluid is called the fully supported velocity, and is denoted by U_{fs}. An estimation of the minimum fluidization velocity and the fully supported weight velocity are indicated in Figures 7.8 and 7.10. For the $100 - 200\mu m$ particle bed, the experimentally determined minimum fluidization is thus equal to $0.02316 m/s$. In Figures 7.8, 7.9 and 7.11 the pressure drop for the fluidized regime is represented by Δp_{eq}. In Figure 7.9 the minimum fluidization is determined for the particle range $400 - 600\mu m$. This was the sample that exhibited behavior closest to the theoretical model. The only deviating effect was that of the gradual transition from the one regime to the other. As mentioned previously this is mainly caused by particular regions being fluidized while others are still in a fixed bed formation. In Figure 7.10 the region of minimum fluidization was enlarged. The minimum fluidization and fully supported weight velocity can be distinguished clearly in the close up on Figure 7.10. The lower pressure drop can also be distinguished clearly between the increasing and decreasing velocity (refer to theoretical Figure 7.1). The experimentally determined minimum fluidization velocity for the bed consisting of $400 - 600\mu m$ particle is $0.2105 m/s$. According to Davidson [5] the criteria for a well-fluidized bed is a low particle

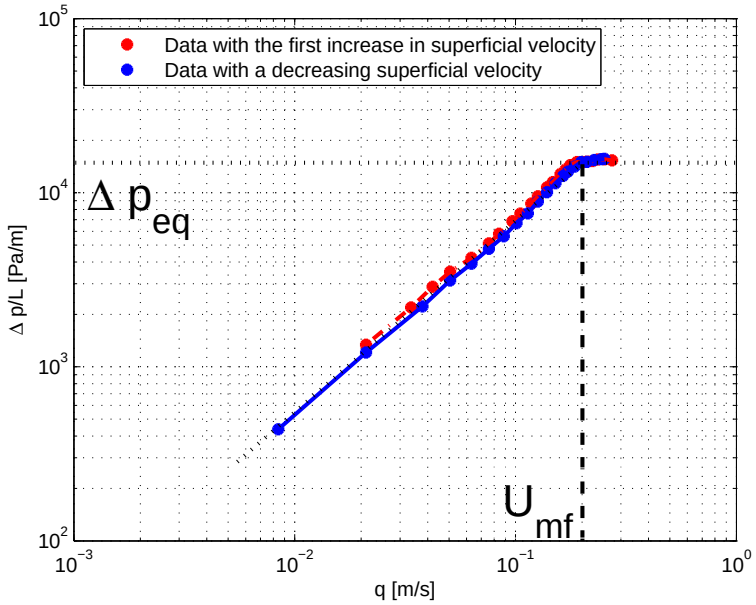

Figure 7.9: Fluidization of a glass powder with a distribution of particle sizes between $400 - 600\mu m$ on a log-log scale.

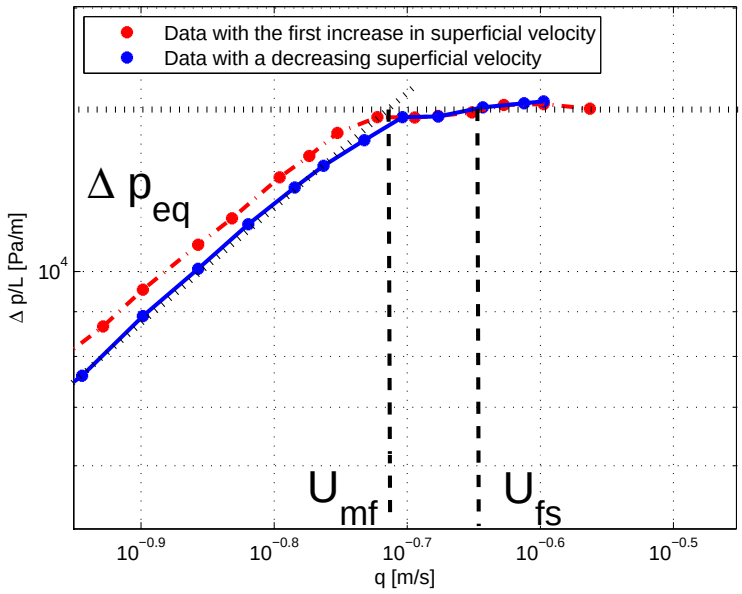

Figure 7.10: Experimental determination of the minimum fluidization- and fully supported weight velocity.

density, small particle size, small particle size range, a particle shape approaching a sphericity of one and a high fluid density. All the previous criteria are relative. Furthermore the criteria that render a bed well behaved can also be the criteria that makes it difficult to fluidize and cause channelling. From the data collected at the TUC, it can be deduced that the $400 - 600\mu m$ particle bed behaves the best as seen from Figure 7.10. The $100 - 200\mu m$ parti-

cle bed is so small that the particles interlock and cause the previously mentioned frictional "hump". The $750 - 1000\mu m$ particle bed produced data that deviated the most from the theoretical model. The cause can be the relatively large particle size as well as a relatively large size distribution. After fluidization the larger particles could have settled at the bottom of the column while the smaller particles could have gathered in the top section. So the separation produced a larger bed volume resulting in a higher porosity. The large particles have a size range of $250\mu m$ while the other samples have a range of $100\mu m$ and $200\mu m$, respectively (the particle size distribution should have the shape of a bell-shaped curve as described in Chapter 4). Thus with the largest particle range, the separation of particles according to their sizes has the biggest effect on the $750 - 100\mu m$ glass spheres. From the samples used at the TUC the $400 - 600\mu m$ glass powder had the best balance between the factors that makes a bed fluidize well. Nevertheless, the experimental minimum fluidization velocity of the large particles was determined to be approximately $0.421 m/s$. To quantify the results determined

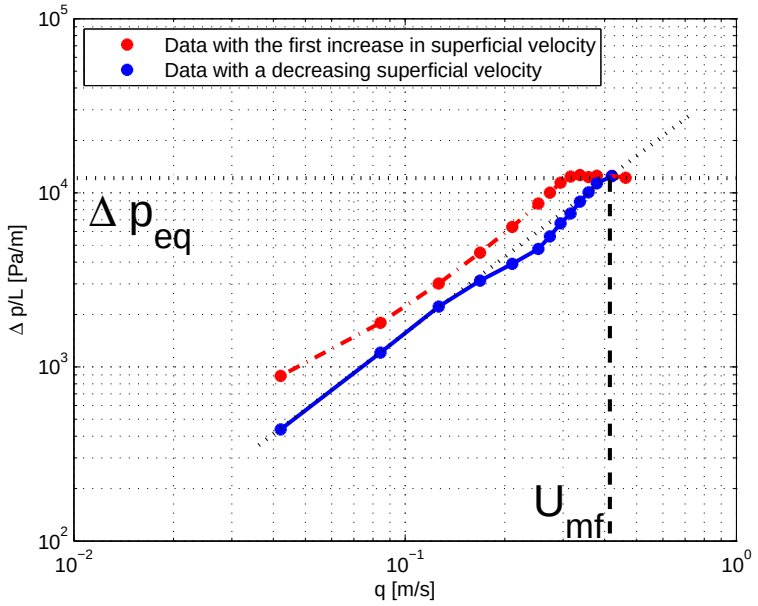

Figure 7.11: Fluidization of a glass powder with a distribution of particles sizes between $750 - 1000\mu m$. Thus having a size range of $250\mu/m$, the largest of the three powders.

with the experimental method, the theoretical value of the minimum fluidization velocity can also be determined for all three powders.

7.2 Theoretical determination of the minimum fluidization velocity

In the absence of an experimental facility a theoretical value for the minimum fluidization can be determined. As is evident from Figures 7.8, 7.9 and 7.11, fluidization occurred at different superficial velocities for each of the three different powders. To calculate an equation for the minimum fluidization velocity, U_{mf}, the net weight on the particles has to be balanced with the upward force acting on the bed. The upward force exerted on the particles is

given by the pressure drop over the porous structure multiplied by the effective area. Call this force F_{up}, and it is expressed as:

$$F_{up}(upward\ force\ on\ packed\ bed) = \Delta pA. \tag{7.2.1}$$

If the packed bed has an effective height of, L, and a porosity of ϵ, it follows that the effective volume of the solid particles is $(1-\epsilon)AL$. The net weight of the particles can be determined by the calculation of the resultant vertical force acting on the packed bed, namely:

$$\sum F_{vertical} = (\rho_p - \rho_f)Vg,$$

where g is the magnitude of the gravitational acceleration and V is the volume of the solid particles. Knowing that $V = (1-\epsilon)AL$, it follows that the nett weight of the particles (F_{nett}) is given by:

$$F_{nett} = (1-\epsilon)(\rho_p - \rho_f)ALg. \tag{7.2.2}$$

For the bed to be in equilibrium the upward force on the bed must equal the downward force, yielding the following expression for the pressure drop:

$$\Delta p = (1-\epsilon)(\rho_p - \rho_f)Lg. \tag{7.2.3}$$

In the case of a low Reynolds number discharge, equation (7.2.3) can be combined with the Carman-Kozeny equation (2.3.3) in conjunction with the Mcdonald correction, yielding:

$$U_{mf} = \frac{(\rho_p - \rho_f)gd_s^2\epsilon^3}{180(1-\epsilon)\mu}. \tag{7.2.4}$$

Since equilibrium was assumed in equation (7.2.3) the particular superficial velocity calculated in equation (7.2.4) is the minimum fluidization velocity [5].

From the granular RUC model it follows that the relationship between the pressure drop and the porosity is given by the following equation:

$$-\frac{dp}{dx} = \frac{25,4(1-\epsilon)^{4/3}\mu q}{d_s^2\left(1-(1-\epsilon)^{1/3}\right)\left(1-(1-\epsilon)^{2/3}\right)^2} + \frac{c_d\rho(1-\epsilon)q^2}{2\epsilon\, d_s\left(1-(1-\epsilon)^{2/3}\right)^2}, \tag{7.2.5}$$

with d and d_s as defined in Figure 2.2. Similarly to the Ergun model it follows, in the lower Reynolds number limit, that

$$U_{mf} = \frac{gd_s^2(\rho_p - \rho_f)\left(1-(1-\epsilon)^{1/3}\right)\left(1-(1-\epsilon)^{2/3}\right)^2}{25.4\mu(1-\epsilon)^{1/3}}. \tag{7.2.6}$$

The quadratic terms of both the Ergun equation [8] and the granular RUC model [7] mainly represent flow behavior in the Forgheimer regime. The minimum fluidization values that are calculated with equations (7.2.4) and (7.2.6) are only accurate in the Darcy regime. The particles used in this study's experiments have a range of particle sizes. Ideally some definition of an average particle size is needed as described in Chapter 4. Unfortunately sieving analysis is only performed on the powder with a particle distribution of $400-600\mu m$. For this powder the two definitions defined in Chapter 4, namely dp_{50} and dp_{sv}, will be used. For the other two powders the median size in the range will be used, in other words, for the

$100 - 200\mu m$ powder $150\mu m$ will be used as representative diameter and for the $750 - 100\mu m$ glass spheres $425\mu m$ will be implemented.

For the theoretical values to be as accurate as possible the porosity that should be used in equations (7.2.4) and (7.2.6) is the porosity at the point of fluidization [5]. The porosity at the point of fluidization can be calculated by using the bed height after the bed has been fluidized at least once and has settled into a looser arrangement of particles (refer to Figure 7.1). The porosities for the $100 - 200\mu m$, $400 - 600\mu m$ and $750 - 100\mu m$ powder at minimum fluidization velocity were 0.36, 0.35 and 0.34 respectively. In Table 7.1 the minimum fluidization velocities are presented as calculated via the experimental and theoretical models respectively. The theoretical models do not compare well to the experimentally de-

Glass powder diameter range	*Experimental* $U_{mf}\ [m/s]$	*Theoretical Ergun* $U_{mf}\ [m/s]$, eqn. (7.2.4)	*Theoretical granular RUC* $U_{mf}\ [m/s]$, eqn.(7.2.6)
$100 - 200\mu m$	0.023	0.012	0.012
$400 - 600\mu m$	0.210	0.10 (dp_{50})	0.11 (dp_{50})
		0.12 (dp_{sv})	0.12 (dp_{sv})
$750 - 1000\mu m$	0.421	0.34	0.35

Table 7.1: Comparison of the different calculated estimations for the minimum fluidization velocity for three different spherical particle specimens.

termined values of the minimum fluidization velocities. The cause may be attributed to the non-uniformity of the particles used. Another reason may be due to the fact that the effect of the Forcheimer regime is ignored in the theoretical derivation.

7.3 Comparing the granular RUC model and the Ergun equation to pressure drop data of mixed particle beds

In comparing the Ergun equation [8] and the granular RUC model [7] to the mixed powders data, only the data points preceding fluidization were used. The two models were not implemented in this study to predict physical quantities in the fluidized or bubbling regimes. For all the following comparisons the data that was used was acquired after fluidization had occurred at least once. If fluidization had not occurred yet there may still be some bed expansion before the point of fluidization, and the current comparisons only investigate flow through fixed beds (refer to Figure 7.1).

For the $100 - 200\mu m$ particles the drag factor, c_d, was taken to be equal to 1.9 as prescribed by du Plessis [7]. In Figure 7.12 an envelope is shown within which the particle sizes may differ. This provides a clear demonstration of the influence of the particle size that is chosen to represent the mixed particle bed. In Figure 7.12 the data does not fit in the envelope produced by the granular RUC model with a diameter of $100\mu m$ and $200\mu m$ respectively. The data can lie within an envelope produced by two approximations with particle diameters of $200\mu m$ and $300\mu m$. Both, the Ergun equation and the granular RUC model over-predict the pressure drop (refer to Figure 7.12 and 7.13). The main cause of the over-prediction may

be related to the formation of channels in the powders. In mixed beds with a wide range of particle sizes, the formation of channels can be seen with the naked eye (refer to Figure 7.7). This was observed in a mixture of the $100 - 200\mu m$ and $750 - 1000\mu m$ powders and this would suggest the possibility that a channel can also form within a smaller range of particle sizes. A fair amount of static electricity was also present in the column during the experiments. It is not evident to what extent this would have influenced the formation of channels in the powder.

The curvature of the models' predictions has the same trend as that of the data. This result possibly confirms the suspicion that the column to particle diameter ratio is too small in the case of the Raschig rings. That may be an explanation to the different curvature obtained with the Raschig ring data and the models' predictions (refer to Chapter 5). From Figures 7.12 (*b*) and 7.13 (*b*) it is clear to see that the curvature of both models is correct in the case of the $100 - 200\mu m$ powder.

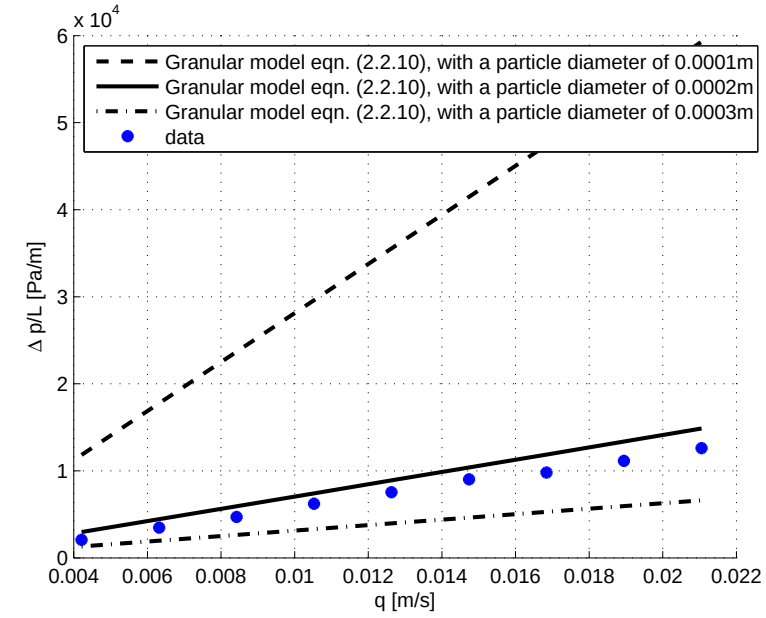

(a)

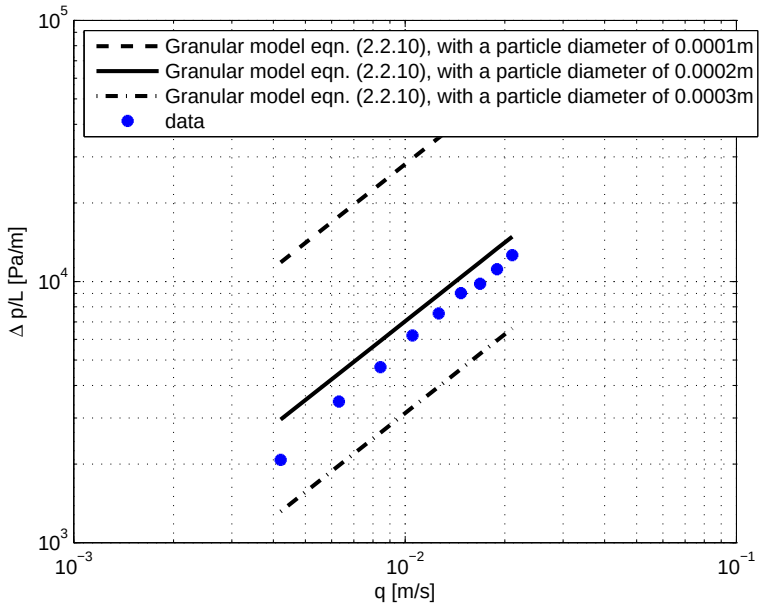

(b)

Figure 7.12: (a) Comparison of the granular RUC model [7] with experimental data given a range of particle sizes. The $100 - 200\mu m$ powder was used to acquire the data. (b) The same comparison but on a log-log scale.

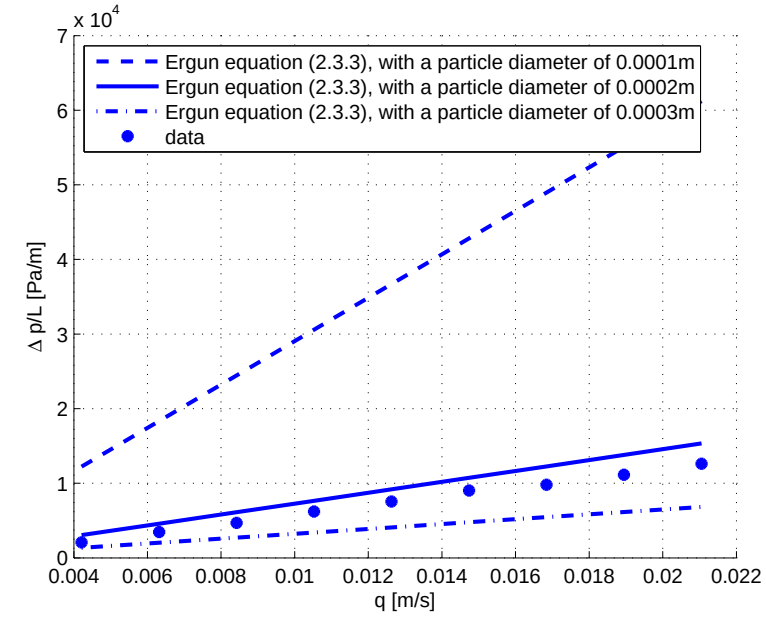

(a)

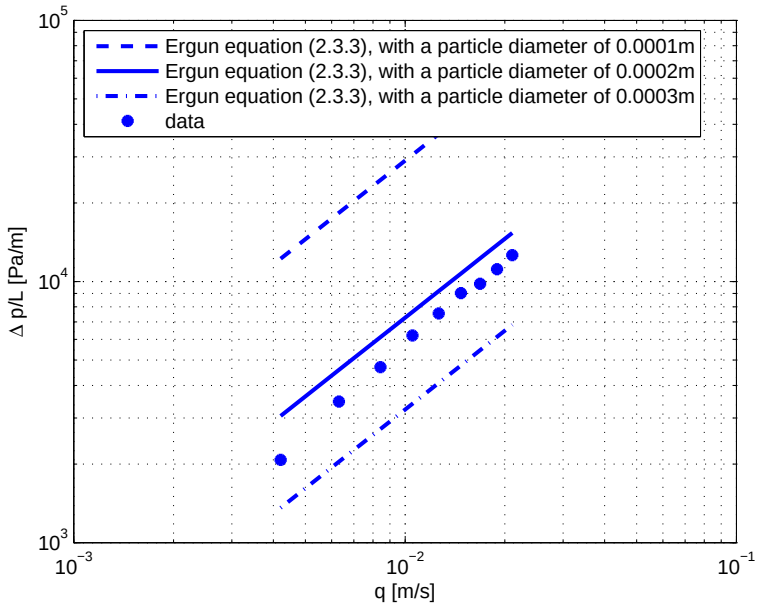

(b)

Figure 7.13: (a) Comparison of the Ergun equation [8] to experimental data with a range of particle sizes. The $100 - 200\mu m$ powder was used to acquire the data. (b) The same comparison but on a log-log scale.

Next the $400 - 600\mu m$ powder's data was compared with both the granular RUC model and the Ergun equation (refer to Figure 7.14 and 7.15). Again an envelope arises between the upper and lower limit of the powder particle range. As was the case in the preceding comparison, the models over predicted the pressure drop. The formation of channels may be to blame for this lower pressure drop through the bed as mentioned with the previous powder as well.

Sieving analysis was performed on the $400 - 600\mu m$ powder to validate that the powder's particle diameter distribution is in fact between 400 and $600\mu m$. The results of the sieving is presented in Chapter 4 and has shown that some particles smaller than $400\mu m$ were found. Nevertheless two definitions for an average particle diameter were implemented, namely dp_{50} and dp_{sv}. Both of these were between 400 and $600\mu m$. Thus even with these average diameters the models produced a poor prediction.

Again the data and the models had approximately the same curvature as depicted in Figure 7.14 (*b*) and 7.15 (*b*).

For the $750 - 1000\mu m$ powder the comparison of the data to the Ergun equation [8] and the granular RUC model is given in Figures 7.16 and 7.17. This powder produces results that deviate the most from the data. In Figures 7.16 (*b*) and 7.17 (*b*) the different gradients produced by the models and those of the data are given. Thus it is clear that the relatively large particle size distribution and relatively large particles create physical effects that deviate from flow through uniform spherical particles. Again, channelling may be the cause for the large over prediction but this hypothesis could not be confirmed. This powder also had the largest difference in the pressure drop before and after fluidization of all the powders. Fluidization obviously had a big impact on rearrangement of the particles. As mentioned before, the smaller particles will settle on top while the larger particles will tend to move to the bottom of the column. This would cause the porosity to increase and thus cause a lower pressure drop. The Ergun equation [8] and the granular RUC model [7] should thus not be used on powder with a large span of particle sizes. The smaller the particle size distribution, the more accurate the prediction.

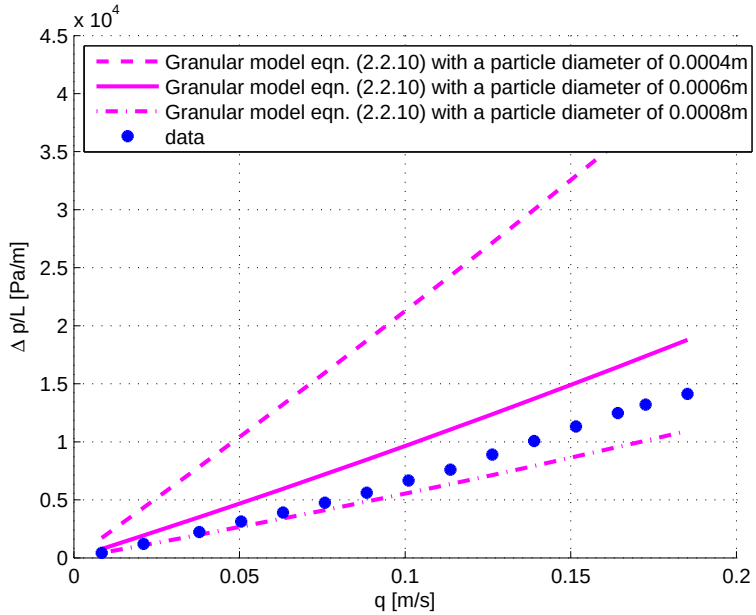

(a)

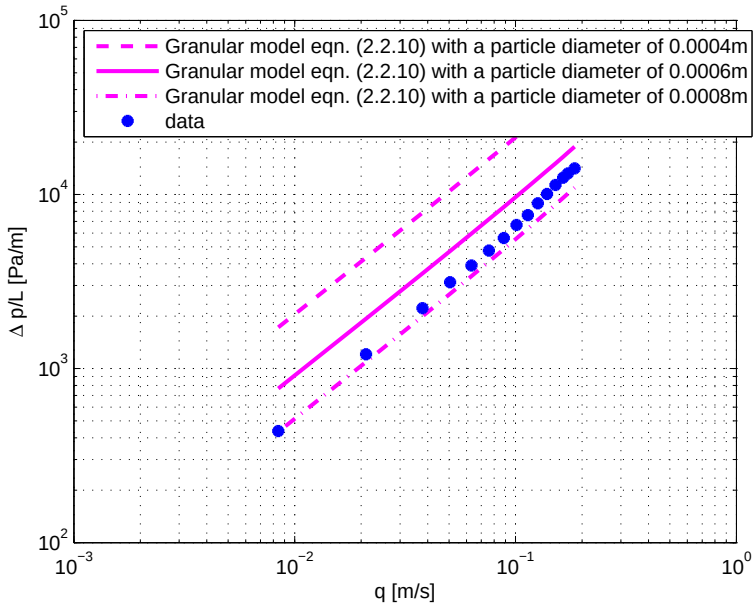

(b)

Figure 7.14: (a) Comparison of the granular RUC model [7] with experimental data given a range of particle sizes. The $400 - 600\mu m$ powder was used to acquire the data. (b) The same comparison but on a log-log axis.

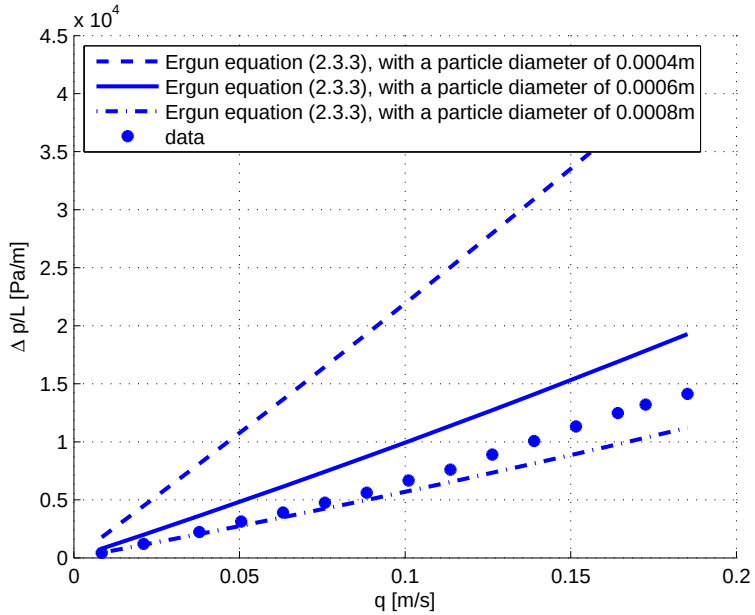

(a)

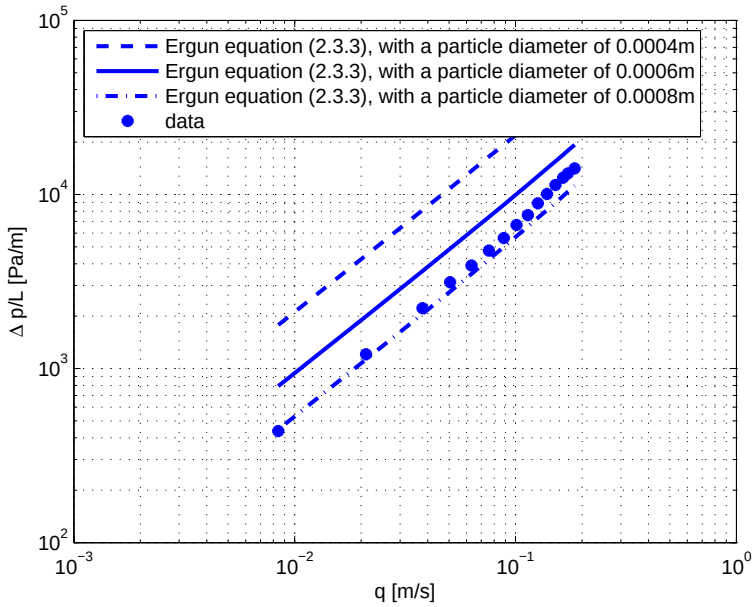

(b)

Figure 7.15: (a) Comparison of the Ergun equation [8] with experimental data given a range of particle sizes. The $400 - 600\mu m$ powder was used to acquire the data. (b) The same comparison but on a log-log axis.

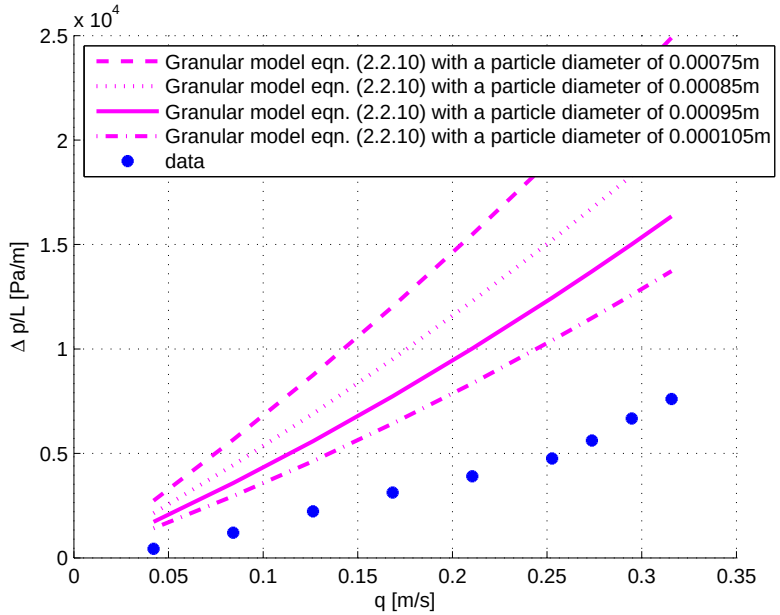

(a)

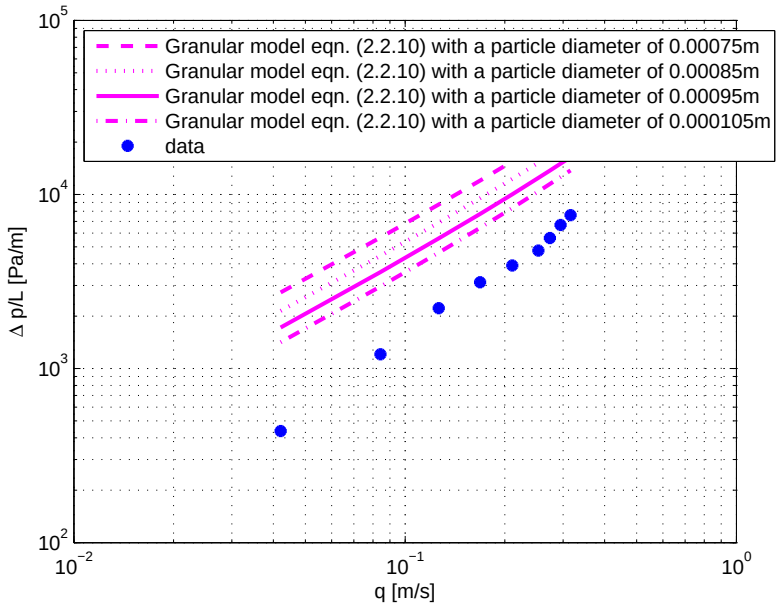

(b)

Figure 7.16: (a) Comparison of the granular RUC model [7] with experimental data given a range of particle sizes. The $750 - 1000\mu m$ powder was used to acquire the data. (b) The same comparison but on a log-log axis.

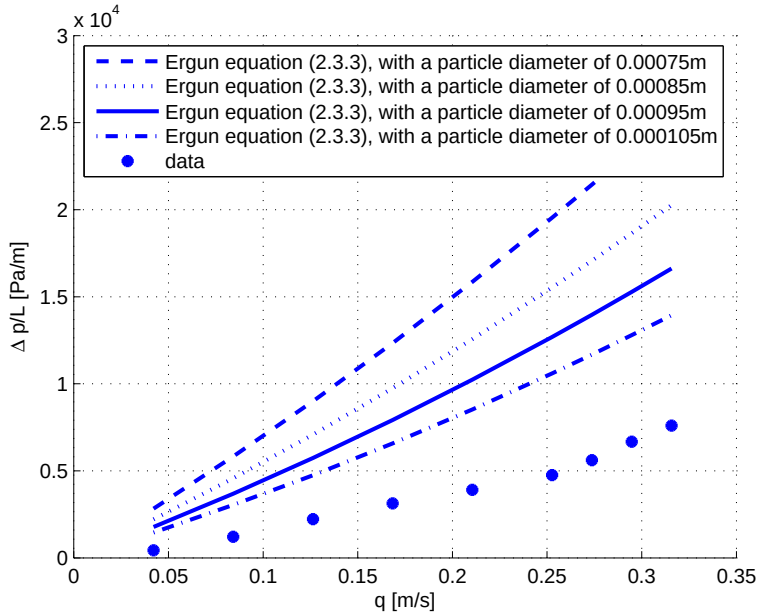

(a)

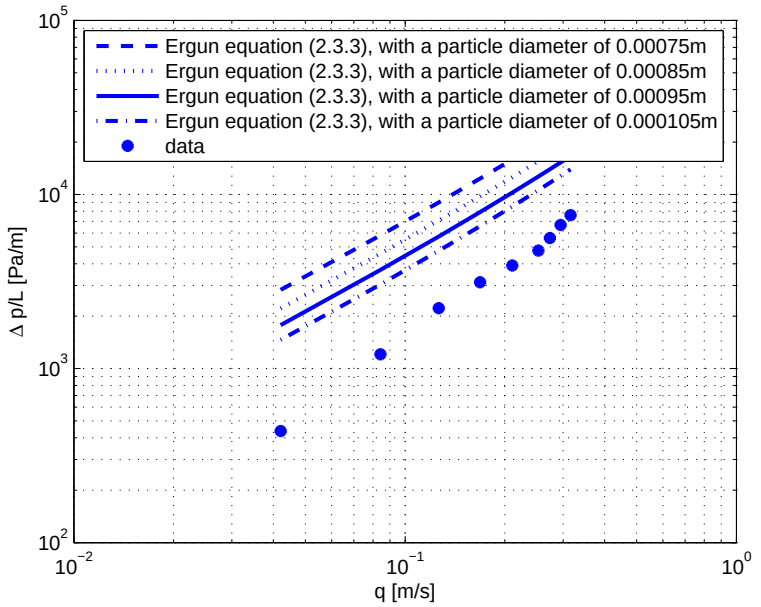

(b)

Figure 7.17: (a) Comparison of the Ergun equation [8] with experimental data given a range of particle sizes. The $750 - 1000\mu m$ powder was used to acquire the data. (b) The same comparison but on a log-log axis.

Of all the powders mentioned in this work, the pressure drop across the distributor was not 30% or more of the total pressure drop across the bed. This is therefore a reason for concern as the formation of stagnant regions is a possibility [21]. Unexpected flow behavior can be attributed to this effect as the extent of the dead zones are not known.

Chapter 8

Conclusion

The major contribution of this work was the generation of a set of data by means of experiments and analyses of possible predictive models. They produced satisfactory correlations to data and thus provide confidence in the capability of mathematical models to predict experimental trends for various fixed bed reactors.

The initial aim of using the spherical particle powders in the experimental part of this study was to check how experimental results would compare with the well known Ergun equation. As the Ergun equation was adapted empirically, based on the data obtained for flow through uniform spheres, it is expected to describe the flow through non-uniform spheres to some extent. The reason for such an assessment was because of the non-linearity of the data acquired with Raschig rings. The curvature differed from what the models predicted and the suspicion arose that the data may have been processed incorrectly. Thus, after the powders produced data that had the same behavior as the models, especially the Ergun equation, it could be concluded that the problem with the Raschig rings were not the result of incorrect data processing. The main cause is expected to be wall effects, due to the column to ring size ratio being small, almost equal to 10. If this ratio is much larger than 10 ($d_c/d_p >> 10$) the effect of the wall can be ignored [15].

With the incorporation of the Sonntag correction all of the models perform better. On the modelling side the Sonntag correction was applied with great success to existing empirical and pore-scale models. Using any of the models discussed in this work without Sonntag's correction will result in a under-prediction of the pressure drop for Raschig ring experiments.

In the powder beds a variety of different effects can manifest itself. These can cause everything from a small deviation in the data's pressure drop compared to the models, to a large over-prediction.

The deviations in the models from the data could be attributed to a variety of different effects. Almost none of these effects could be pin-pointed satisfactorily in this work due to time constraints. It is thus advisable to verify which effects predominated in both the Raschig ring and powder beds. The next logical step would then also be to find ways in which to combat the effects and to adapt the models to take these effects into account. The result will then be accurate predictions of flow through any packed bed and any column.

List of References

[1] R. Billet. *Packed column analysis and design*. Monography, Ruhr University Bochum, 1989. (Cited on pages 28 and 31.)

[2] Brown and associates. *Unit operations*. John Wiley and Sons, Inc., 1967. (Cited on pages 104, 106, and 108.)

[3] S. W. Churchill and R. Usagi. A general expression for the correlation of rates of transfer and other phenomena. *AIChE Journal*, 18:1121–1127, November 1972. (Cited on page 7.)

[4] S. Crosnier, J. P. du Plessis, R. Riva, and J. Legrand. Modeling of gas flow through isotropic metallic foams. *Journal of Porous Media*, 9:35–54, 2006. (Cited on pages 7, 8, 9, 13, 28, 29, and 37.)

[5] J. F. Davidson and D. Harrison. *Fluidization*. Academic Press, 1971. (Cited on pages 19, 83, 85, 86, 88, 91, and 92.)

[6] J. P. du Plessis. Porous media modelling. Classnotes, Applied Mathematics, University of Stellenbosch, February 2007. (Cited on pages 4, 5, and 77.)

[7] J. P. du Plessis and S. Woudberg. Pore-scale derivation of the ergun equation to enhance its adaptability and generalization. *Chemical Engineering Science*, 63:2576–2586, 2008. (Cited on pages 6, 7, 8, 13, 28, 29, 37, 40, 42, 54, 78, 81, 91, 92, 94, 96, 97, 99, and 109.)

[8] S. Ergun. Fluid flow through packed columns. *Chemical Engineering Progress*, 48:89–94, February 1952. (Cited on pages 9, 10, 22, 28, 29, 31, 37, 40, 91, 92, 95, 96, 98, and 100.)

[9] C. J. Geankoplis. *Transport processes and separation process principles*. Prentice Hall, 2003. (Cited on pages 9, 10, 11, 12, 14, 15, and 104.)

[10] D. Geldart, editor. *Gas fluidization technology*. John Wiley and Sons, 1986. (Cited on page 24.)

[11] Honeywell sensing and controle, Honeywell Inc., 11 West Spring street, Freeport, Illinois, 61032. (Cited on page 19.)

[12] W. Kast. *Chem. Ing. Techn*, 36(5):469, 1964. (Cited on page 28.)

[13] Koch-Glitsch. Intalox packed tower systems, structured packing. Booklet, Koch-Glitsch,LP, P.O. Box 8127, Wichita, KS 67208-0127, 4111 E. 37th Street North,Whichita, Kansas 67220, 2003. (Cited on page 1.)

[14] N. Kolev. *Packed bed columns for absorption, desorption, rectification and direct heat transfer*. Elsevier, 2006. (Cited on pages 11, 15, 16, 17, 21, 27, 28, 30, 31, and 32.)

[15] J. Mackowiak. Extended channel model for prediction of the pressure drop in single-phase flow in packed columns. *Chemical Engineering Research and Design*, 2008. (Cited on pages 29, 30, 32, 59, 60, and 101.)

[16] W. E. McCabe, J. C. Smith, and P. Harriott. *Unite operations of chemical engineering*. McGraw Hill, 2001. (Cited on page 11.)

[17] I. F. Mcdonald, M. S. El-Sayed, K. Mow, and F. A. L. Dullien. Flow through porous media - the ergun equation revisited. *Ind. Eng. Chem. Fundam.*, 18:199–208, January 1979. (Cited on pages 10, 32, and 40.)

[18] D. Nemec. *Pressure drop and liquid holdup in packed beds with cocurrent two-phase flow at high pressures*. Ph.d. thesis, University of Ljubljana, 2003. (Cited on pages 33, 34, 35, and 36.)

[19] D. Nemec and J. Levec. Flow through packed bed reactors: 1. single-phase flow. *Chemical Engineering Science*, 60:6947–6957, August 2005. (Cited on pages 27, 31, 32, 37, and 54.)

[20] G. Sonntag. The influence of the void ratio on the pressure drop in a packed bed. *Chemie Ingenieur Technik*, 32:317–329, May 1960. (Cited on pages 33, 35, 36, and 37.)

[21] S. Sookai. Fluidization fundamentals. In *Fundamentals and Applications of Fluidization*, pages 1–63. IFSA, November 2008. (Cited on pages 22, 83, and 100.)

[22] R. F. Strigle. *Packed tower design and applications*. Gulf Publishing Company, 1987. (Cited on page 11.)

[23] H. K. Versteeg and W. Malalasekera. *Computational fluid dynamics*. PEARSON, Prentice hall, 1995. (Cited on pages 73, 75, 76, and 79.)

Appendix A

Sieve analysis

Sieving, also known as screen analysis, is one of the simplest methods for determining an approximation to particle sizes. The method consists of passing the material successively through sieves progressively having smaller and smaller openings. A set of screens are shown in Figure A.1 that were used in the TUC to determine particle size distributions. The size of the particles passing through one screen but not through a screen with smaller opening is considered the arithmetic average of the two screens and is denoted by D_{avg} [2]. D_{avg} is also called the nominal size of a particle. In some cases the nominal diameter, D_p, of packing element is approximated by the nominal size, D_{avg}, from a sieve analysis [9].

The procedure normally consists of placing a particular weight of particles in the top screen, as shown in Figure A.1. The vibrating plate is then switched on for a designated amount of time. The sieves are then removed and the content and sieve are weighed. By subtracting the original mass of the sieve the amount of powder in each sieve can be calculated. The sieves are then placed back on the vibrating plate for a second time. The same procedure of weighing the powders is repeated. If the amount of powder per screen is within a satisfactory deviation, the weight of powder per screen is assigned to that particular nominal size. If not, the same procedure is repeated until the desired percentage error is achieved.

Depending on the accuracy required the degree to which the screens' openings are made smaller can be varied. According to Brow *et al.* [2] the standard screen interval used in the United Stats is a factor of $\sqrt{2}$, $\sqrt[4]{2}$ is also used for careful work and research [2]. In other words, the screen openings become progressively smaller with a factor of $1/\sqrt{2}$. In Figure A.1 the interval was not used simply due to the unavailability of the correct screen sizes.

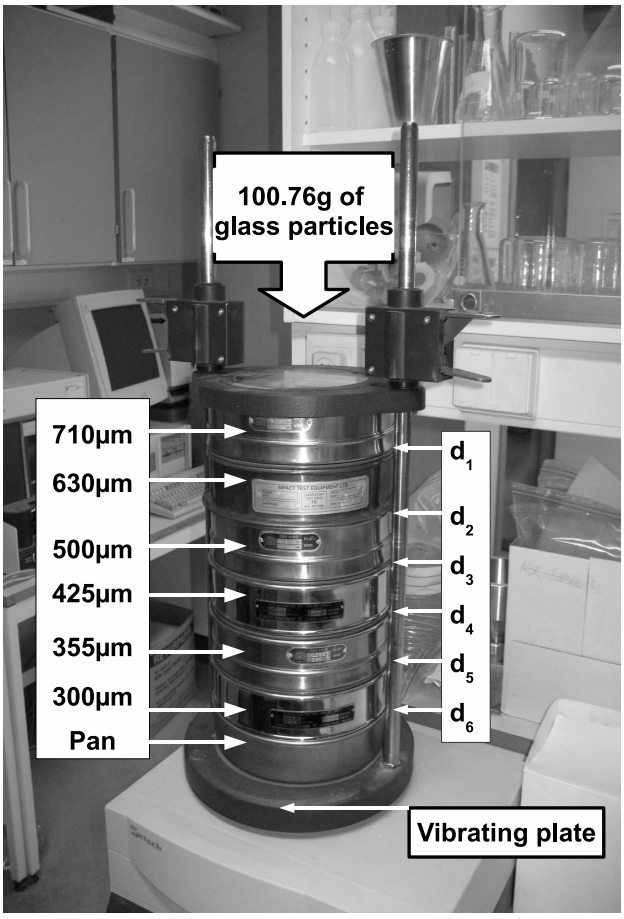

Figure A.1: Sieving analysis set-up. In this particular example the $400 - 600\mu m$ spherical glass powder was assessed this way.

Appendix B

Particle shape factor

When working with a particle the specific surface can be defined as in equation (3.1.1) in terms of the volume or it can be defined in terms of the mass of the particle. Brown *et al.* [2] defined the specific surface as the area of the particle divided by its mass [2]. If n is defined as the *ratio of specific surfaces*, it follows that:

$$\begin{aligned} n &= \frac{Specific\ surface\ of\ particle}{Specific\ surface\ of\ sphere\ of\ same\ diameter} \\ &= \frac{Specific\ surface}{6/\rho D_{avg}}, \end{aligned} \tag{B.0.1}$$

with ρ the density of the particle. For a spherical particle the surface area is known to be equal to πD^2, with D the diameter of the sphere. The mass of such a sphere is $\rho\pi D^3/6$, with ρ the density of the spherical particle. Thus using the definition for the specific surface that states that it is equivalent to the particle's area divided by its mass, it follows that the specific surface of the spherical particle is $6/\rho D_{avg}$. Given this expression, equation (B.0.1) can be written as:

$$n = \frac{Specific\ surface\ of\ particle}{6/\rho D_{avg}}. \tag{B.0.2}$$

Having knowledge of n the effect of the irregular shaped particles can now be investigated. The shape factor can be thought of as the ratio of deformation. For example: if a clay sphere's area is divided by the area of the clay after being shaped into the desired irregular shape, the particular shape factor, ϕ_s, is produced. Following the derivation presented in Brown *et al.*, the shape factor for a particle can be derived from n as follows:

$$\begin{aligned} n &= \frac{Specific\ surface\ of\ particle}{Specific\ surface\ of\ sphere\ of\ same\ diameter} \\ &= \frac{\dfrac{Surface\ of\ particle}{Mass\ of\ particle}}{\dfrac{Surface\ of\ sphere\ of\ same\ diameter}{Mass\ of\ sphere\ of\ same\ diameter}}, \end{aligned}$$

and knowing that $\phi_s = \pi D_p^2/S_{fs}$ it follows that:

$$\begin{aligned} n &= \left(\frac{\pi D_p^2}{\psi_s} / \frac{\pi D_p^3}{6}\rho\right)\left(\frac{\pi D_{avg}^3}{6}\rho / \pi D_{avg}^2\right) \\ &= \frac{D_{avg}}{D_p\,\phi_s}. \end{aligned} \tag{B.0.3}$$

Therefore,

$$\phi_s = \frac{D_{avg}}{D_p\, n}. \tag{B.0.4}$$

For example a cylinder with height twice its radius has the effective dimension, D_{avg}, of $2r$, and the diameter of a sphere having the same volume as the particle is $2.289r$. A cube having sides of length a has an effective dimension of a and the diameter of a sphere with the same volume is equal to $1.24a$ (See Figure B.1).

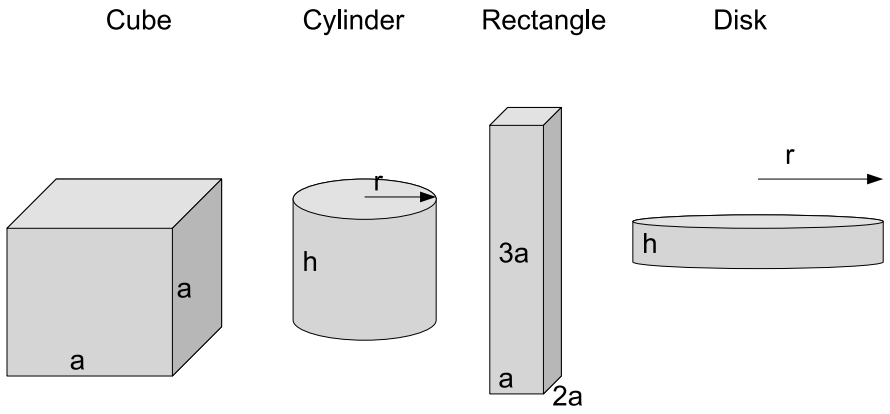

Figure B.1: Some basic geometric shapes used in Table B.1 .

In Table B.1 the shape factors for some geometric shapes are provided. The actual shapes of particles encountered in the industry can only be determined by microscopic examination and not with elementary geometry as is the case in Table B.1.

Shape	Particle Shape factor, ϕ_s	$\frac{D_p}{D_{avg}}$
Sphere	1	1
Octahedron	0.847	0.965
Cube	0.806	1.240
Rectangular prisms		
$a \times a \times 2a$	0.767	1.564
$a \times 2a \times 2a$	0.761	0.985
$a \times 2a \times 3a$	0.725	1.127
Cylinders		
h=2r	0.874	1.135
h=3r	0.860	1.310
h=10r	0.691	1.960
h=20r	0.580	2.592
Disks		
h=1.33r	0.858	1
h=r	0.827	0.909
h=r/3	0.594	0.630
h=r/10	0.323	0.422
h=r/15	0.254	0.368

Table B.1: Shape factors for some basic geometric shapes, using the definition presented in equation (B.0.4) [2].

Some small discrepancies exist among the presented data and the values that were recalculated. A possible explanation for this, is that at the time Brown *et al.* wrote *Unit operations*, log-books were still used [2]. The results produced by four-figure log-books were not as accurate as the present day calculations.

B.0.1 Packed bed shape factor

Although it is possible in theory to calculate the shape factor of a particle from its dimensions, it is not simple in practice. In most cases it is practically impossible, according to Brown *et al.* [2]. The shape factor or sphericity in packed beds are calculated experimentally. Given enough experimental data the shape factor for a porous packed bed can be calculated using equation (3.1.7).

Appendix C

Metallic Raschig rings

The effect of Sonntag's correction on the porosity and the specific surface is tabulated in Table C.1. In the case of flow through metal Raschig rings, the form drag factor was kept at

m	a $[m^2/m^3]$	ϵ [-]
0.1	348.87	0.3237
0.2	375.36	0.3833
0.3	401.86	0.4429
0.4	428.35	0.5025
0.5	454.84	0.5621
0.6	481.34	0.6218
0.7	507.83	0.6814
0.8	534.32	0.7410
0.9	560.82	0.8006
1	587.31	0.8602

Table C.1: Parameters associated with the different percentages of the volume available for flow inside the ring.

the prescribed 1.9 [7]. In Figures C.1 to C.10 the effect of Sonntag's correction is investigated. It is evident that the assumption of 20% stagnant volume inside the ring, is not a good assumption anymore. The stagnant volume appears to be in a bracket of between $50 - 70\%$. The curvature discrepancy is also not as severe as in the case of the glass Raschig rings (refer to Chapter 5). A possible cause for this phenomena, is the volume of the particles. The metallic Raschig rings had a much thinner wall compared to the glass Raschig rings and thus also produced a much lower porosity.

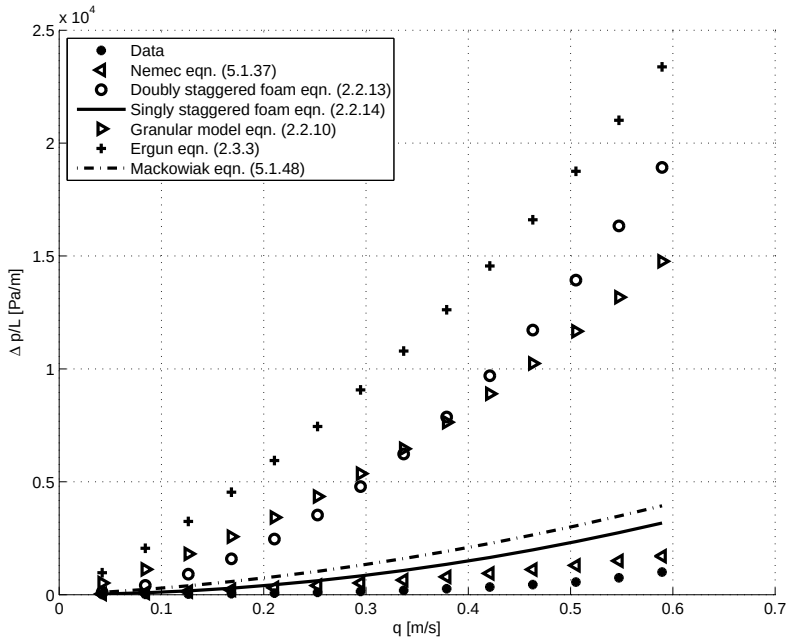

(a)

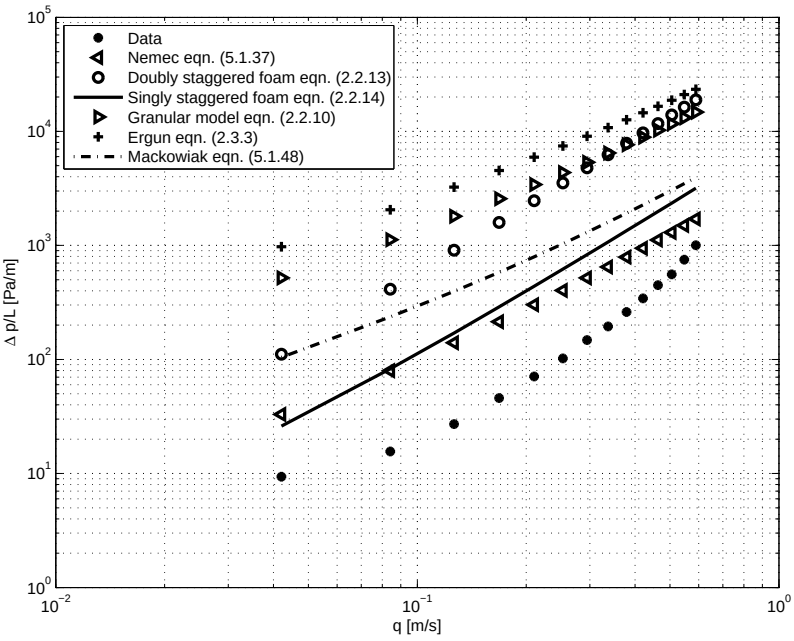

(b)

Figure C.1: (a) Comparison of models with the Sonntag correction equal to 10%. (b) The same comparison but on a log-log scale.

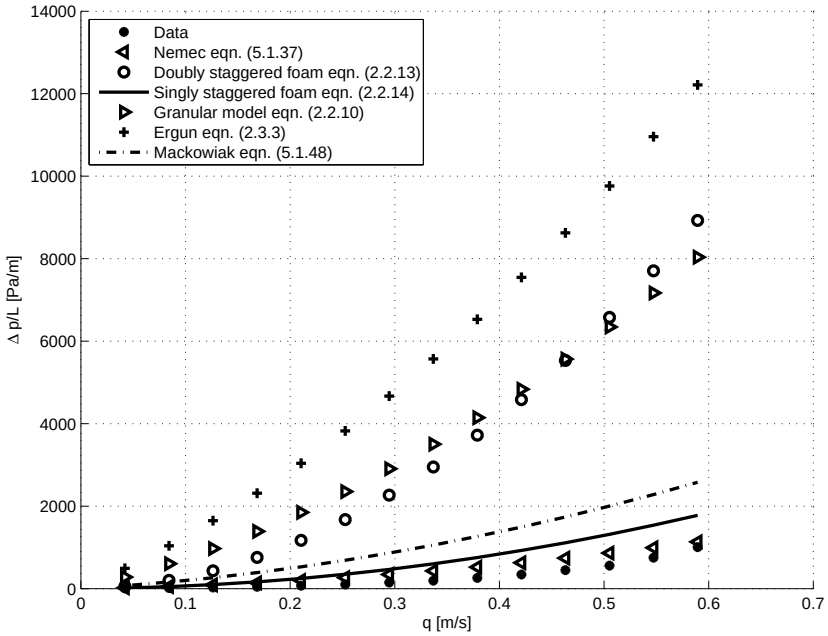

(a)

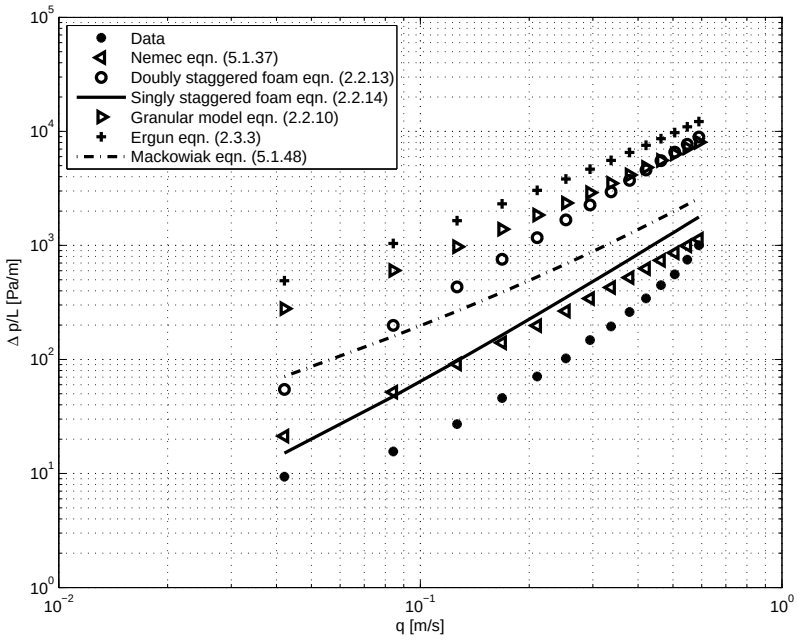

(b)

Figure C.2: (a) Comparison of models with the Sonntag correction equal to 20%. (b) The same comparison but on a log-log scale.

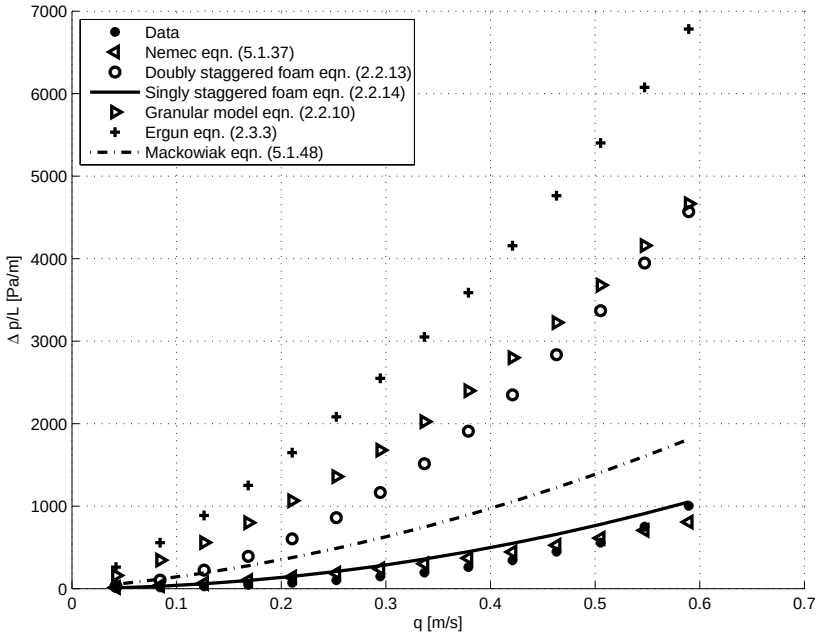

(a)

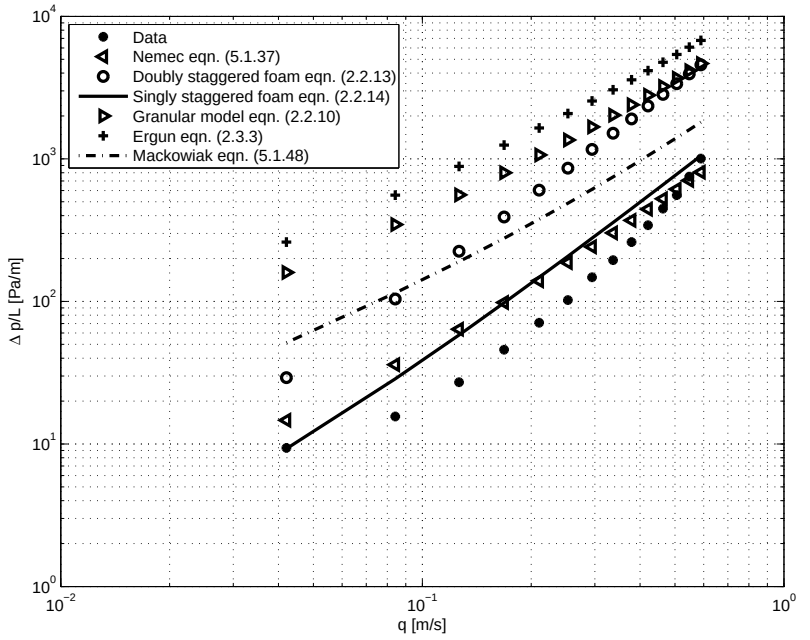

(b)

Figure C.3: (a) Comparison of models with the Sonntag correction equal to 30%. (b) The same comparison but on a log-log scale.

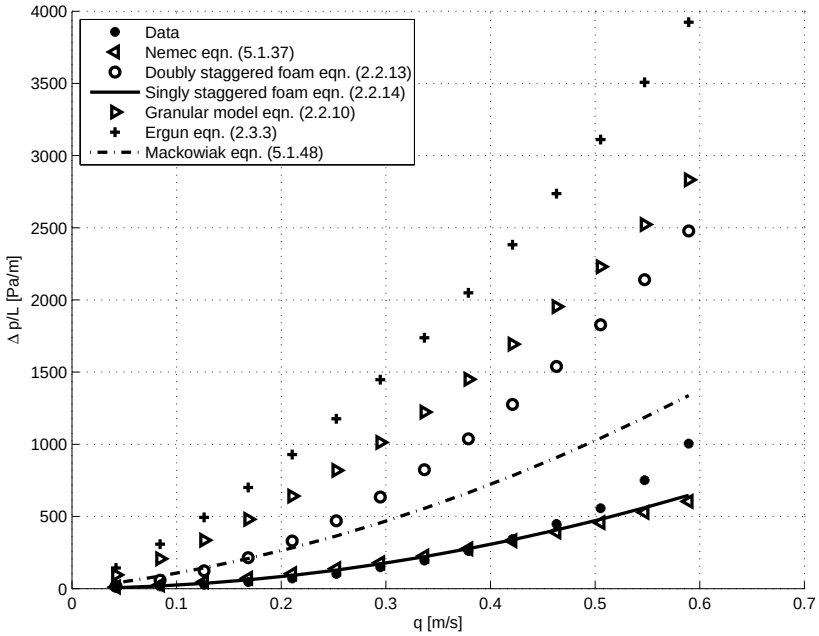

(a)

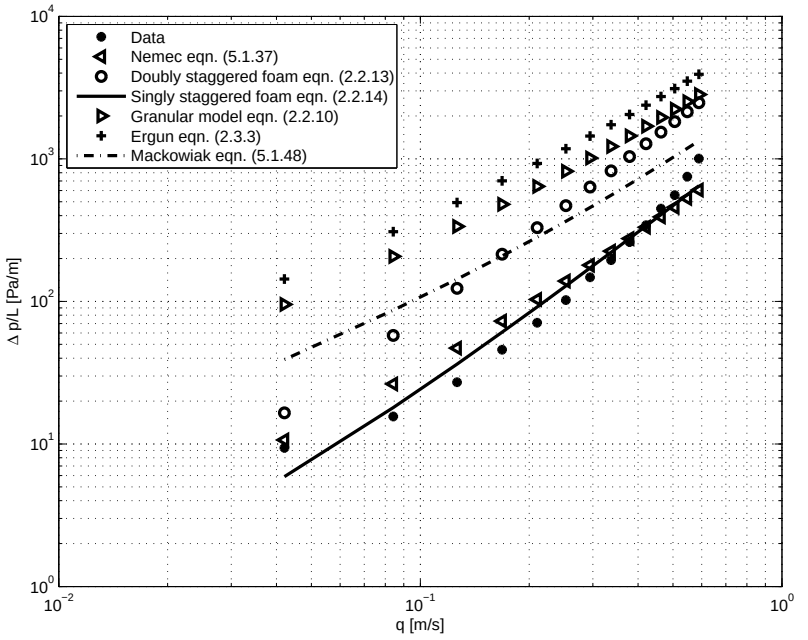

(b)

Figure C.4: (a) Comparison of models with the Sonntag correction equal to 40%. (b) The same comparison but on a log-log scale.

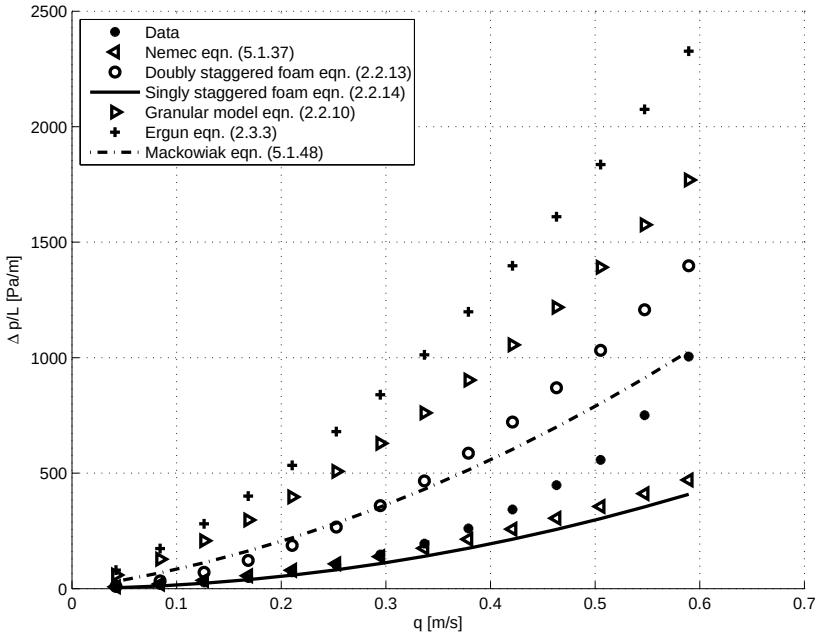

(a)

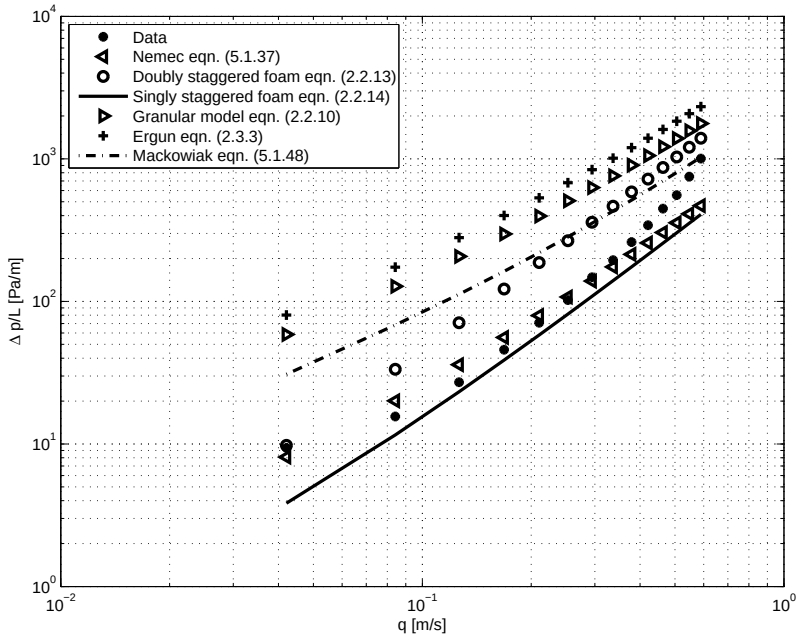

(b)

Figure C.5: (a) Comparison of models with the Sonntag correction equal to 50%. (b) The same comparison but on a log-log scale.

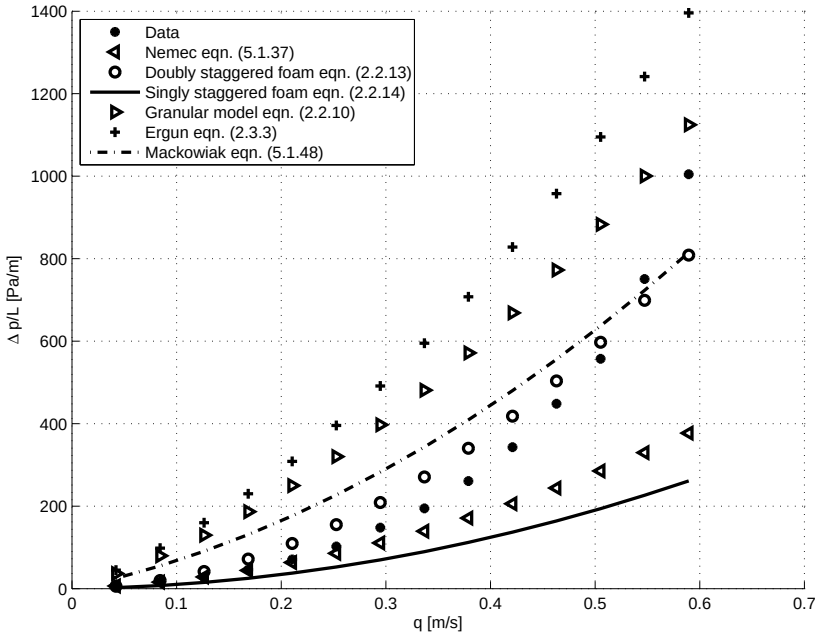

(a)

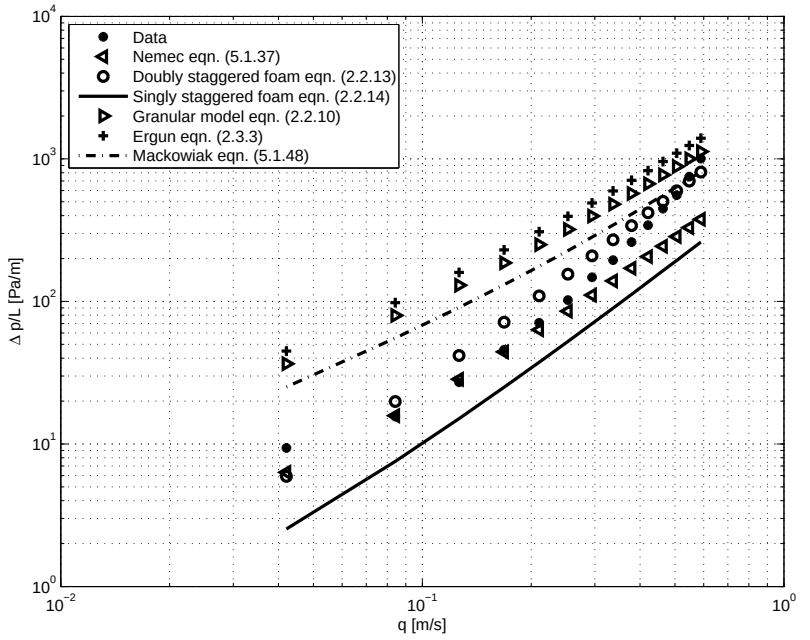

(b)

Figure C.6: (a) Comparison of models with the Sonntag correction equal to 60%. (b) The same comparison but on a log-log scale.

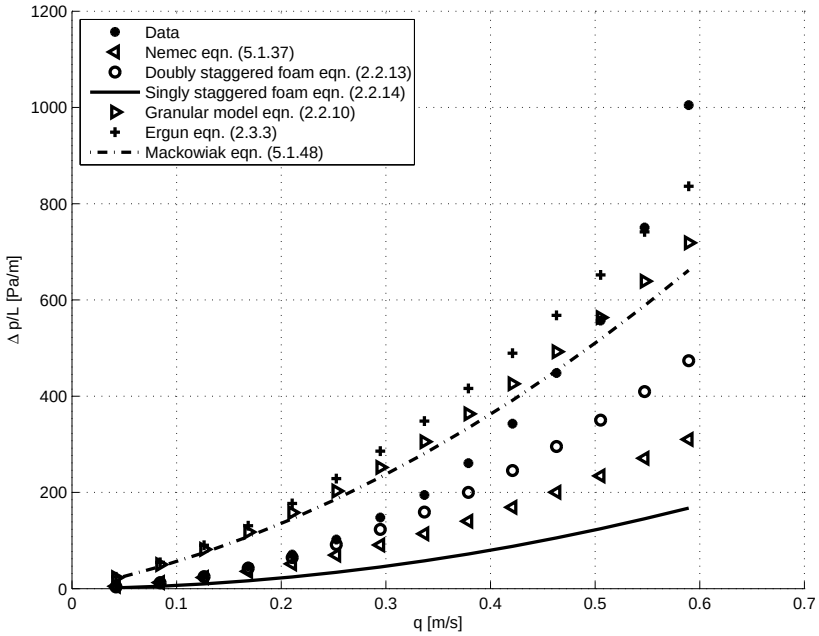

(a)

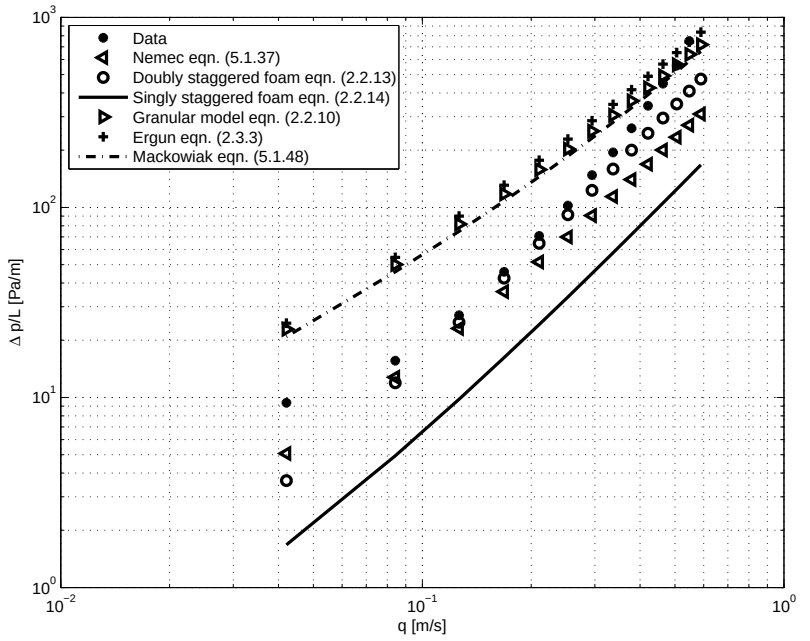

(b)

Figure C.7: (a) Comparison of models with the Sonntag correction equal to 70%. (b) The same comparison but on a log-log scale.

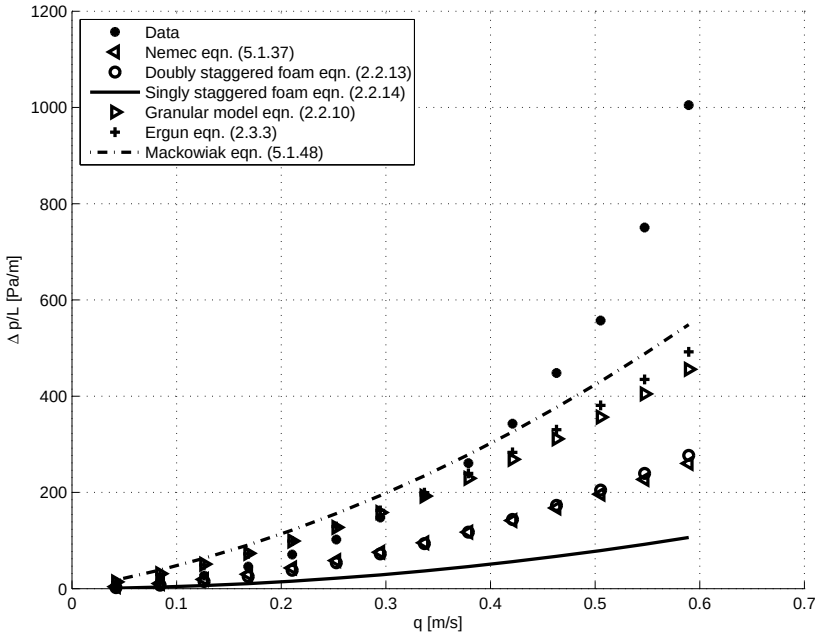

(a)

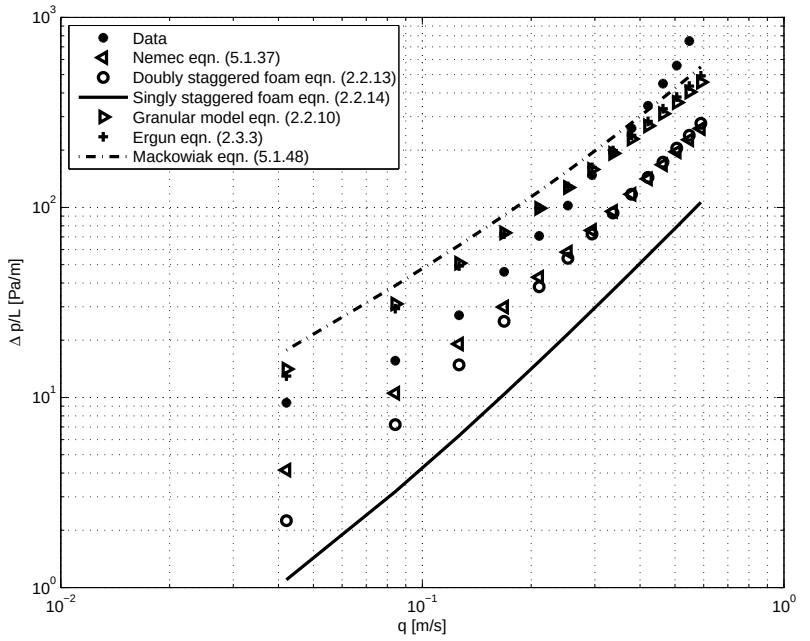

(b)

Figure C.8: (a) Comparison of models with the Sonntag correction equal to 80%. (b) The same comparison but on a log-log scale.

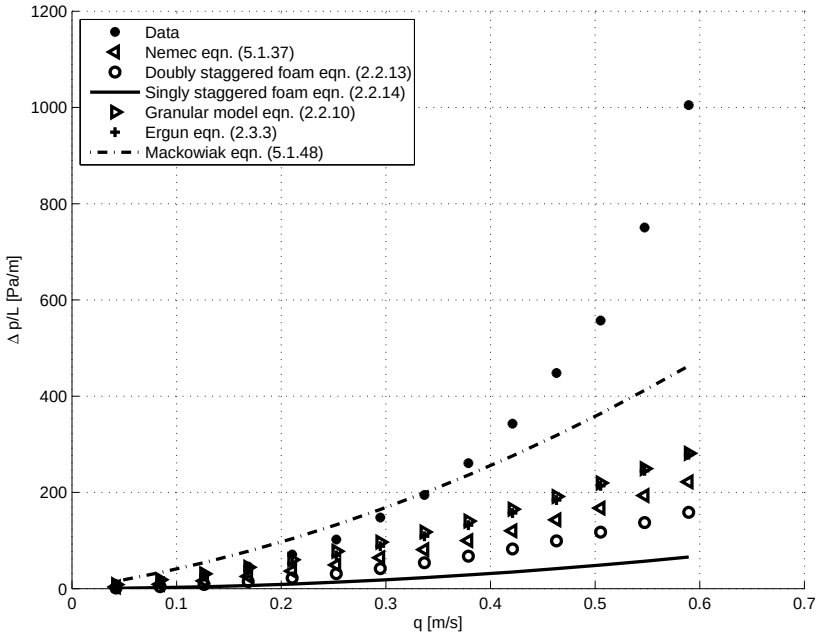

(a)

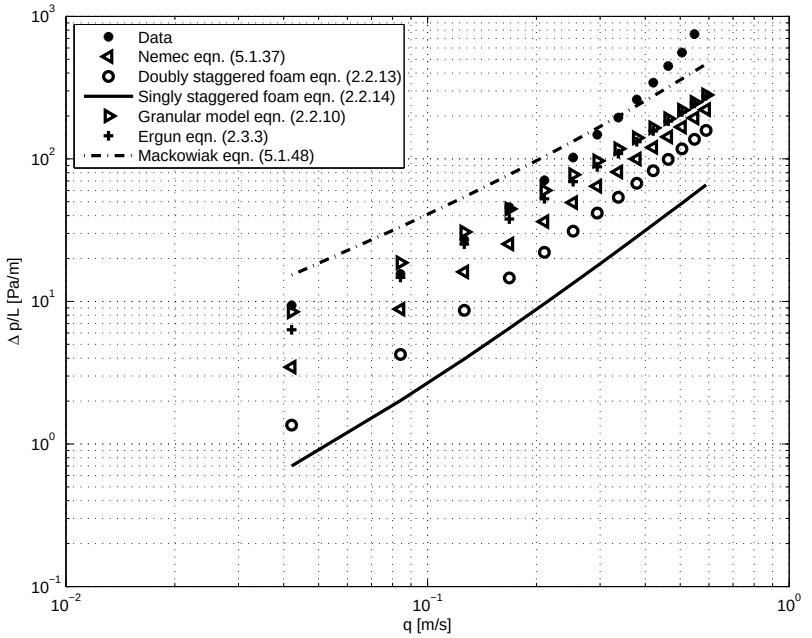

(b)

Figure C.9: (a) Comparison of models with the Sonntag correction equal to 90%. (b) The same comparison but on a log-log scale.

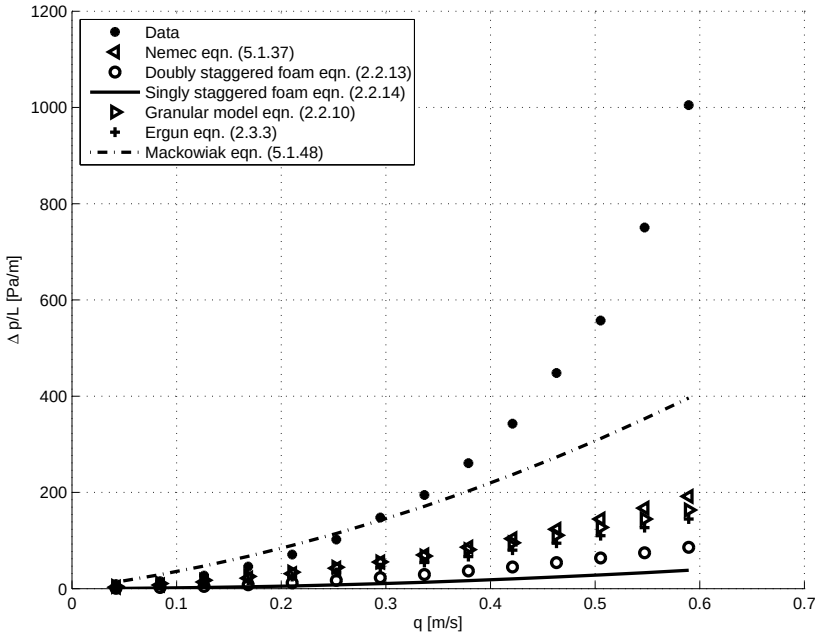

(a)

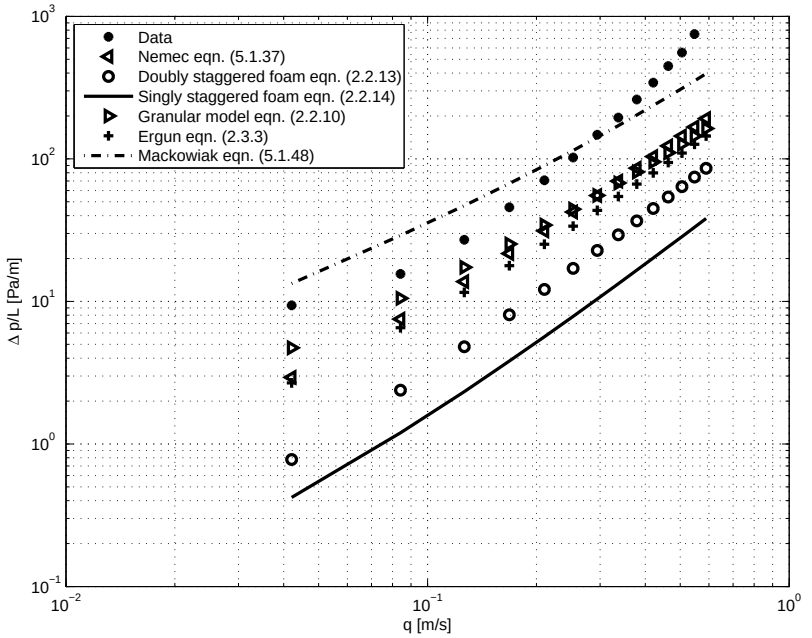

(b)

Figure C.10: (a) Comparison of models with the Sonntag correction equal to 100%. (b) The same comparison but on a log-log scale.